

AN EXPERIMENTAL INVESTIGATION OF  
HIGH CONTACT RATIO GEAR TOOTH BEHAVIOUR

Leslie Lajos Kenedi

A Thesis  
in  
The Faculty  
of  
Engineering

Presented in Partial Fulfillment of the Requirements  
for the degree of Master of Engineering at  
Concordia University  
Montréal, Québec, Canada

August 1982

© Leslie Lajos Kenedi, 1982

## ABSTRACT

### AN EXPERIMENTAL INVESTIGATION OF HIGH CONTACT RATIO GEAR TOOTH BEHAVIOUR

Leslie Lajos Kenedi

The objective of this study is to examine experimentally the static behaviour of a pair of High Contact Ratio Gears (HCRG). There is a recent interest in such gearing which stems from the possibility of significant weight saving.

Photoelasticity was used extensively in the past for investigating mostly a single tooth. For HCRG a multiple tooth model is necessary, as the interaction of the simultaneously engaged tooth pairs determines how the load is distributed. Building such photoelastic model is a novelty as extremely high precision is required.

The fillet stresses are observed in single and multiple tooth pair engagements. For a few selected fillet locations the stresses are plotted vs loading position measured on the line of action. Thus the static stress excursions of these points are obtained, allowing determination of the most damaging stress ranges.

7 Deflection measurements are taken and new concepts are introduced for setting their reference datum. The variable compliance of tooth pairs as a function of load position is determined and the sharing of the load is explored in depth using several new techniques.

As the structure is indeterminate, the concept of "Stress Admittance" is proposed. This is the stress due to the combined unit deflection of a pair of contacting teeth. It may be used for finding the critical location of the load in multiple tooth pair engagement.

- 1 -

DEDICATION

I dedicate this work to my wife

Anna,

whose enduring patience and loving  
encouragement made it all possible.

#### ACKNOWLEDGEMENT

I am indebted to my thesis supervisor Professor S.V. Hoa for guiding and encouraging me throughout this effort.

I would like to express my appreciation to T. Bui for introducing and coaching me in the application of Finite Elements to the subject matter, and to A. Elkholy mostly for his assistance at the input for the Cornell-Westervelt Dynamic Program.

I am grateful to all those colleagues at Pratt and Whitney Aircraft of Canada Limited who have contributed to this effort in the form of advice, suggestion and in the tiresome task of typing those equations and figures.

TABLE OF CONTENTS

	Page
List of Symbols	1
List of Figures	9
List of Tables	12
CHAPTER ONE	14
INTRODUCTION	
CHAPTER TWO	15
LITERARY SURVEY	
2.1 Stress Sensitivity - Short Beam Model Approach	16
2.1.1 The Lewis Equation	16
2.1.2 Dolan & Broghamer - Stress Concentration Factor	18
2.1.3 TheAGMA Standard	20
2.1.4 R.B. Heywood - Gear Tooth as a Projection	22
2.1.5 M.A. Jacobson - Proximity Effects	24
2.1.6 B.W. Kelley and R. Pedersen - The Contemporary State of the Art and a New Formula	25
2.1.7 I.M. Allison and E.J. Hearn - Effects of Friction	27
2.1.8 R.W. Cornell's - Expression for Fillet Stresses	27
2.2 Stress Sensitivity - Finite Element Method	29
2.2.1 L. Wilcox & W. Coleman's Polynomial Formula	30
2.2.2 G. Chabert, T. Dang Tran, R. Mathis's Expressions for Tensile and Compressive Fillet Stresses	33
2.3 Stress Sensitivity - Isotropic Wedge Theory	35
2.3.1 B.A. Shötter's Wedge Stresses and the Most Damaging Stress Range	35

TABLE OF CONTENTS (Cont'd)

	Page
2.4 Stress Sensitivity - Theory of Elasticity Solution, Using Complex Potentials and Conformal Transformation	37
2.4.1 T. Aida and Y. Terauchi	37
2.4.2 C.N. Baronet, G.V. Tordion's "Exact Stress Distribution"	41
2.5 Survey - Investigating Tooth Compliance	43
2.5.1 Weber's Semi-Elasticity Solution	43
2.5.2 W.J. O'Donnell: "Stresses and Deflections in Built in Beams"	46
2.5.3 G. Chabert, T. Dang Tran, R. Mathis - Deflections, using Finite Elements	47
2.5.4 A. Premilhat, G.V. Tordion, C.N. Baronet - Deflections, using Complex Potentials	50
2.5.5 R.W. Cornell's Expression for Pair Compliance	50
2.6 Conclusion of Survey	56
CHAPTER THREE	58
FORMULATION OF THE CONCEPT OF STRESS ADMITTANCE AND FATIGUE CONSIDERATIONS	58
3.1 Stress Sensitivity	60
3.2 Load Sharing in Multiple Pair Engagement	61
3.3 Stress Admittance	63
3.4 Equivalent Alternating Stresses	

- v -

TABLE OF CONTENTS (Cont'd)

	Page
CHAPTER FOUR TEST EQUIPMENT	64
4.1 The Prototype	64
4.2 The Model	64
4.2.1 Computation of the Profile	67
4.2.1.1 The Involute	67
4.2.1.2 The Fillet	70
4.2.1.3 Tip Relief	72
4.2.2 Making the Model	76
4.3 The Rig	80
CHAPTER FIVE TEST PROCEDURE	85
5.1 Geometric Considerations	85
5.1.1 Theoretical Match-Points of Pinion and Wheel	85
5.1.2 Points of Simultaneous Contact	85
5.2 Scaling	88
5.3 Loading	91
5.3.1 Scheme of Loading Points	93
5.4 Stress Measurements	95
5.4.1 The Photoelastic Method	95
5.4.2 Calibration	96
5.4.3 Determination of Stresses	97
5.5 Pair-Deflection Measurements	98

TABLE OF CONTENTS (Cont'd)

	Page
CHAPTER SIX	100
ALTERNATIVE ANALYTICAL METHODS	
6.1 Application of the Kelly-Pedersen Formula	100
6.2 Application of the Aida-Terauchi Formula	101
6.3 Using the Cornell-Westervelt Dynamic Program	102
6.4 An Application of Finite Elements	103
6.4.1 Element Network	103
6.4.2 The Program	110
6.4.3 Boundary Conditions	110
6.4.4 Loading	114
6.4.5 Determination of Deflections - Using Novel Reference Data	118
6.4.6 Determination of Fillet Stresses	120
CHAPTER SEVEN	121
RESULTS	
AND CORRELATION WITH ALTERNATIVE METHODS	
7.1 Stresses - Single Tooth Pair Engagement.	121
7.2 Stresses - Multiple Tooth Pair Engagement	134
7.3 Deflections	144



TABLE OF CONTENTS (Cont'd)

	Page
CHAPTER EIGHT	148
ANALYSIS OF RESULTS	
8.1 Pair Compliance - Experimental	148
8.2 Compliances from Finite Elements, Correlation of Results	150
8.3 Sharing of the Load at Multiple Engagement	152
8.3.1 Determination of the Loads Using Gauge Point Stresses	155
8.3.2 Graphical Determination of the Loads Using Deflections	158
8.3.3 Calculation of Loads Assuming Linearity	158
8.4 Stress Sensitivity and Stress Admittance	162
8.5 Equivalent Static Alternating Stresses	165
CHAPTER NINE	174
AN ESTIMATE OF THE ERRORS	
9.1 Bias Due to Parasitic Loading	174
9.2 Random Errors	176
CHAPTER TEN	180
CONCLUSIONS AND CONTRIBUTIONS	
10.1 Conclusions	180
10.2 Contributions to the Art	181
List of References	183
Appendix 1 - Work Equivalent Loads	A1

### LIST OF SYMBOLS<sup>1</sup>

a.	addendum
$a_1$	moment arm
A	cross sectional area
b	half width of contact
$b_1$	constant (Wilcox & Coleman)
$b_2$	length of side of equivalent straight flanked beam
B	face width of beam, thickness of model
$B_1$	variable (Wilcox & Coleman)
c	distance of extreme fiber from neutral axis
$c_1$	constant (Wilcox & Coleman)
C	compliance
$C_d$	center distance
$C_e$	equivalent compliance
$C_p$	pair - compliance
$C_{po}$	pair - compliance at pitch point
d	dedendum
$d_1$	constant (Wilcox & Coleman)
$D_1$	variable (Wilcox & Coleman)

<sup>1</sup> The assemblance of symbols quoted from a variety of sources are often conflicting. To make the text more readable the notation of some of the quoted formulas was changed, though an effort was made to retain as much as possible of the original nomenclature.

LIST OF SYMBOLS<sup>1</sup> (Cont'd)

e	half length of the weakest section
E	Young's modulus
E <sub>s</sub>	Young's modulus of support
f	material fringe constant [kPa - m], (psi-in)
g	size of gap
G	shear modulus
h	distance from contact to tooth centerline along the normal to the profile
h <sub>t</sub>	total depth of tooth
h'	distance
i	the i <sup>th</sup> number of a sequence
I	second area moment
J	geometry factor
k	dimensionless flexibility coefficient (Chabert)
K	stress concentration factor
K <sub>f</sub>	stress correction factor (AGMA standard)
K <sub>m</sub>	constant representing the effect of inaccuracies on the stresses in the model.
K <sub>1</sub>	"residual factor" (Wilcox & Coleman)
K <sub>2</sub>	O'Donnell correction factor
K <sub>3</sub>	constant
l	height from weakest section to load
l'	height from weakest section to the load line at its intersection with the tooth centerline
l <sub>s</sub> , l' <sub>s</sub>	l and/or l' with reference for maximum stress sensitivity

LIST OF SYMBOLS<sup>1</sup> (Cont'd)

$l'_F$	$l'$ with reference for maximum deflection
$l'_O$	height from fillet-flank blending point to load line and tooth centerline intersection
$l_t$	height from weakest section to tip of the tooth
$L$	length
$m$	module [mm]
$m_c$	contact ratio
$m_n$	load sharing ratio
$m_t$	tip modification
$M$	bending moment
$n$	integer
$N$	number of teeth
$N'$	fringe order
$N_1$	number of teeth in driver (pinion)
$N_2$	number of teeth in driven gear (wheel)
$p$	contact pressure
$P_c$	circular pitch
$P_B$	base pitch
$P_D$	diametral pitch
$r_c$	side length of wedge - compressive (Shotter)
$r_f$	fillet radius
$r_t$	side length of wedge - tensile (Shotter)
$r_1, r_2$	radii of curvature
$R$	radius - polar coordinate

4

LIST OF SYMBOLS<sup>1</sup> (Cont'd)

$R_B$	radius of the base circle
$R_H, R'_H$	radius of "Highest Point for Single Tooth Contact"
$R_P$	pitch radius
$R_r$	root radius
$s$	standard deviation
$s_B$	standard deviation in material thickness
$s_f$	standard deviation in material-fringe value
$s_m$	standard deviation due to model inaccuracy
$s_N$	standard deviation in fringe reading
$s_{vt}$	standard deviation in stress sensitivity
$s_W$	standard deviation in load
$S$	distance along the line of action from pitch point, +ve toward disengagement
$S'$	normalized position along the line of action $S/P_B$
$S_d$	Outer most point on the line of action, where both of the contacting surfaces are unmodified true involutes - disengagement side
$S_e$	Similar to $S_d$ - engagement side
$S_o$	Reference length on the line of action, either $S_{od}$ or $S_{oe}$
$S_{od}$	length of the disengagement side of the line of action
$S_{oe}$	length of the engagement side of the line of action
$t$	depth of the beam of the "weakest section"
$t_F$	depth of the beam at the foundation "boundary" for maximum deflection
$t_L$	depth of the beam at the application of the load
$t_o$	depth of the beam at the fillet-flank blending point

LIST OF SYMBOLS<sup>1</sup> (Cont'd)

$t_s$	depth of the beam for maximum fillet stress
$t_\gamma$	depth of the beam at fillet angle $\gamma$
$T$	arc tooth thickness
$u$	complex coordinate in $\zeta$ plane, real axis
$U$	"unbalanced residual factor" (Wilcox & Coleman)
$v$	complex coordinate in $\zeta$ plane, imaginary axis
$v_1$	complex variable on $v$ axis
$V$	stress-sensitivity [ $\text{mm}^{-2}$ ], ( $\text{in}^{-2}$ )
$W$	normal load
$W_d$	deadweight or rig load
$W_m$	normal load - model
$W_p$	normal load - prototype
$W_r$	radial component of the normal load
$W_{sh}$	"shared" normal load
$W_t$	tangential component of the normal load
$x$	coordinate axis
$x_1$	distance - Lewis layout
$y$	coordinate axis
$y'$	displacement along the line of action
$y'_b$	deflection - bending component
$y'_c$	deflection due to local compression
$y'_F$	deflection - contributed by the deformation of the fillet and the foundation region
$y'_{FB}$	component of $y'_F$ due to deformation in the fillet area
$y'_{FF}$	component of $y'_F$ due to deformation in the foundation area

LIST OF SYMBOLS<sup>1</sup> (Cont'd)

$y_1$	Lewis form factor
$Y$	modified form factor
$z$	complex variable in the plane of rectangular coordinates
$Z$	stress admittance $[N/mm^3]$ $(lb/in^3)$
$\alpha$	polar angle with reference to the <u>centerline of the tooth</u>
$\alpha_B$	polar angle to starting point of the involute on base circle
$\alpha_C$	polar angle to the center of the fillet radius
$\alpha_P$	polar angle of the pitch point
$\alpha_D, \alpha_M$	polar angle for points D and M respectively
$\alpha_1, \alpha_2, \alpha_3$	wedge angles (Skotter)
$\beta$	inclination of load to the normal at the point of maximum fillet stress - Kelly & Pedersen method
$\beta_1$	inclination of load with respect to the centerline of the tooth
$\gamma$	fillet angle, zero reference is the line connecting the two centers of fillet circles on each side of the tooth, +ve counterclockwise
$\gamma_F$	fillet angle for maximized deflection - Cornell method
$\gamma_{KP}$	fillet angle at maximum tensile stress, Kelley & Pedersen method
$\gamma_L$	fillet angle at the tangency of the Lewis parabola
$\gamma_O$	fillet angle at fillet-flank blending point
$\gamma_S$	fillet angle for maximized stress - Cornell method
$\delta$	width of a finite strip
$\Delta\alpha, \Delta\epsilon$	small angular differences
$\epsilon$	roll angle of a point on the involute
$\epsilon_A, \epsilon_C$	roll angle for points A and C respectively

LIST OF SYMBOLS<sup>1</sup> (Cont'd)

$\epsilon_p$	roll angle for pitch point
$\zeta$	complex variable in the plane of curvilinear coordinates
$\theta$	"vectorial angle" of a point on the involute ( $\epsilon-\phi$ ) also called inv ( $\phi$ ) [involute of $\phi$ ]
$\theta_C$	vectorial angle for point C
$\theta_m$	rotation of the root of a built in beam (O'Donnell)
$\theta_p$	vectorial angle for the pitch point
$\lambda$	angle of the normal to the profile at a point with reference to the normal to the tooth centerline
$\lambda_A \lambda_C \lambda_D \lambda_M$	angle of normals at points A, C, D, M respectively
$\nu$	Poisson's ratio
$\mu$	coefficient of friction
$\pi_1 \pi_2 \pi_3$	dimensionless ratios
$\rho$	equivalent radius of curvature
$\sigma$	stress
$\sigma_a$	alternating component of stress
$\sigma_{ae}$	equivalent alternating stress
$\sigma_b$	fillet stress due to the tangential component of the load
$\sigma_c$	max. compressive fillet stress
$\sigma_g$	"gauge stress" (Chapter 8)
$\sigma_m$	mean stress
$\sigma_n$	normal stress
$\sigma_r$	fillet stress due to the radial component of the load
$\sigma_{rb}$	the bending component of $\sigma_r$
$\sigma_{rd}$	the direct component of $\sigma_r$



LIST OF SYMBOLS<sup>1</sup> (Cont'd)

$\sigma_{sh}$	"shared stress" obtained in multiple engagement test
$\sigma_t$	max. tensile fillet stress
$\sigma_{uc}$	ultimate stress in uniaxial compression
$\sigma_{ut}$	ultimate stress in uniaxial tension
$\tau$	shear stress
$\phi$	pressure angle
$\phi_o$	pressure angle - arbitrary reference
$\phi_A \phi_C$	pressure angle at points A and C respectively
$\phi_p$	pressure angle at pitch point (normal pressure angle)
$\phi_{PL}$	pressure angle at pitch point "loaded side"
$\phi_{PU}$	pressure angle at pitch point "unloaded side"
$\psi$	angular displacement
$\omega$	transformation function

List of Figures

	Page
2.1 Lewis Layout with Tip Loading [4]	17
2.2 Dolan & Broghamer's Set Up [11]	19
2.3 Radius of the Highest Point for Single Tooth Contact ( $R'_H$ ) (for the driver gear)	21
2.4 Heywood's Construction [16]	23
2.5 Kelley & Pedersen's Construction [18]	23
2.6 Stress Sensitivity - R.W. Cornell [8]	28
2.7 Contour of Finite Element Model, Asymmetric Tooth - Wilcox & Coleman [31]	31
2.8 Tooth Layout - Wilcox & Coleman [31]	31
2.9 Layout of Finite Element Model - Chabert et al. [7]	34
2.10 Layout, Wedge Principle, Shottter [27]	36
2.11 Mapping of the Tooth Form into a Straight Edged Half Plane - Baronet & Tordion [5], Aida & Terauchi [1]	38
2.12 Aida & Terauchi Layout [2]	40
2.13 Compliance, Layout - Weber [29]	44
2.14 Contact Deformation and Pressure Distribution - Weber [29]	44
2.15 Load Sharing - Chabert et al. [7]	49
2.16 Beam Compliance - Cornell [8]	51
2.17 Fillet and Foundation Compliance - Cornell [8]	51
2.18 Local Compliance - Cornell [8]	54
3.1 Static Model for High Contact Ratio Tooth Engagement	59
3.2 Fatigue Diagram	59
4.1 Tooth Form - Pinion	66
4.2 Tooth Form - Wheel	66

List of Figures (Cont'd)

	Page
4.3 Involute Tooth Profile	68
4.4 Fillet Layout	71
4.5 Tip Modification	75
4.6 Profile Adjustment Set Up, Mounting of the Model	78
4.7 Profile Adjustment Set Up, Guide for Abrasive Tool	79
4.8 Experimental Set Up - Frontal View	81
4.9 Experimental Set Up - Side View	82
4.10 Polariscope and Straining Rig (Photograph)	84
5.1 Matching Radii	86
5.2 Points of Simultaneous Contact	87
5.3 Loading Layout	92
6.1 Load Sharing - Tentative Dynamic Program	104
6.2 Finite Element Model - Wheel	105
6.3 Finite Element Grid, Close Up - Wheel	106
6.4 Finite Element Grid, Close Up - Typical Loading Site	107
6.5 Finite Element Model - Pinion	108
6.6 Finite Element Grid, Close Up - Pinion	109
6.7 Deflected Shape - Pinion	111
6.8 Isostress Lines, Major Principal Stresses - Pinion	112
6.9 Isostress Lines, Minor Principal Stresses - Pinion	113
6.10 Layout of Elliptic Load Distribution	116
7.1 Fillet Stresses vs Angular Position, Single Engagement - Wheel, $S' = -1.00$	122
7.2 Fillet Stresses vs Angular Position, Single Engagement - Wheel, $S' = 0$	123

List of Figures (Cont'd)

	Page
7.3 Fillet Stresses vs Angular Position, Single Engagement - Wheel, $S' = 1.33$	124
7.4 Fillet Stresses vs Angular Position, Single Engagement - Pinion, $S' = -1.00$	125
7.5 Fillet Stresses vs Angular Position, Single Engagement - Pinion, $S' = 0$	126
7.6 Fillet Stresses vs Angular Position, Single Engagement - Pinion, $S' = 1.33$	127
7.7 Peak Tensile Stresses and their Angular Location vs $S'$ (Normalized Position Along the Line of Action), Single Engagement - Wheel	128
7.8 Peak Compressive Stresses and their Angular Location vs $S'$ , Single Engagement - Wheel	129
7.9 Peak Tensile Stresses and their Angular Location vs $S'$ , Single Engagement - Pinion	130
7.10 Peak Compressive Stresses and their Angular Location vs $S'$ , Single Engagement - Pinion	131
7.11 Photoelastic Fringe Pattern - Single Pair Engagement (Photograph)	133
7.12 Fillet Stresses vs Angular Position, Multiple Engagement - Wheel, $S'_{nom} = 0$	135
7.13 Fillet Stresses vs Angular Position, Multiple Engagement - Wheel, $S'_{nom} = .33$	136
7.14 Fillet Stresses vs Angular Position, Multiple Engagement - Wheel, $S'_{nom} = .82$	137
7.15 Fillet Stresses vs Angular Position, Multiple Engagement - Pinion, $S'_{nom} = 0$	138
7.16 Fillet Stresses vs Angular Position, Multiple Engagement - Pinion, $S'_{nom} = .33$	139
7.17 Fillet Stresses vs Angular Position, Multiple Engagement - Pinion, $S'_{nom} = .82$	140
7.18 Peak Tensile Stresses vs $S'$ , Multiple Engagement - Wheel	141

List of Figures (Cont'd)

	Page
7.19 Peak Tensile Stresses vs $S'$ , Multiple Engagement - Pinion	142
7.20 Photoelastic Fringe Pattern - Multiple Pair Engagement (Photograph)	143
7.21 Deflection vs Load, $S' = -.67$	145
7.22 Deflection vs Load, $S' = 0$	146
7.23 Deflection vs Load, $S' = 1.00$	147
8.1 Compliance vs $S'$ - Experimental	149
8.2 Compliance vs $S'$ - from Finite Elements and Experimental	151
8.3 Branch Loads in Multiple Engagement - Experimental	153
8.4 Branch Loads in Multiple Engagement - Summary	154
8.5 Load Gauge Stresses vs $S'$ - Tensile	156
8.6 Load Gauge Stresses vs $S'$ - Compressive	157
8.7 Load Sharing, Using Deflections, $S'_{nom} = -.43$	159
8.8 Load Sharing, Using Deflections, $S'_{nom} = 0$	160
8.9 Load Sharing, Using Deflections, $S'_{nom} = .82$	161
8.10 Stress Sensitivity vs $S'$ - Experimental	163
8.11 Stress Admittance vs $S'$ - Experimental	164
8.12 Stress Excursion - Wheel, Pressure Side, $\gamma = 40^\circ$	167
8.13 Stress Excursion - Wheel, Lee Side, $\gamma = -33^\circ$	168
8.14 Stress Excursion - Pinion, Pressure Side, $\gamma = 40^\circ$	169
8.15 Stress Excursion - Pinion, Lee Side, $\gamma = -26^\circ$	170
8.16 Equivalent Static Alternating Stresses	173
9.1 Sliding Component due to Deflection vs $S'$	175

LIST OF TABLES

	Page
4.1 Gear Data	65
5.1 Loading Scheme	94
6.1 Non-Dimensional Load Fractions	117
8.1 Equivalent Alternating Stresses - Wheel	171
8.2 Equivalent Alternating Stresses - Pinion	172

INTRODUCTION

The term "High Contact Ratio Gearing" implies that the average number of teeth being in contact at a given time is high in contrast with the "conventional" Low Contact Ratio Gearing. Usually High Contact Ratio Gearing involves 2 to 4 pairs of teeth in contact at a given time. A decrease in load per tooth may be therefore attained. However the pressure angles would be lower, the pitch may become finer, thus the relative stressing of the fillet would increase. With more teeth acting at the same time the sensitivity to manufacturing errors could be critical. At such conflicting conditions the analysis must be increasingly precise.

There are a number of analytical approaches available for the evaluation of gear tooth designs, each attempting to cover the most common practical cases. By stepping from low contact ratio (1.2 to 1.6) to high contact ratio practice, caution must be exercised. The new conditions may exceed the range of validity for a previously proven method.

The opening market for HCRG and the increased demands for accurate analysis warrants an experimental effort to contribute to the choice of an economical and reliable analytical tool.

The literature on the subject is first investigated, so repetitions may be avoided, and the efforts may be focused on areas not adequately covered.

LITERARY SURVEY

The low pressure angles at which HCRG operate, shift the critical stresses to the fillet area. Therefore articles dealing with fillet stresses will be explored first.

As the load carried by an individual tooth depends greatly upon how the total load is shared, the flexibility of the tooth gains increased importance. For this reason papers examining the compliance of gear teeth will be considered afterwards.

The analytical methods for finding the fillet stresses may be grouped under four headings.

- 1) Short beam model approach -
- 2) Finite Element analysis
- 3) Isotropic Wedge Theory
- 4) Theory of Elasticity approach, using complex potential functions and conformal transformation.

The material below is listed along these lines.



## 2.1.0 Stress Sensitivity - Short Beam Model Approach

### 2.1.1 The Lewis Equation [26], [37]

The historic first was attributed to Wilfred Lewis (1892). A parabola of "equal strength" was fitted into the tooth outline.

(Fig. 2.1). The load line is extended to the radial centerline of the tooth giving the apex of the parabola. The "weakest section" AA' is obtained by drawing a tangent to the fillet radius such that AB = BE. To this section, elementary beam theory is applied.

The formula announced in 1892 for the bending stress of the gear tooth is:

$$\sigma_t = \frac{W_t}{pBy_1} \quad (2.1)$$

where  $W_t$  is the transmitted (tangential) load

$p$  is the circular pitch

$B$  is the face width of the tooth

$y_1$  is the dimensionless "Lewis form factor", which depends upon the form of the tooth.

Using Fig. 2.1 it may be shown how this expression is linked to the beam theory. By similar triangles shown in dashed lines:

$$\frac{t/2}{x_1} = \frac{l'}{t/2} \quad \text{therefore } x_1 = \frac{t^2}{4l'} \quad (2.2)$$

The stress at "A" due to the tangential component of the load:

$$\sigma_t = \frac{M}{I/c} = \frac{6W_t l'}{Bt^2} = \frac{W_t}{B} \cdot \frac{l'}{t^2/6l'} = \frac{W_t}{B} \cdot \frac{1}{t^2/4l'} \cdot \frac{1}{4/6}$$

multiplying the numerator and the denominator by  $p$  and substituting  $x_1$  from Eq. (2.2)



$$\sigma_t = \frac{W_t}{B (x_1/p) (2/3)p}$$

Letting the form factor  $y_1 = \frac{2x_1}{3p}$  Eq. (2.1) is obtained.

### 2.1.2 Dolan & Broghamer - Stress Concentration Factor [12]

It was soon discovered that the Lewis formula gave grossly inaccurate results. Following a few early investigators such as S. Timoshenko [39], R.V. Baud [33], R.E. Peterson [34], P.H. Black [35], Dolan and Broghamer made the first extensive study to isolate those parameters which influence the fillet stresses most.

Eleven models were made of bakelite, incorporating a systematic variation of load position, number of teeth, pressure angle, addendum proportions, fillet size, and fillet shape.

Each model consisted of a middle tooth and two halves of the neighboring teeth, as in Fig. (2.2). They were held in a rigid frame (1). Deadweight loading was transmitted by a half wedge (2), through a thin cellulose strip (3) protecting the model.

After careful measurements and analysis the parameters were organized into the shape of the well known stress concentration factor formulas for the tensile fillet. For nominal pressure angles of:

$$\phi_p = 14\frac{1}{2}^\circ \quad K = .22 + (t/r_f)^{0.2} (t/l)^{0.4} \quad (2.3)$$

$$\phi_p = 20^\circ \quad K = .18 + (t/r_f)^{0.15} (t/l)^{0.45} \quad (2.4)$$

The factors above include the direct effect of the radial load and increase significantly the nominal stresses obtained by the Lewis formula. The use of these expressions is discouraged for angles other than indicated.

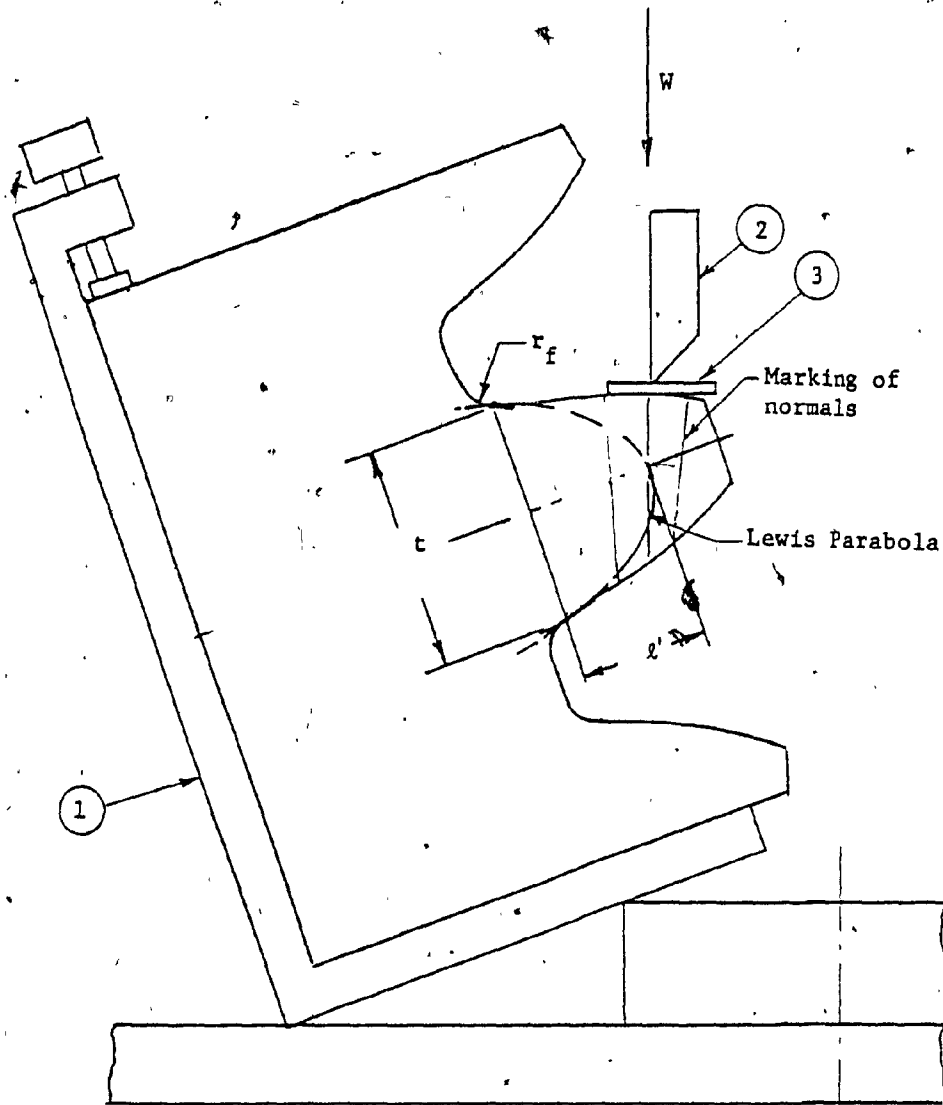


FIG. 2.2: DOLAN & BROCHAMER'S SET-UP [12]

These stress concentration factors constitute an important feature of the "Modified Lewis formula", which along with other considerations forms the basis of the AGMA standard described below.

### 2.1.3 The AGMA Standard [4]

This standard has received wide acceptance. It stipulates a series of service factors providing a guide for design. Modifications were introduced to the Lewis formula, which in its revised form constitutes the core of the standard.

$$\sigma_t = \frac{W_t P_d}{B J} \quad (2.5)$$

where  $P_d$  the diametral pitch has replaced the circular pitch, and

$J$  a "geometry factor" was introduced.

$$J = \frac{Y}{K_f m_n} \quad (2.6)$$

where  $K_f$  is a stress correction factor, essentially Dolan &

Broghamer's stress concentration factor.

$m_n$  is the load sharing ratio. For conservative estimates tip

loading is assumed and it is taken as unity.

The new form factor  $Y$  is defined by the expression:

$$Y = \frac{1}{\cos \lambda \left( \frac{1.5}{x_1} - \frac{\tan \lambda}{t} \right) \cos \phi_p} \quad (2.7)$$

where  $x_1$  &  $t$  is read from the layout as in Fig. (2.1)

The second term in the denominator accounts for the direct effect of the radial component of the load, as it was proposed by Merrit [38] (1938). The moment effect of the same is ignored.



When the designer is confident that manufacturing can keep profile errors at very low values, he may assume that load sharing does exist at each and every mesh. Then the critical load may be placed to the "Highest Point for Single Tooth Contact" (HPSTC). The term tacitly infers LCR gearing. The radial position of this point may be found for the driver gear using Fig. (2.3). Essentially the length of one base pitch is measured forward from point E, the engagement end of the line of action. To find  $R_H$ , the position of the HPSTC for the driven gear, point D the end of the disengagement branch is used as datum.

The Y form factor is then determined similarly as before except the load is located at the HPSTC.

For standard tooth forms the values for Y are available in tabular form. For non-conventional designs however an accurate layout or computation is still necessary.

The accuracy of the "Modified Lewis formula" is far from being satisfactory for the new industrial demands. The following researchers are all attempting to improve the accuracy using various approaches.

#### 2.1.4 R.B. Heywood - Gear Tooth as a Projection (1948)[17][18]

This author used photoelasticity in his investigation of the behaviour of loaded projections. The scope of his work is quite general. It deals with screw threads and other protruding structural elements, symmetric or skewed, bounded by flat flanks of any practical incline.

For the extension of his analysis to gear teeth the curved flank of the tooth was transformed to an equivalent straight sided projection shown in Fig. (2.4).

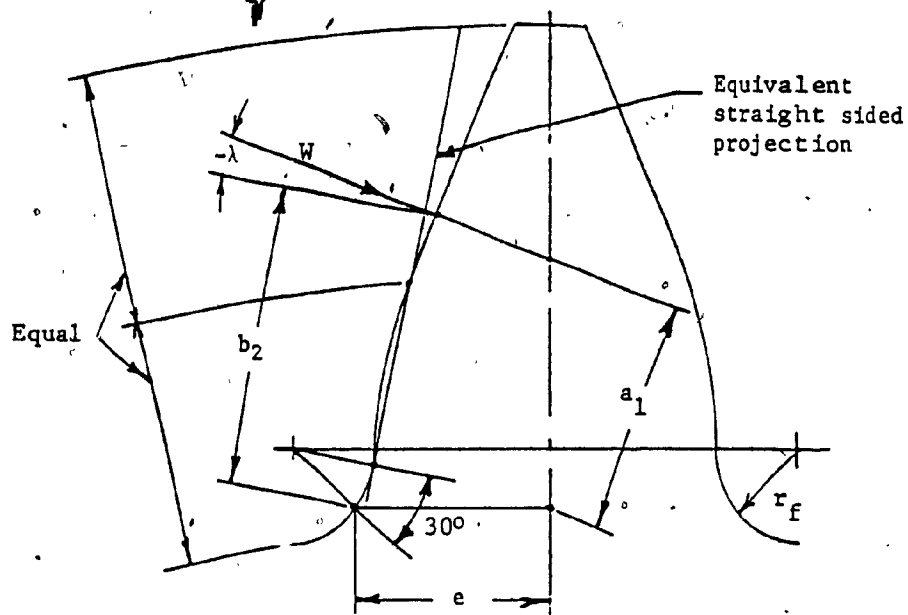


FIG. 2.4 HEYWOOD'S CONSTRUCTION [18]

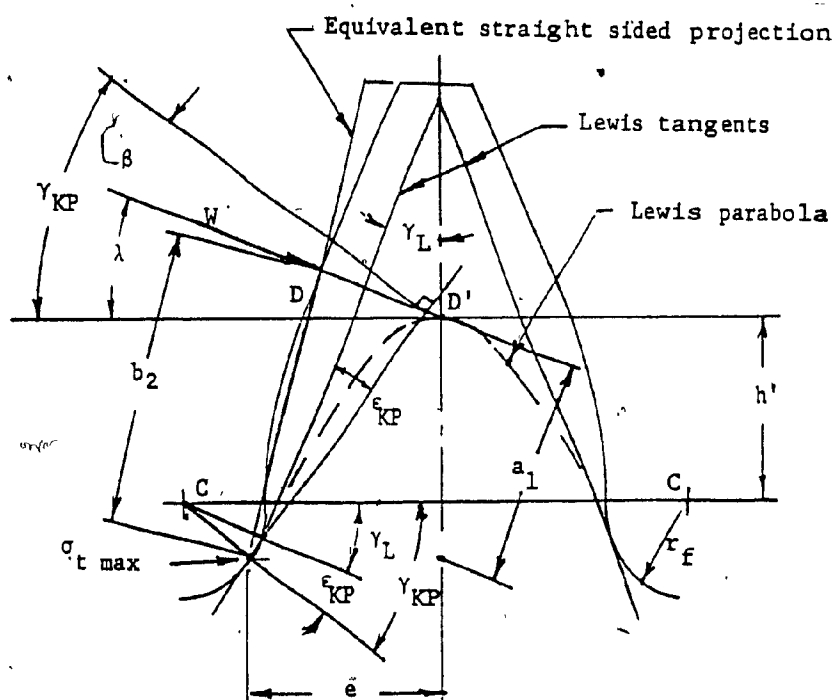


FIG. 2.5 KELLEY - PEDERSEN CONSTRUCTION [20]



In the analysis of the gear problem first it is explained that the Lewis approach is unsound. The simple bending formula was intended for long parallel beams, not for short tapered shapes. Also the load is much too close to the fillet so its "proximity" can not be ignored.

The photoelastic measurements were regarded as the undisputed true stresses, and a formula was constructed to fit the results. The effect of "proximity" was isolated and is given as the second term in the second bracket below.

The maximum tensile fillet stress:

$$\sigma_t = \frac{W}{B} \left[ 1 + .26 \left( \frac{e}{r_f} \right)^{0.7} \right] \left[ \frac{1.5 a_1}{e^2} + \left( \frac{.36}{b_2 e} \right)^{\frac{1}{2}} \left( 1 + \frac{\sin \lambda}{4} \right) \right] \quad (2.10)$$

The stress concentration factor depends upon a single ratio, it was found independent of the load height, cf Eq's. (2.3 & 2.4).

No attempt was made to construct a formula for the compressive stresses.

#### 2.1.5 M.A. Jacobson - Proximity Effects (1955)[19]

This author emphasizes the importance of careful experimental practices.

His main contribution to the art was the demonstration of the proximity effects. He shows that as the load approaches the fillet area, the tensile fillet stresses start to increase again. This happens in spite of the diminishing bending moment.

2.1.6 B.W. Kelley and R. Pedersen - The Contemporary State of the Art and a New Formula [20]

These authors have analysed and compared the afore mentioned methods and test results, including their own, and an improved formula was proposed.

Their original objective was to find a stress concentration factor formula for  $25^\circ$  pressure angle, similar to those established by Dolan and Broghamer.

It was soon found that no unique constant would satisfy large and small tooth numbers equally. This lead the authors to scrutinize the construction of the Lewis parabola and that of Heywoods equivalent flat sided projection. Also the shape of the fillets was more closely examined.

The radius of curvature of trochoidal fillets, which are produced by rack type tools in a generation process, has its minimum value as it blends with the root radius. From this point it increases gradually toward the involute. It is reasonable therefore to adopt for stress calculations the actual fillet radius at the location of maximum stress.

It was observed, that as the load moved toward the tip, the location of the peak stress shifted toward the involute. The parabolic construction in the Lewis layout does not give the right location, but moves it in the proper direction with the variation of:

a) load position, b) beam depth and c) the "taper" of the tooth shape.

The Heywood construction is not sensitive to this "stress shift". Once the taper of the equivalent straight side is determined, a

constant  $30^\circ$  is taken for the location of the max. stress from the point of tangency, as shown in Fig. (2.4) p 23.

A hybrid process was proposed. The Lewis parabola was chosen as the basis of the construction, as in Fig. (2.5) p 23. The location of the maximum stress was determined by the "stress shift" expression Eq. (2.11) below. The structure of the stress formula resembles that of Heywood.

Kelley and Pedersen have observed that the angle between the Lewis tangent and the tangent to the fillet at the point of the maximum stress may be closely approximated by

$$\epsilon_{KP} = 25^\circ - \gamma_L \quad (2.11)$$

where  $\epsilon_{KP}$  is the angular shift of the maximum tensile stress which is the angle between the above tangents.

$\gamma_L$  is the angle between the Lewis tangent and the centerline of the tooth.

The maximum fillet stress is:

$$\sigma_t = \frac{W}{B} \left[ 1 + 0.26 \left( \frac{e}{r_f} \right)^{0.7} \right] \left[ \frac{1.5a_1}{e^2} + \frac{\sin \beta}{2e} + \frac{0.45}{(b_2 e)^{\frac{1}{2}}} \right] \quad (2.12)$$

where  $\beta$  is the acute angle between the direction of the load and the set of principal stresses at the "critical point", (Fig. 2.5), p 23.

The proximity terms are somewhat different from those of Heywood. Neither of them are based on the laws of physics, they both are purely empirical but Kelley and Pedersen's terms fit the results better. It is claimed that the formula may be applied also to concave sided internal gears.

They conducted also some fatigue tests in support to their formula and found excellent correlation at stress levels near the endurance limit. The significance of the "range of stress" is mentioned with respect to residual stresses. In the carburized layers large compressive stresses are locked in by quenching. These superimposed onto the service stresses give an entirely new set of fatigue conditions.

#### 2.1.7 I.M. Allison and E.J. Hearn - Effects of Friction [3]

The article deals with a wide range of conditions effecting the bending strength of gear teeth. However the role of friction should be mentioned here.

It was shown that frictional forces at the contact may alter the stress pattern radically. Gear performance is only slightly affected since lubrication usually keeps  $\mu < 0.1$ . However friction may become a major source of error in photoelastic tests where  $0.3 < \mu < 0.6$  under static conditions is typical. It is shown, that with  $\mu = 0.3$  a 40% change in the fillet stresses may be experienced.

#### 2.1.8 R.W. Cornell's Expression for Fillet Stresses [8]

This study is part of a wider computerized effort for finding the fillet stresses under dynamic conditions [9]. The static analysis is described below, the layout and nomenclature are shown in Fig. (2.6).

This author found that the Heywood formula gives equally close results for LCRG and HCRG cases. Hence it was adopted with some changes. Term (3) below was adjusted for the bending component of the load. In term (4) the factor .25 was replaced by the Poisson's ratio and it was made more sensitive to the proximity of the radial load by employing the ratio  $t_L/t_s$ . Term (5) for the radial load was added.

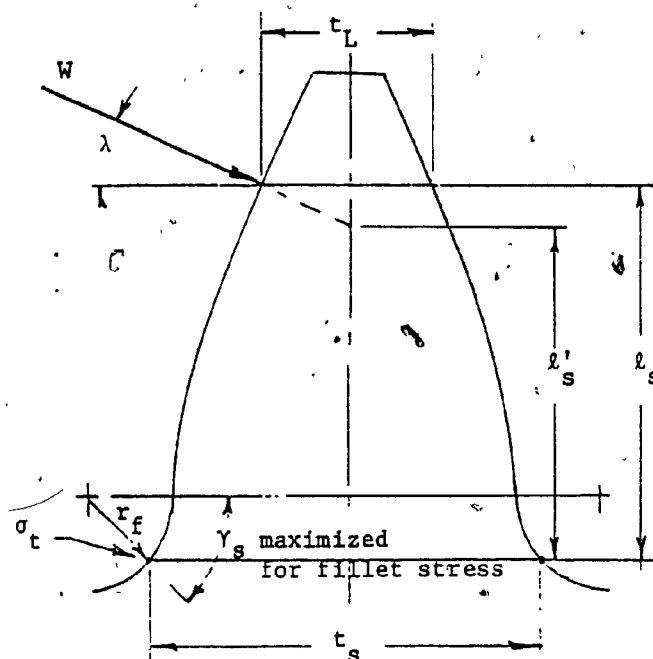


FIG. 2.6 STRESS SENSITIVITY, R.W. CORNELL [8]

The modified Heywood formula was given in a normalised form:

$$\frac{\sigma_t B}{W \cos \lambda} = \left[ \underset{1}{1 + .26 \left( \frac{t_s}{2r_f} \right)^{0.7}} \right] \left[ \underset{2}{\frac{6l'_s}{t_s^2}} + \left( \frac{.72}{t_s l_s} \right)^{\frac{1}{2}} \left( \underset{3}{1 - \frac{t_L}{t_s} \nu \tan \lambda} \right) - \underset{4}{\frac{\tan \lambda}{t_s}} \right] \quad (2.13)$$

where factor (1) is the stress concentration factor

term (2) is the beam cantilever stress

(3) is the proximity stress due to the bending

(4) is the proximity stress due to the radial load

(5) is the direct stress due to the radial load

The location of the maximum fillet stress is considered to be a variable. It is determined in terms of fillet angle  $\gamma_s$  in a computerized process which maximizes, the fillet stress. After  $\gamma_s$  is found  $t_s$ ,  $l_s$  and  $l'_s$  can be calculated.

The results were compared with stresses obtained by other close form solutions, tests and by "analytic transformation" [5] and good correlation was found.

## 2.2 Stress Sensitivity - Finite Element Method

This is the most widespread tool of stress analysis for continua in the computer age. Therefore its application to the gear problem is of primary importance.

The method does not yield a general solution, it gives rather a specific answer to a specific question. It is however extremely suitable for parametric studies so data may be accumulated economically for building up a closed form empirical formula. In this context the finite element method may be regarded as "numerical experimentation".

### 2.2.1 L. Wilcox & W. Coleman's Polynomial Formula (1973) [31]

These authors developed empirical expressions for standard addendum symmetric and asymmetric involute tooth profiles from data generated by finite elements. The variation of pressure angles and tool edge radii gave nine symmetric and six asymmetric models.

The position of the load was varied from tip to pitch line. The equation developed is similar in structure to that of Kelley and Pedersen [20].

$$\sigma_t = K S_{CB} K_1 \quad \text{for the symmetric and} \quad (2.14)$$

$$\sigma_t = K S_{CB} U \quad \text{for the asymmetric cases.} \quad (2.15)$$

where  $S_{CB}$  is the basic beam bending stress.

The stress concentration factor:

$$K = 0.939 \left( \frac{t}{r_f} \right)^{0.256} \quad (2.16)$$

$K_1$  and  $U$  are the "balanced and unbalanced residual factors" for symmetric and asymmetric tooth forms respectively. All the hard to account for radial, shear, proximity etc. effects are cast into these coefficients.

$K_1$  is expressed with a power series of 2<sup>nd</sup> degree in terms of a nondimensional load height, as in Fig (2.8).

$$K_1 = B_1(\phi_p) + C_1(\phi_p) \left( \frac{l}{l_t} \right) + D_1(\phi_p) \left( \frac{l}{l_t} \right)^2 \quad (2.17)$$

$B_1$ ,  $C_1$  and  $D_1$  are functions of pressure angle and are assumed to have the form:

$$B_1(\phi_p) = b_1 + c_1 \left( \frac{\phi_o}{\phi_p} \right) + d_1 \left( \frac{\phi_o}{\phi_p} \right)^2 \quad (2.18)$$

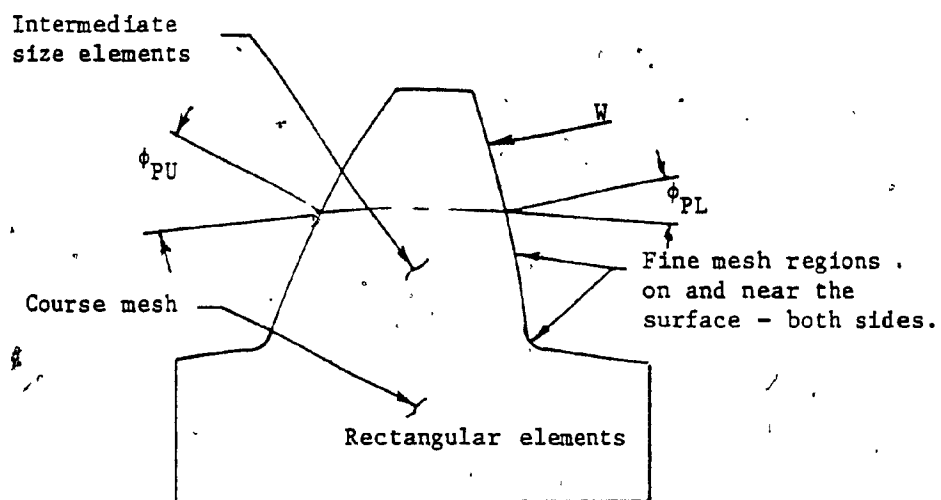


FIG. 2.7 CONTOUR OF FINITE ELEMENT MODEL  
ASYMMETRIC TOOTH - WILCOX & COLEMAN [31]

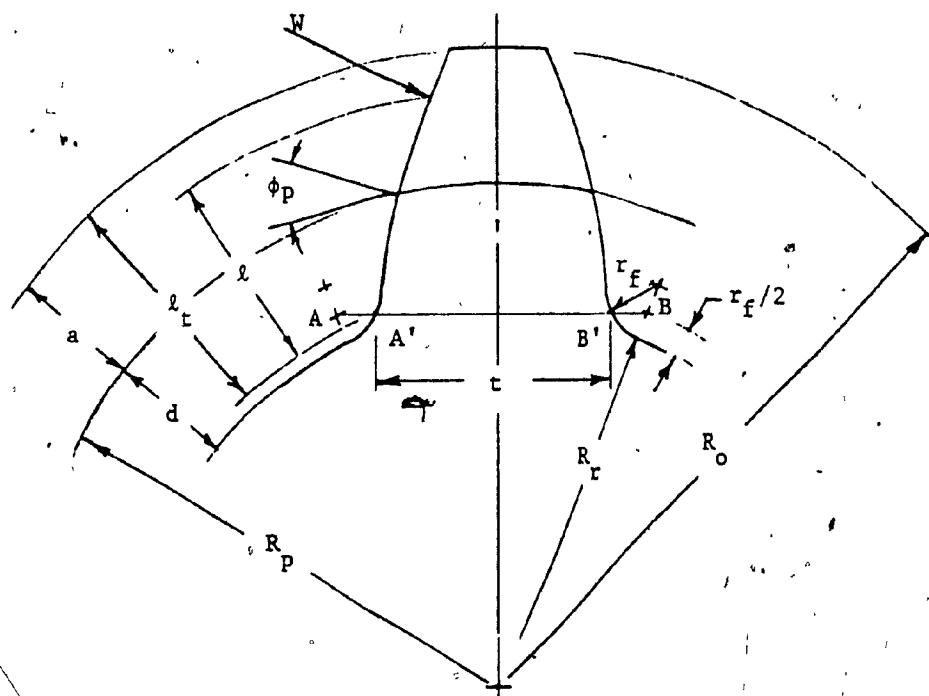


FIG. 2.8 TOOTH LAYOUT - WILCOX & COLEMAN [31]



where  $\phi_0$  is an arbitrary choice of pressure angle, to have the expression nondimensional. The constants  $b_1, c_1, d_1$  are determined from the finite element results and solving systems of (three) equations.  $C_1(\phi_p)$  and  $D_1(\phi_p)$  are determined in a similar manner, a quadratic equation of nine terms was obtained.

U the unbalanced residual plays a similar roll for asymmetric tooth forms. A cubic equation of (16) terms determines this factor.

The nondimensional pressure angle here is expressed as 
$$\frac{\phi_{PL} - \phi_{PU}}{\phi_{PL} + \phi_{PU}}$$

where the indices PL and PU refer to the loaded and "unloaded" sides.

Good agreement is found with the photoelastic results of Dolan & Broghamer [12] and Kelley and Pedersen [20]. It remains to be seen that the formula would apply to modified addendum cases, as the constants were found by using standard addendum proportions. The constants are published in the article, thus they may be readily adapted to a programable hand calculator.

The investigators used constant strain type rectangular elements. In the low gradient regions the size of the elements was approximately 10% of tooth height. In the fillet area this size was reduced to 2%. To obtain reasonable surface stresses numerical averaging and hyperbolic extrapolation was applied.

In a later paper [32] they report having used isoparametric elements. Substructuring was employed to handle the large number of elements in acceptable computation time.

2.2.2 G. Chabert, T. Dang Tran, R. Mathis's (1974)  
Expressions for Tensile and Compressive Fillet Stresses [7]

An article which extends this survey to the continental Europe.

The scope of this investigation is narrower than that of ref. [31].

20° nominal pressure angle, standard addendum symmetric profile of the European module system was examined, (Fig. 2.9). The tool edge radius, number of teeth and the load positions were varied in the finite element experiment.

From the results closed form expressions were developed for the peak tensile and also for the maximum compressive fillet stresses expressed in  $N/mm^2$ .

$$\sigma_t = \left[ 3 + \frac{1}{N} \left( 38 - 50 \frac{r_f}{m} \right) \right] \frac{W}{B m m_c} \quad (2.19)$$

for  $12 < N \leq 50$

$$\sigma_c = \left[ 3.5 + \frac{1}{N} \left( 41 - 50 \frac{r_f}{m} \right) \right] \frac{W}{B m m_c} \quad (2.20)$$

where  $N$  is the number of teeth

$W$  the normal load [N]

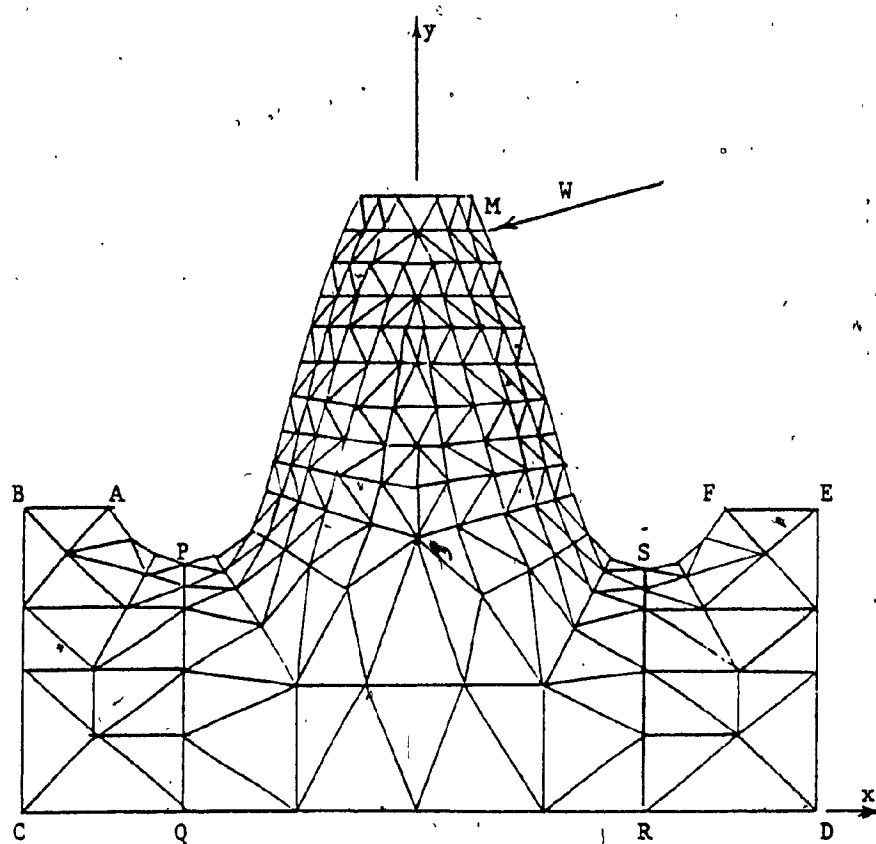
$r_f$  the fillet radius [mm]

$B$  the face width [mm]

$m$  the module [mm]

$m_c$  is the contact ratio

Triangular elements with midside nodes are used. The density of the elements around the fillets and along the flanks are approximately 10% of the tooth height. There is no reference if any adjustments were made to compensate for the size and limitations of the elements.



The reduced area is bounded by lines PQ and RS

FIG. 2.9 LAYOUT OF FINITE ELEMENT MODEL - CHABERT ET AL  
Taken from FIG. (1) ref. [7]

### 2.3 Stress Sensitivity - Isotropic Wedge Theory

From the point of loading tangents are drawn to each fillet, thus a wedge is obtained. The known solution of two dimensional theory of elasticity for an isotropic wedge under a point load of arbitrary orientation is applied.

This solution is credited to Mitchell J.H. (approximately 1900) and may be found in Timoshenko & Goodier's Theory of Elasticity [28].

#### 2.3.1 B.A. Shotter's Wedge Stresses and the Most Damaging Stress Range [27]

The inadequacy of the beam approach is even more true for high strength tooth forms, such as the Wildhaber & Novikoff circular arc profile, than for involute shapes. It was found that when for manufacturing convenience the fillet depth was increased on such tooth shapes, the stresses have decreased unexpectedly.

Apparently the close proximity of the contact surpassed the bending moment in stressing the fillet. Therefore the elasticity solution of an isotropic wedge was applied. For an arbitrarily oriented load the maximum tensile and compressive stresses are:

$$\sigma_t = \frac{2W}{r_t B} \frac{\alpha_3 \cos \alpha_2 - \sin \alpha_3 \cos \alpha_1}{\alpha_3^2 - \sin^2 \alpha_3} \quad (2.21)$$

$$\sigma_c = \frac{2W}{r_c B} \frac{\alpha_3 \cos \alpha_1 - \sin \alpha_3 \cos \alpha_2}{\alpha_3^2 - \sin^2 \alpha_3} \quad (2.22)$$

where  $r_t$  &  $r_c$  are the radial distances from the point of load application to the tangencies on the tensile and compressive fillets respectively, as shown in Fig. (2.10).

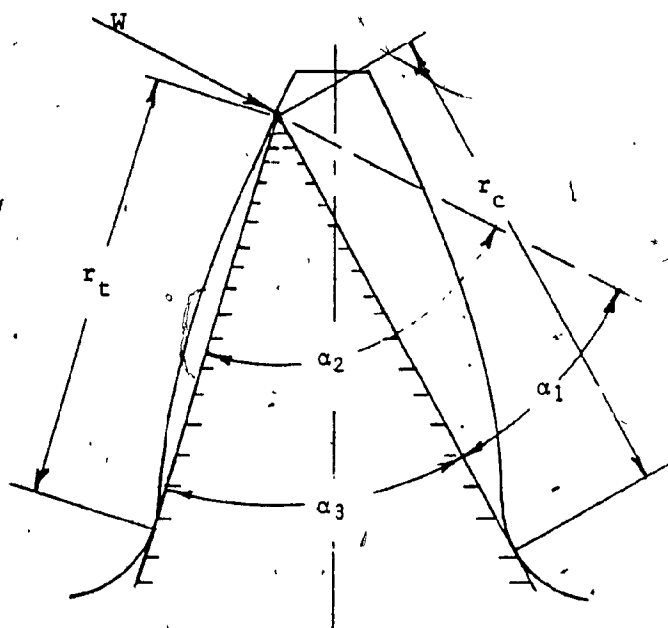


FIG. 2.10 LAYOUT, WEDGE PRINCIPLE - SHOTTER [27]

It must be noted, that for these equations to hold, the stress distribution must remain purely radial ref. [28], p 112. This is unlikely to be the case at the reactions near the fillets, where it matters the most.

The article deals also extensively with the nature of fatigue failure. It is emphasized, that the maximum tensile stress is not sufficient for the determination of the fatigue life of the gear, even if it was known precisely. The full distribution of the stresses around the fillets are needed for a whole load cycle to find their most damaging stress range.

#### 2.4.0 Stress Sensitivity - Theory of Elasticity Solution, Using Complex Potential Functions and Conformal Transformation

The theory of elasticity derives the stresses and the deflections from the Airy stress function. The complex potential theory relates the stress function to certain analytic functions, the so called complex potentials. Hence the stresses may be expressed in general terms of these complex potentials.

The curved edge of the tooth profile is transformed to a straight edge of an infinite half plane using conformal mapping (Fig. 2.11). The boundary conditions on this straight edge allow the complex potentials to be specified. As the stresses in the plane of curved contours are expressed in terms of the complex potentials now with specific functions, a solution is obtained.

#### 2.4.1 T. Aida & Y. Terauchi

These authors are credited with being the first to apply this two dimensional elasticity solution using curvilinear coordinates to the

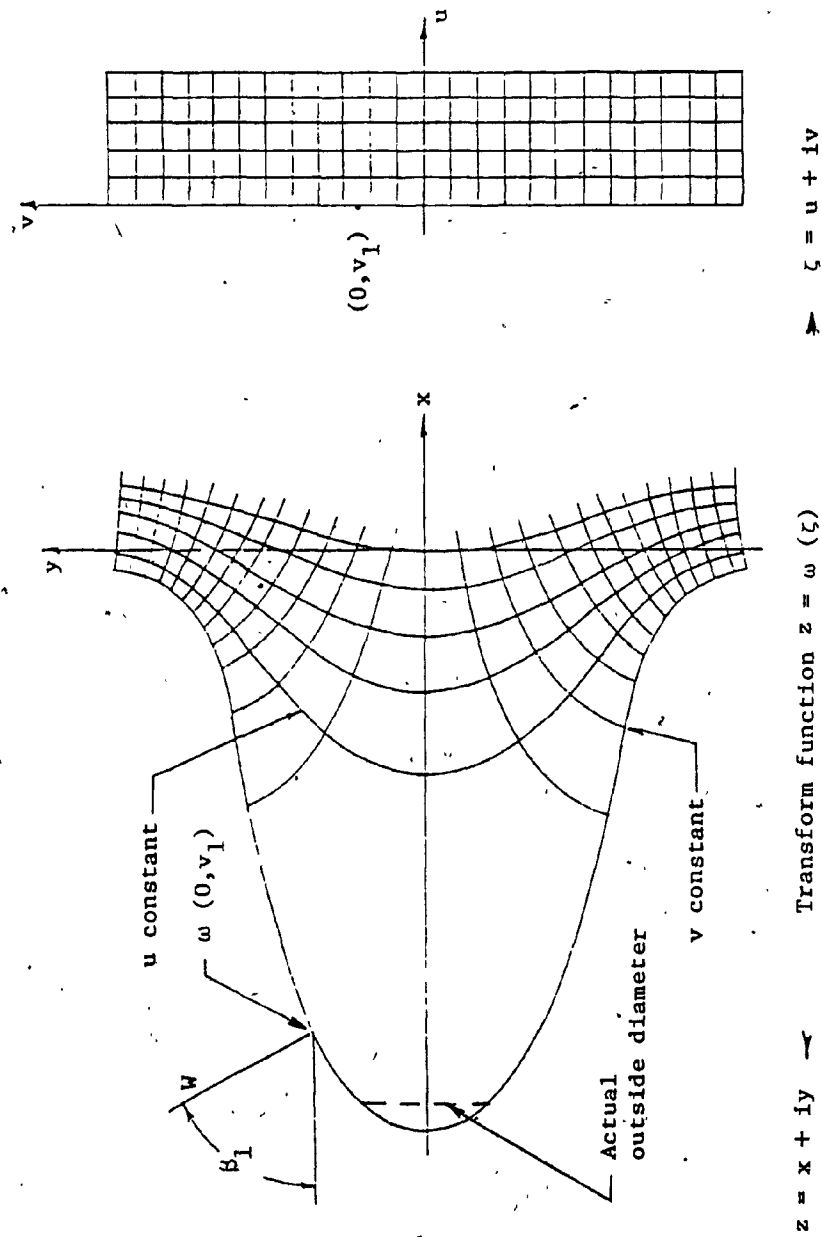


FIG. 2.11 MAPPING OF THE TOOTHFORM INTO A STRAIGHT EDGED HALF PLANE  
 Taken from: BARONET-TORDION [5], AIDA-TERAUCHI [1].

gear problem. The derivation and even the application is quite involved, its proper presentation is beyond the scope of this study.

Aida and Terauchi have realized, that the complex potential method is not suitable for every day practice, therefore they constructed a utility formula, which gives stresses reasonably close to those obtained previously.

The loads were resolved into tangential and radial components and "nominal stress elements" were selected corresponding to the load components. The layout and nomenclature is shown in Fig. (2.12). The nominal bending stress is:

$$\sigma_b = \frac{6Wl \cos \lambda}{Bt^2}, \quad (2.23)$$

where  $B$  is the face width of the tooth.

The nominal direct compressive stress, including the effect of its moment about the centerline of the tooth:

$$\sigma_r = - \frac{W \sin \lambda}{Bt} - \frac{6Wa_1 \sin \lambda}{Bt^2}, \quad (2.24)$$

and the nominal shear component:

$$\tau = \frac{W \cos \lambda}{Bt} \quad (2.25)$$

These nominal stress components were compared with the stresses obtained under the respective loads by the complex potential method. The process has lead to the establishment of weighting factors for each stress component and an expression for the stress concentration factor. The latter is the quantity in the first parenthesis below. The maximum tensile stress is:



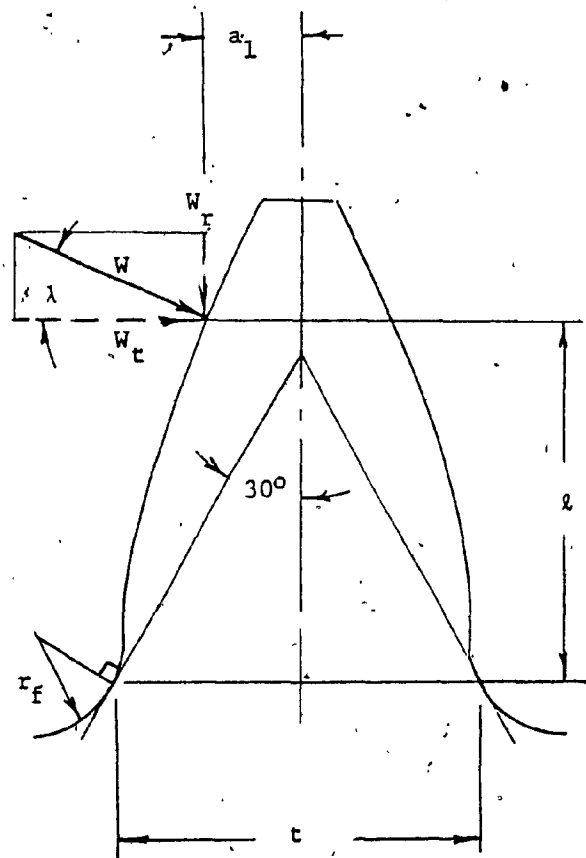


FIG. 2.12 AIDA-TERAUCHI LAYOUT [2]

$$\sigma_t = \left( 1 + 0.8 \frac{t}{r_f} \right) [ .66 \sigma_b + .40 (\sigma_b^2 + 36\tau^2)^{\frac{1}{2}} + 1.15 \sigma_r ] \quad (2.26)$$

The rational structure of the formula suggests that it may be employed in a more general sense. This observation was used later by the writer to extend the usefulness of the formula for compressive peaks, and for analysing frictional effects.

Aida and Terauchi investigated the accuracy of Hofer's method for finding the "weakest section", which is the same 30° tangency from the tooth centerline as it was done by Heywood [18]. It was found that the location of the tensile peak varies from 24° to 36.8°. It is claimed that the choice of a constant 30° leads to an underestimate of  $\sigma_{\max}$  by not more than 5%.

They also performed a series of photoelastic tests to verify the formula. Good agreement was found for those shapes which resemble genuine tooth forms, even for low dedendum loading cases. To obtain a better representation of true gear shapes, it was realized that more than three terms are needed in the mapping function. This was achieved by the authors of the next article.

#### 2.4.2 C.N. Baronet, G.V. Tordion's "Exact Stress Distribution" (1970)[5]

Simultaneously with Aida and Terauchi's paper [1], V.L. Ustinenko [40] published a similar solution using five terms in the mapping function. The calculations were performed for the standard European tooth form. Baronet and Tordion used a similar transform function and computed the stresses for American Standard tooth shapes. Using these

five terms a straight line may be mapped almost perfectly into a gear tooth profile, as in Fig.(2.11) p 38. Only the discontinuity at the tip is rounded off with little effect on the stresses.

The eight constants for the transform function were determined by trial and error. They are given in tabular form for 20° and 25° pressure angles and standard addendum proportions for six different tooth numbers at the end of the article. The stresses are expressed by the "Modified Lewis formula":

$$\sigma_{\max} = \frac{W_t P_D}{B J(t \text{ or } c)} \quad (2.27)$$

where  $J_t$  and  $J_c$  are geometry factors for the tensile and compressive sides respectively and are given in tabular form.

It is unfortunate that the results are compared only with one source which was also obtained by computation. Some supporting evidence from a photoelastic experiment would be desirable.

### 2.5.0 Survey - Investigating Tooth Compliance

To find the dynamic loading on a structure it is necessary to know its stiffness. For a pair of gear teeth in mesh the reciprocal term, compliance is more convenient. The displacements are considered in the direction of the normal load, i.e. along the line of action.

#### 2.5.1 Weber's Semi-elasticity Solution [29]

The deflection of a tooth may be idealized to comprise of three discrete elements.

- a) The Hertzian deformation of the contact and of the underlying region.
- b) The bending and shear deformation of the tooth as a beam.
- c) The displacement at the load due to the deformation at the foundation of the tooth.

The Hertzian deflection is derived from theory of elasticity principles, using a stress function of complex variable. The elliptical load distribution given by Hertz is adopted (Fig. 2.14b).

$$p = p_{\max} [1 - (x'/b)^2]^{\frac{1}{2}} \quad (2.28)$$

where  $b$  is the half width of the contact strip between the contacting cylinders, as in Fig.(2.14a). If they are made of the same material:

$$b = \left[ \frac{8W}{\pi B} \frac{r_1 r_2}{r_1 + r_2} \frac{1 - \nu^2}{E} \right]^{\frac{1}{2}} \quad (2.29)$$

$r_1$  and  $r_2$  are the radii of the cylinders.

The length " $h$ " over which the deformation of the contact and the underlying region is considered, is delimited to the centerline of the tooth. The apex of the shear parabola in a rectangular beam is at the

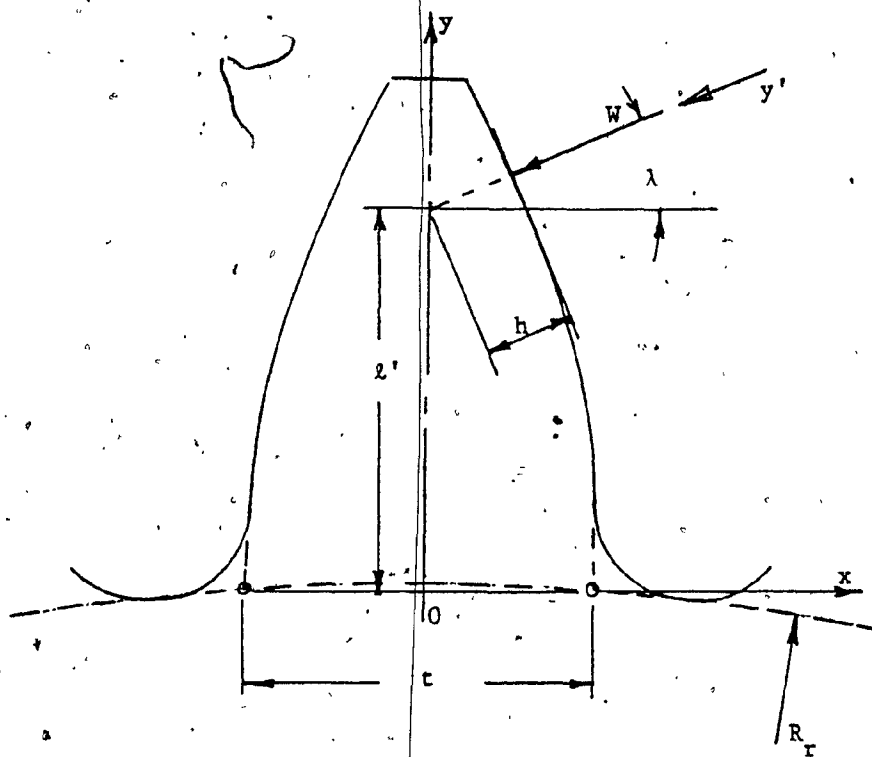


FIG. 2.13 COMPLIANCE LAYOUT - WEBER [29]

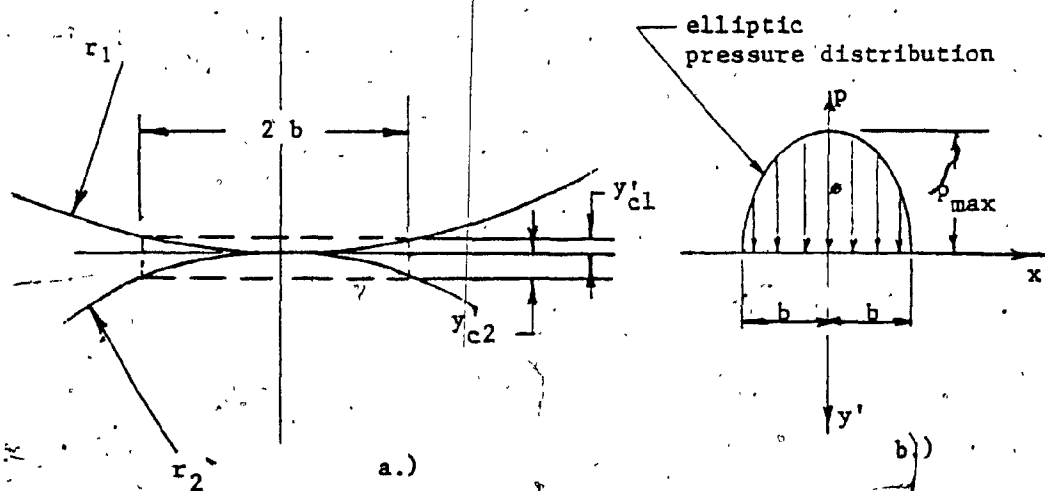


FIG. 2.14 CONTACT DEFORMATION AND PRESSURE DISTRIBUTION - WEBER [29]

centerline. Hence the main flow of the forces once they have reached the centerline of the tooth is transmitted through shear, which is accounted for in the "beam deflection" term. Therefore the Hertzian deflection for one tooth is:

$$y'_c = \frac{2W}{\pi B} \frac{1-v^2}{E} \left[ \ln \frac{2h}{b} - \frac{v}{1-v} \right] [\text{sic}]^1 \quad (2.30)$$

where  $h$  is the distance from the contact to the centerline of the tooth, (Fig. 2.13).

and for a mating pair made of the same material:

$$y'_{c1} + y'_{c2} = \frac{4W}{\pi B} \frac{1-v^2}{E} \left[ \ln \frac{2\sqrt{h_1 h_2}}{b} - \frac{v}{1-v} \right] [\text{sic}]^1 \quad (2.31)$$

The other two components of the deflection were found using energy methods. The strain energy in the tooth was equated with the work done by producing the displacement at the application of the load ( $\frac{1}{2} Wy'$ ). The beam deflection is given as:

$$y'_b = \frac{W}{EB} \cos^2 \lambda \left[ 12 \int_0^{l'} \frac{(l'-y)^2}{(2x)^3} dy + 3.1 \left( 1 + \frac{\tan^2 \lambda}{3.1} \right) \int_0^{l'} \frac{dy}{2x} \right] \quad (2.32)$$

where  $2x$ , the section width, is a function of  $y$ , as in Fig.(2.13)

The first term is due to the bending moment, the second, constant term is a factor for the shear, and the third term represents the effect of the radial component of the load.

<sup>1</sup>R.W. Corpell [8] found the last term to be  $\frac{v}{2(1-v)}$ . The writer could arrive only to the latter result.

The displacement at the load due to the deformation at the foundation of the tooth is:

$$y'_F = \frac{W}{EB} \cos^2 \lambda \left[ 5.2 \left( \frac{l'}{t} \right)^2 + \left( \frac{l'}{t} \right) + 1.4 \left( 1 + \frac{\tan^2 \lambda}{3.1} \right) \right] \quad (2.33)$$

The first term is due to the bending moment imparting root rotation. The second term combines the reciprocal affects of:

- a) the moment effecting root displacement,
- b) the shear force producing root rotation.

The constant in the last parenthesis represents the shear displacement and the last term is due to the radial component of the load.

Sample calculations are tabulated, and are compared with the experimental data of Walker [41] finding good agreement. The theory developed in this work is quoted repeatedly in the literature.

#### 2.5.2 W.J. O'Donnell: Stresses and deflections in Built in Beams [22]

This article focuses on displacements which are due to the rotation at the foundation of the beam under a bending moment. It is shown, that for short beams like a gear tooth, if this rotation is not accounted for, it leads to serious errors. It is equally true, and admitted by this author in the subsequent discussion, that for gear tooth foundation the "other" displacement elements dealt with by Weber [29] in Eq. (2.33) must also be included.

Nevertheless reasonable solutions were obtained expressed in a tabular hand book style. The nomenclature used is identical to that used by Roark [24] so that the insertion of a correction factor  $K_2$  permits ready application.

The rotation at the built in end:

$$\theta_m = \frac{16.67 M}{\pi E_s (t + 1.5 r_f)^2 B} \quad \begin{array}{l} \text{plane stress solution} \\ \text{for narrow beams} \end{array} \quad (2.34)$$

$$\theta_m = \frac{16.67 M (1 - \nu^2)}{\pi E_s (t + 1.5 r_f)^2 B} \quad \begin{array}{l} \text{plane strain solution} \\ \text{for wide beams} \end{array} \quad (2.35)$$

where  $E_s$  is Young's modulus for the support material.

The correction factor is given as:

$$K_2 = \theta_m EI \quad (2.36)$$

### 2.5.3 G. Chabert, T. Dang Tran, R. Mathis - Deflections, Using Finite Elements [7]

These authors used the finite element set up as described in paragraph 2.2.2 and Fig. (2.9) p 34.

At the outset the boundary of the structure was determined. The outer contour ABCDEF was fixed first, then the displacements along lines PQ and RS were computed. As it was found, that these displacements exceeded nowhere 3.5% of the deflection at the loading point M, it was concluded that the boundary may be safely reduced to PQRS, where zero displacements were imposed. The author's rationale for this step was to ascertain that a load on one tooth did not affect significantly the deflections on the next one. Consequently the flexibility coefficients were used directly to compute the sharing of the load for two pairs of teeth in contact.

Deflection values were generated for tip, pitchpoint and "Lowest Point for Single Tooth Contact" loadings. From the results "k" non-dimensional flexibility coefficients were computed, which were defined by the equation:



$$y = \frac{kW}{BE} \quad (2.37)$$

where  $y$  is the deflection

$W$  the normal load

$B$  the face width

$E$  is Young's modulus

The flexibility coefficients were then plotted vs load position and it was found, that they depend only on the geometry of the tooth and on the position of the load.

The sharing of the load was determined by considering the two teeth in contact as springs in series, the pairs as springs in parallel, as in Fig. (2.15a). Hence the two branch forces equal the total force:

$$W_1 + W_2 = W \quad (2.38)$$

The two branch deflections are the same.

$$(k_{1a} + k_{1b}) W_1 = (k_{2a} + k_{2b}) W_2 \quad (2.39)$$

The loads per unit face width were then plotted vs position on the line of action as in Fig. (2.15b).

It is clear that when all the load is carried by a single pair of teeth, it is the total normal force. However for double engagement the load variation on a single pair being "strictly linear" is questionable. Some additional evidence would be helpful to support such claim.

The process where the boundary was reduced must be examined more closely (Fig. 2.9) p.34. The proximity of the outer boundary ABC of zero displacements to line PQ has controlling influence on the displacements along that line. This very fact may invalidate the conclusion, which ruled out significant interaction between adjacent pairs.

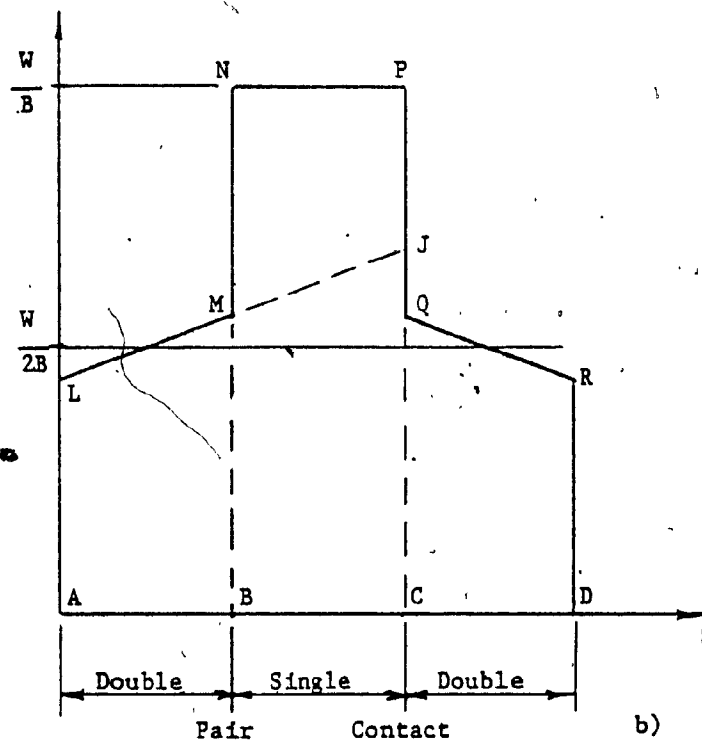
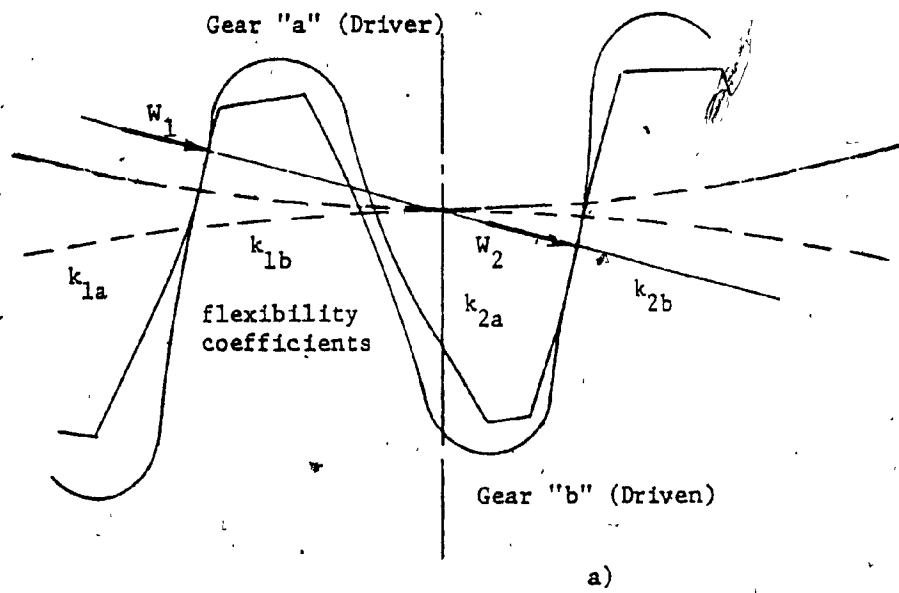


FIG. 2.15 LOAD SHARING - CHABERT ET AL [7]

2.5.4 A. Premilhat, G.V. Tordion, C.N. Baronet - Deflections,  
Using Complex Potentials [23]

The complex potential functions obtained by G.V. Tordion and C.N. Baronet [5] are used to find the deflections. Using plane strain analysis, the displacements of the median line of the tooth along  $x, y$  coordinates in the original  $z$  plane are obtained:

Due to the singularity at the point load, the deflection at the point of intersection between the tooth centerline and line of action is computed. To find the total deflection one may add the contact deformation as per Eq. (2.30) and footnote to the reported values.

The displacements of the tooth centerline are compared with Weber's [29] results graphically. They show similar trends, Weber's values being somewhat higher. The difference is likely to be reduced if the contact deformations are added to the deflections of the centerline.

2.5.5 R.W. Cornell's Expression for Pair Compliance [8]

The deflection of the tooth comprises of three components:

- a) The deflection of the tooth as a cantilever beam.
- b) The deflection at the load due to the deformations at the fillet and the foundation area.
- c) The local deformation at the contact and the underlying region delimited by the tooth centerline.

Computation of the beam deflection in general requires an integration. This operation is approximated by a summation process, which is based on elementary strength of materials principles. In this form the calculations can be readily performed on a programmable hand calculator. The layout and nomenclature are shown in Fig. (2.16).

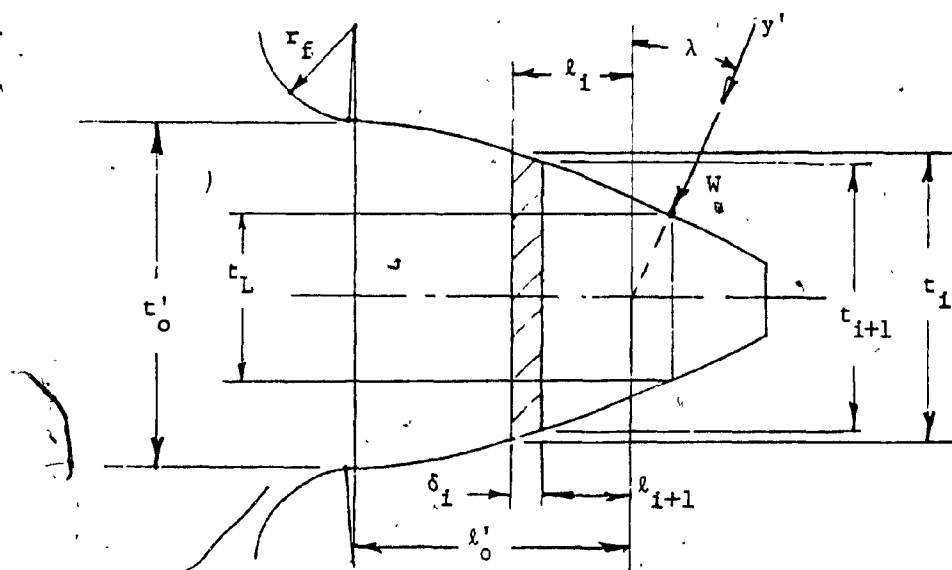


FIG. 2.16 BEAM COMPLIANCE - CORNELL [8]

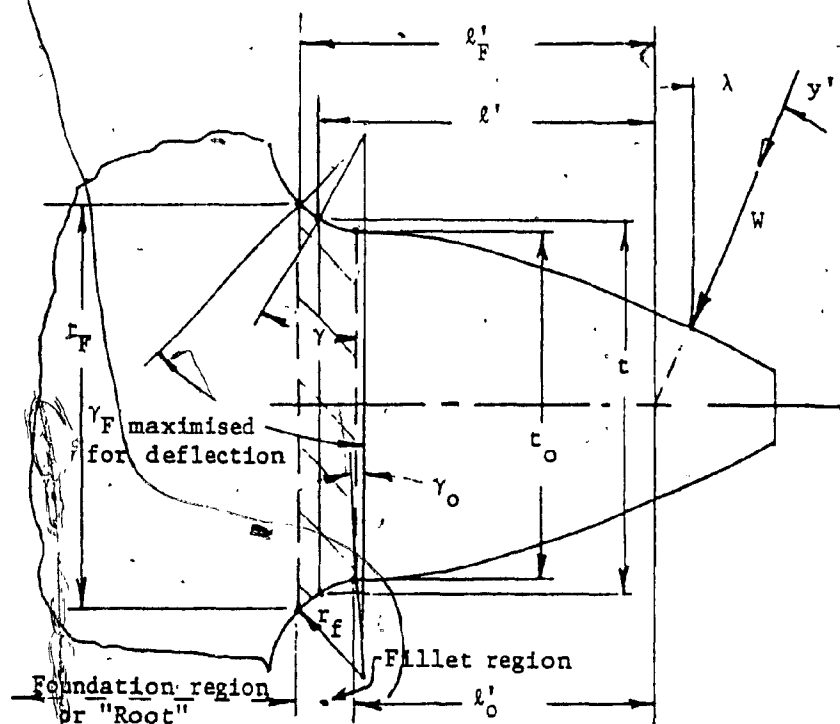


FIG. 2.17 FILLET AND FOUNDATION COMPLIANCE - CORNELL [8]

The deflection of the tooth as a beam:

$$y'_b = \frac{W \cos^2 \lambda}{BE} \sum_{i=1}^n \delta_i \left[ \frac{l_i^2 - l_i \delta_i + \delta_i^2 / 3}{\bar{I}_i} + \frac{[2.4(1+\nu) + \tan^2 \lambda]}{\bar{A}_i} \right] \quad (2.40)$$

$$\text{where } \frac{1}{\bar{I}_i} = \frac{1}{I_i} + \frac{1}{I_{i+1}} \quad \text{and} \quad \frac{1}{\bar{A}_i} = \frac{1}{A_i} + \frac{1}{A_{i+1}}$$

$I_i$  is the second area moment of the  $i_{th}$  segment.

$A_i$  is the cross sectional area of the  $i_{th}$  segment.

$d_i$  is the length of the that segment.

$l_i$  is the distance of the segment from the "critical section".

The expression above assumes narrow teeth i.e.  $B/t < 5$ . For wide teeth the values of  $I$  should be replaced by  $I/(1-\nu^2)$ .

For the deflections at the load due to the deformation at the foundation and fillet areas a modified version of O'Donnell's analysis [22] was adopted. The built in end is subdivided into two regions i.e. to foundation area or root and fillet area, see Fig. (2.17).

The deflection at the load due to deformations at the root is:

$$y'_{FF} = \frac{W \cos^2 \lambda}{BE} \left[ \frac{16.67}{\pi} \left( \frac{l_F}{t_F} \right)^2 + 2(1-\nu) \left( \frac{l_F}{t_F} \right) + 1.534 \left( 1 + \frac{\tan^2 \lambda}{2.4(1+\nu)} \right) \right]$$

plane stress solution for narrow teeth ( $B/T < 5$ ) (2.41)

$$y'_{FF} = \frac{W \cos^2 \lambda}{BE} (1-\nu^2) \left[ \frac{16.67}{\pi} \left( \frac{l_F}{t_F} \right)^2 + 2 \frac{1-\nu-2\nu^2}{1-\nu^2} \left( \frac{l_F}{t_F} \right) + 1.534 \left( 1 + \frac{\tan^2 \lambda}{2.4(1+\nu)} \right) \right]$$

plane strain solution for wide teeth ( $B/t > 5$ ) (2.42)

where the term	is due to the type of deformation at the root	caused by:
1st	rotation	moment
2nd	i) rotation <sup>1</sup>	shear
	ii) displacement <sup>1</sup>	moment
3rd	displacement	shear
4th	displacement	the radial component

$t_F$  is the beam depth, which is obtained by maximizing the deflections.

$2'_F$  is the distance from the load-centerline intersection to  $t_F$ .

The deflection of the fillet area  $y'_{FB}$  is calculated similarly as  $y'_B$  and the total deflection due to the flexibility of the foundation and the fillet area:

$$y'_F = y'_{FF} + y'_{FB} \quad (2.43)$$

For local deflection Weber's [29] equation is adopted. If the mating gears are made of the same material:

$$y'_C = \frac{4(1-\nu^2)}{\pi E} \frac{W}{B} \left[ \ln \frac{2\sqrt{h_1 h_2}}{b} - \frac{\nu}{2(1-\nu)} \right] \quad (2.44)$$

cf (2.31)

where  $h_1$  and  $h_2$  are the distances from the contact point to the respective centerlines of each tooth along the line of action.

$b$  is the half contact width (Fig. 2.18).

In the dynamic program [9] the compliance of a mating pair is considered. For this reason the deflection of the two members must be added, as they act in series connection.

<sup>1</sup> are equal terms as per Maxwell's reciprocity theorem.

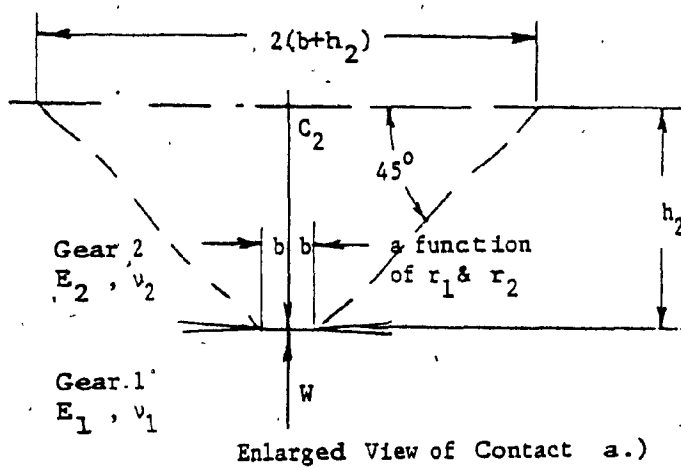
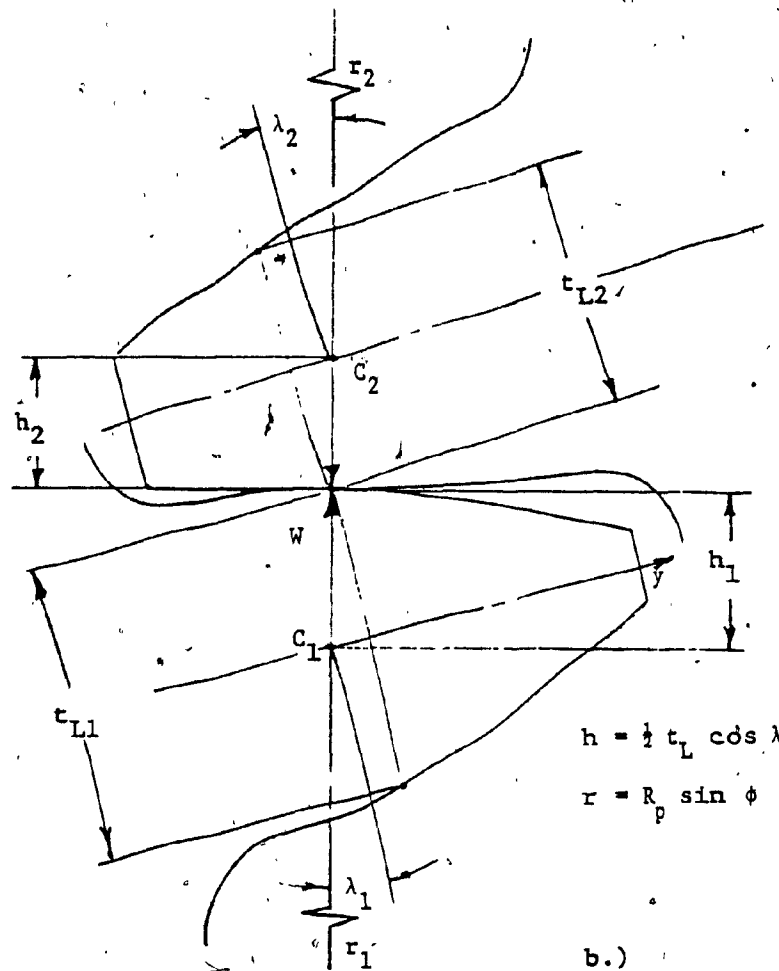


FIG. 2.18 LOCAL COMPLIANCE - CORNELL [8]

These lengthy expressions are calculated only for 5 loading positions. Using the 5 results curve fitting is applied and a 4th degree polynomial is generated, expressed in terms of a special normalized position along the line of action. The pair compliance equation:

$$C_p = C_{p0} \left[ 1 + A_1 \left( \frac{S}{S_0} \right) + B_1 \left( \frac{S}{S_0} \right)^2 + C_1 \left( \frac{S}{S_0} \right)^3 + D_1 \left( \frac{S}{S_0} \right)^4 \right] \quad (2.45)$$

where  $S_0$  is a reference distance along the line of action,  $S_{0e}$  for the approach and  $S_{0d}$  for the recess.

$S$  is the directed distance of the contact from the pitch point, positive toward disengagement.

$A_1, B_1, C_1, D_1$  are curve fitting coefficients.

$C_{p0}$  is the pair compliance at the pitch point.



## 2.6 Conclusions of Survey

The articles examined indicate a considerable development from the Lewis' formula to the application of complex potentials in the art of calculating fillet stresses. Consequently there is a wide variety of formulas available for this purpose.

The Heywood [18] and Kelley-Pedersen [20] expressions have overcome most of the early difficulties, and take into consideration the effects of stress concentration, radial component of load and the aspects of "proximity" at low dedendum loading.

The Coleman-Wilcox polynomial equation covers a wide variation of pressure angles, treats symmetric and asymmetric tooth forms. The Baronet-Tordion tables [5] are expected to give accurate "form factors" for the American standard tooth form. The Aida-Terauchi [2] formula retains the beam principle, accounts for all load components. The building block structure of the weighted stress components has a rational appeal.

It was indicated by Shotter [27] and others that the maximum tensile fillet stress, even if it was accurately known is not sufficient to predict fatigue failure. The stress distribution of the whole fillet, observed over a full load cycle, can only reveal the most dangerous stress range.

Relatively few articles were found dealing with the compliance of gear teeth. The basic analysis is due to Weber [29] complemented by O'Donnell [22]. The knowledge of this property is vital for dynamic analysis and for the determination of load sharing between simultaneously acting tooth pairs. The analysis applied by Chabert et

al [7] to the simple case of LCRG is not convincing. For evaluating HCRG this problem rises to primary importance.

A full treatment is given by Cornell and Westervelt [9][8]. It encompasses the determination of tooth proportions, compliance, dynamic loads and their sharing, and of the maximum tensile fillet stresses.

These theoretical developments are supported by experiments where only single teeth were loaded. Some hard core experimental evidence is lacking on the interaction of simultaneously acting tooth pairs.

Therefore it is deemed, that by conducting tests on a high contact ratio photoelastic model with multiple contact and rolling capabilities, our knowledge could be furthered concerning the following:

How is the total load shared?

How are the fillet stresses affected by the interaction of the branch loads acting at any point along the line of action?

To answer these questions the conventional photoelastic stress determination must be augmented by deflection measurements from which the compliances and the sharing of the load may be calculated. The experimental results would be supported by finite element analysis.

As a measure of the quality of the design a new concept the "Stress Admittance" will be introduced, which is expected to reveal the critical location of the load in multiple tooth engagement.

Such experiment may yield the range of stresses experienced by a given fillet point during a loading cycle. This information may be used later for fatigue analysis.

FORMULATION OF THE CONCEPT OF  
STRESS ADMITTANCE  
AND FATIGUE CONSIDERATIONS

The fillet stresses for HCRG are linear with respect to the load. Therefore the stress distribution for multiple tooth engagement may be obtained by superimposing the stresses generated by the individual loads. A single load induces primary stresses in the adjacent fillets. Secondary stresses appear on a substantial portion of the rim. Fillets, second and third in line act as stress risers in this diffused stress field. The cross effect of the loads results therefore in a complex stress distribution. The problem is further aggravated by the fact, that the individual loads are not known.

### 3.1 Stress Sensitivity

It was seen that the "primary" fillet stresses due to a single load may vary greatly with the shape of the tooth. However once a particular design is chosen, the stresses depend linearly on the magnitude of the load, and in a moderately nonlinear manner on the location, where it is applied. If this location is identified along the "line of action", a common parameter for the pinion and wheel is obtained. The stress response of a single tooth due to a unit load was referred to by Cornell [8] as the "Stress Sensitivity". It is a property of the shape of the tooth and is a function of the position of the load.

$$V = \frac{\sigma}{W} \quad (3.1)$$

where  $V$  is the stress sensitivity

$\sigma$  is the maximum fillet stress, tensile or compressive

$W$  is the normal load

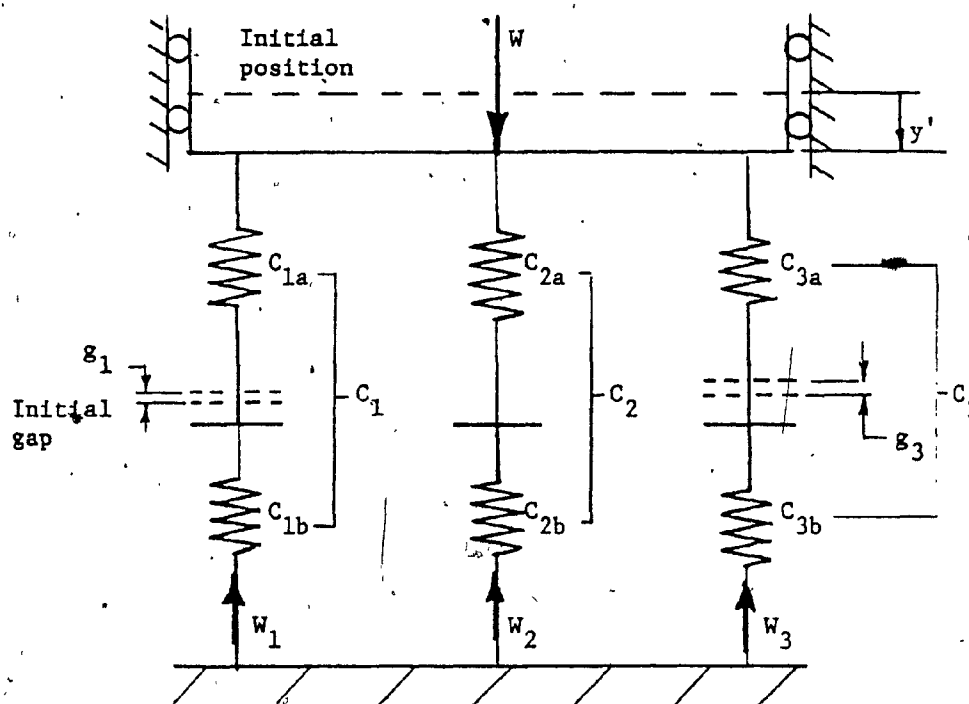


FIG. 3.1 STATIC MODEL FOR HIGH CONTACT RATIO TOOTH ENGAGEMENT

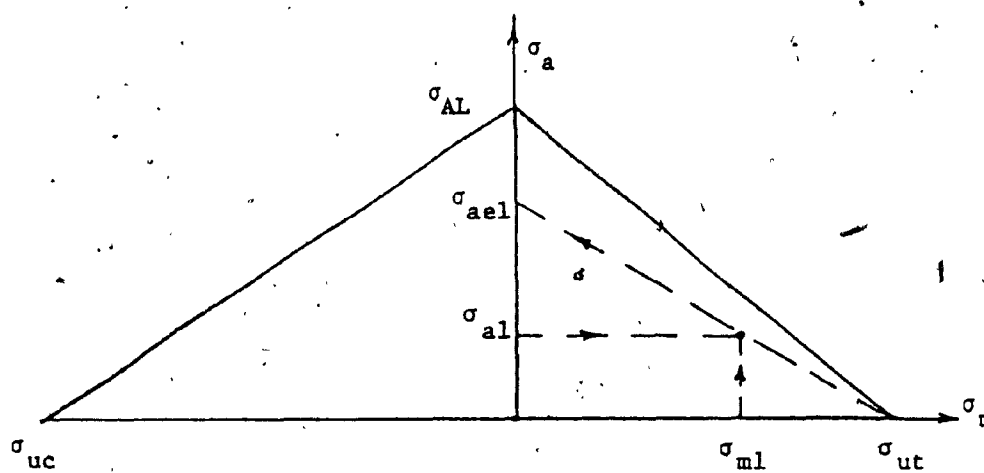


FIG. 3.2 FATIGUE DIAGRAM

### 3.2 Load Sharing in Multiple Pair Engagement

When a tooth acts in a group of simultaneously engaged pairs of three teeth, it may be modelled for static analysis as in Fig (3.1).

The total load branches out to three parallel paths using initially similar logic as in ref's [7] and [9]:

$$W = W_1 + W_2 + W_3 \quad (3.2)$$

A pair of springs connected in series represents a contacting pair of teeth. The parallel branches model the simultaneously acting pairs. Initial gaps are indicated for example in branches 1 and 3. These gaps eventually may be present due to manufacturing errors or profile modifications, which are introduced deliberately to minimize impact loading.

The total displacement is the same for each pair:

$$y'_1 = y'_2 = y'_3 = y' \quad (3.3)$$

The total displacement in branch 3 is typically the sum of the deflections of the teeth in that pair plus the size of the gap  $g_3$ , which must be closed before these teeth can deflect.

$$y'_3 = y'_{3a} + y'_{3b} + g_3 \quad (3.4)$$

The compliance in general:

$$C = \frac{y'}{W} \quad (3.5)$$

The compliance for pair 3, using Eq. (3.3)

$$C_3 = C_{3a} + C_{3b} = \frac{y'_{3a} + y'_{3b}}{W_3} = \frac{y' - g_3}{W_3}$$

giving the branch load:

$$W_3 = \frac{y' - g_3}{C_3} \quad \text{or} \quad W_1 = \frac{y' - g_1}{C_1} \quad (3.6)$$

The total load from Eq's. (3.2 and 3.6)

$$W = \sum_{i=1}^n \frac{y' - g_i}{C_i} \quad (3.7)$$

where  $n$  is the number of pairs simultaneously engaged

$g_i$  is the gap at the  $i^{\text{th}}$  pair. This gap is taken relative to the first contacting pair, hence here  $g_2 = 0$ .

Solving for the relative deflections between the two gear bodies:

$$y' = \left( W + \sum_{i=1}^n \frac{g_i}{C_i} \right) C_e \quad (3.8)$$

where  $C_e$  is the equivalent compliance of the  $n$  pairs connected in parallel i.e. the system compliance with the gear bodies considered to be rigid.

$$\frac{1}{C_e} = \sum_{i=1}^n \frac{1}{C_i} \quad (3.9)$$

If the gaps and compliances are known, and the compliances do not depend upon the load, the system deflection using Eq's. (3.8 and 3.9) may be calculated. Then the branch loads may be found from Eq. (3.6).

### 3.3 Stress Admittance

This new concept attempts to deduce the stress response of a tooth in a system from elementary properties.

The stress sensitivity of a tooth when acting as a member in a group may not indicate the most dangerous location for the load. If

applied at the tip it induces the most adverse stresses, but also causes the largest deflections. If the combined compliance of such tooth and its contacting mate is more than the same for the adjacent pair, the bulk of the load would seek out the other stiffer path, thus leaving a smaller load for that more sensitive location.

Therefore it is proposed that for a tooth acting in a group the ratio of its stress sensitivity over the combined compliance with its contacting mate to be considered for establishing the critical location for the load.

From Eq's. (3.1) and (3.6) the stress in tooth "3a":

$$\sigma_{3a} = W_3 V_{3a} = (y' - g_3) \frac{V_{3a}}{C_3} = (y' - g_3) Z_{3a} \quad (3.10)$$

Let Z be called "Stress Admittance" and be defined by the equation:

$$Z = \frac{V}{C_p} \quad (3.11)$$

where V is the stress due to a unit load (stress sensitivity)

$C_p$  is the compliance of the tooth in question plus the compliance of its mating pair. Or alternatively multiplying the numerator and the denominator by the load:

$$Z = \frac{\sigma_{\max}}{y' p} \quad (3.12)$$

where  $\sigma_{\max}$  is the maximum fillet stress, tensile or compressive

$y' p$  is the combined deflection of the tooth in question with its mating pair. Both parameters to be generated by the same load.

Z is a property of a subsystem, a pair of contacting teeth and is a function of the location of the load. At a given point it has four

values, each associated with one of the peak stresses in wheel and pinion, tensile and compressive.

### 3.4 Equivalent Static Alternating Stresses

Fatigue analysis is beyond the scope of this study. However some aspects of it are considered to demonstrate that the knowledge of the maximum tensile fillet stress may not be sufficient to evaluate the load carrying capacity of a gear tooth.

Each particular point on the fillet contour experiences a different range of stresses over a full load cycle. These ranges may be described by the mean of its extremes and the alternating amplitude about this mean. A comparable measure of the damage potential of these pairs of stress components may be obtained by using the Goodman relation:

$$\frac{\sigma_a}{\sigma_{ae}} + \frac{\sigma_m}{\sigma_{ut}} = 1 \quad (3.13)$$

where  $\sigma_a$  is the alternating component of stress

$\sigma_m$  is the mean stress

$\sigma_{ut}$  is the ultimate stress in a uniaxial tension test

$\sigma_{ae}$  is the equivalent alternating stress with zero mean having the same damage potential as  $\sigma_m$  and  $\sigma_a$  represent.

$\sigma_{AL}$  in Fig. (3.2) is the allowable maximum  $\sigma_{ae}$ . It may be set at 60% of the endurance limit of the material.

This method of evaluation was used by A. Elkholy [15], the diagram is shown in Fig. (3.2), p.59.



TEST EQUIPMENT4.1 The Prototype

The subject of this investigation is one of several proposed shapes for a pair of spur gears in the reduction gearbox of a newly developed turbo propeller engine. The tooth proportions were designed using a computer program which is in the development stage and is based on the articles of Cornell and Westervelt [8]. "High Contact Ratio" involute forms of modified addendums were employed.

The gears are proposed to be made of AMS 6265 carburized and hardened steel, having a Young's modulus of  $E = 207 \text{ GPa}$  (30,000 Ksi).

The gear data are given in Table 4.1. The tooth forms are shown in Fig's. (4.1) and (4.2). The various portions of the contour such as, true involute, modified tip, arcs of fillet and root circles are indicated.

4.2 The Model

A scale of 5X magnification was chosen for the models. It gives a high resolution of position and serves to attenuate the effect of manufacturing errors.

Five teeth were machined on each model, which were made of 6.35 mm (.25 in) thick, Photolastic PSM-1 clear polyester plates of 305 x 254 and 330 x 305 mm (12 x 10 and 13 x 12) inch sizes.

For sufficient diffusion of the applied forces the bodies of the models were reinforced by 9.5 mm (.38 in) thick polycarbonate plates cemented to both sides, see Fig. (4.8), p 81.

Table 4.1 Gear Data

	Pinion	Wheel
Tooth size	$m = 2.61 \text{ mm}$ $(P_D = 9.73 \text{ in}^{-1})$	
Nominal pressure angle	$17^\circ$	
Number of teeth	36	137
Pitch diameter	93.977 ( 3.6999 )	357.635 ( 14.0801 )
Outside diameter (mean)	102.21 ( 4.024 )	362.81 ( 14.284 )
Root diameter (mean)	87.56 ( 3.447 )	348.32 ( 13.713 )
"True Involute Form Diameter"	90.330 ( 3.556 )	351.559 ( 13.841 )
Root fillet radius	1.331 min (0.0524 min)	1.207 min (0.0475 min)
Circular arc tooth thickness (mean)	4.345 (0.1711)	3.570 (0.1406)
Tooth to tooth composite error	0.010 (0.0004)	
Center distance	225.806 ( 08.89 )	
Addendum	1.576 m	0.991 m
Dedendum	1.228 m	1.784 m
Contact ratio	2.327	
Face Width	76.2 ( 3.00 )	

Lengths are given in mm's, their inch equivalents are shown in parentheses,  $m$  is the module in mm's.

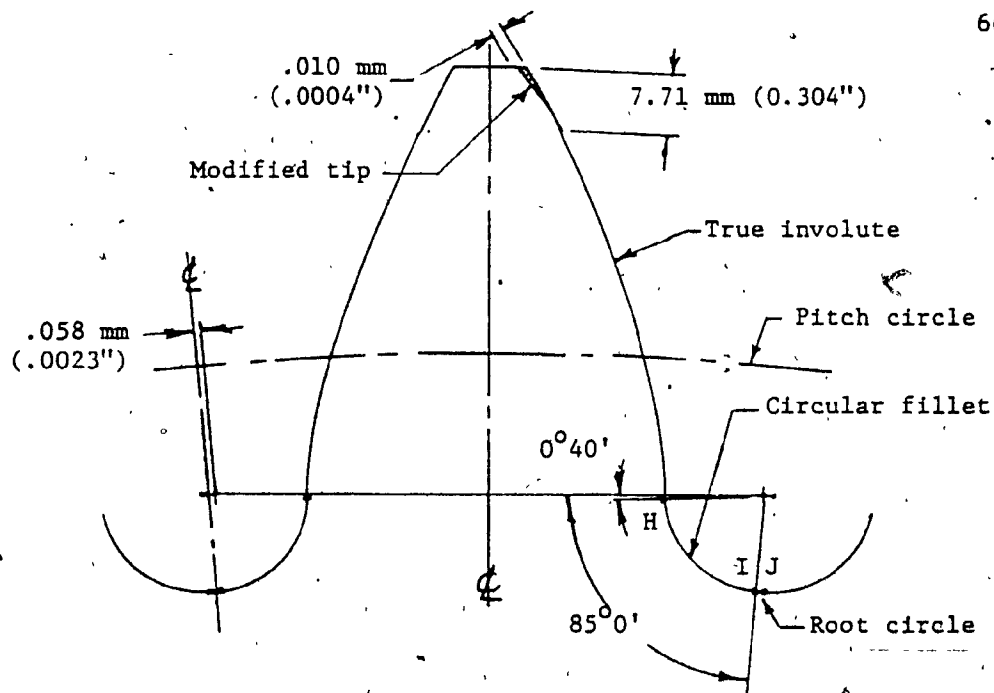


FIG. 4.1 TOOTH FORM - PINION

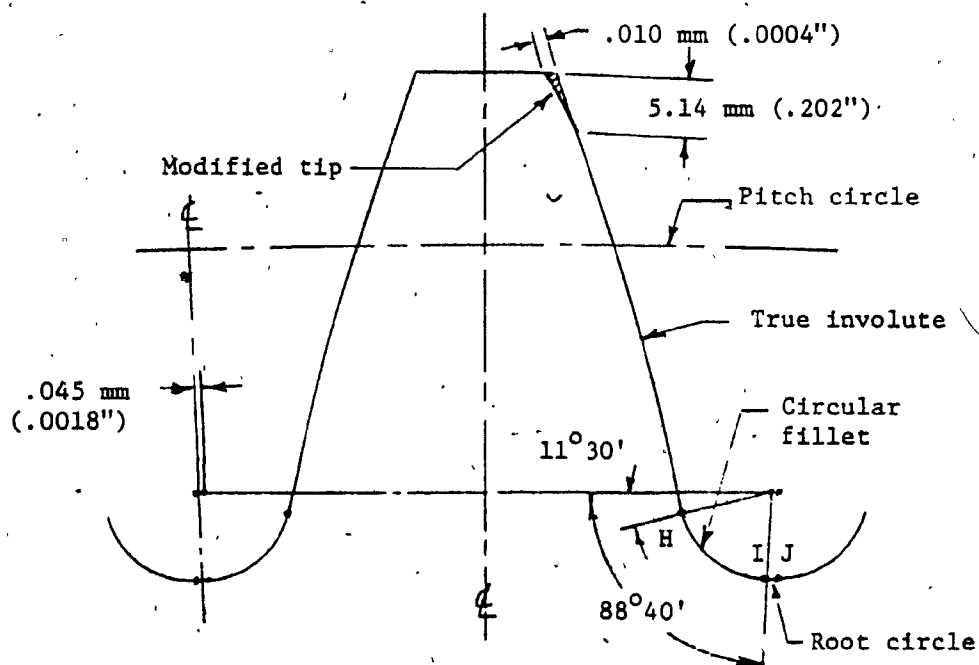


FIG. 4.2 TOOTH FORM - WHEEL

PSM-1 has a Young's modulus of 2.34 GPa (340 Ksi), Poisson's ratio .38, a nominal material fringe value of 7 KPa-m (40 psi-in). It is non-hygroscopic, therefore changes in humidity give no boundary stresses, i.e. little of the so called time edge effects.

#### 4.2.1 Computation of the Profile

The size of the model prohibited its machining by generation. The remaining methods known to the writer for fabricating the tooth profile required to calculate the coordinates of the contour. All these computations were performed on a Texas Instrument TI 59 programmable hand calculator.

##### 4.2.1.1 The Involute

The equations for the involute may be found in gear handbooks [6],[13]. For convenience they are repeated here in some detail.

The involute is often described as the path of a point on a cord, which is held taut, while it is unwound from a cylinder. In Fig. (4.3) the cylinder is the base circle of radius  $R_B$  of a gear. The cord is shown as line AE. Point A initially coincides with point B on the base circle. It passes the pitch circle at point P, ending its path on the gear at the outside diameter at point C.

Arc  $\widehat{BE}$  has the same length as side  $\overline{AE}$  in the right triangle AOE.

This key step gives the roll angle:

$$\epsilon = \frac{\widehat{BE}}{R_B} = \frac{\overline{AE}}{R_B} = \frac{(R^2 - R_B^2)^{\frac{1}{2}}}{R_B} = [(R/R_B)^2 - 1]^{\frac{1}{2}} = \tan \phi \quad (4.1)$$

The pressure angle may be obtained directly:

$$\phi = \cos^{-1} (R_B/R) \quad (4.2)$$

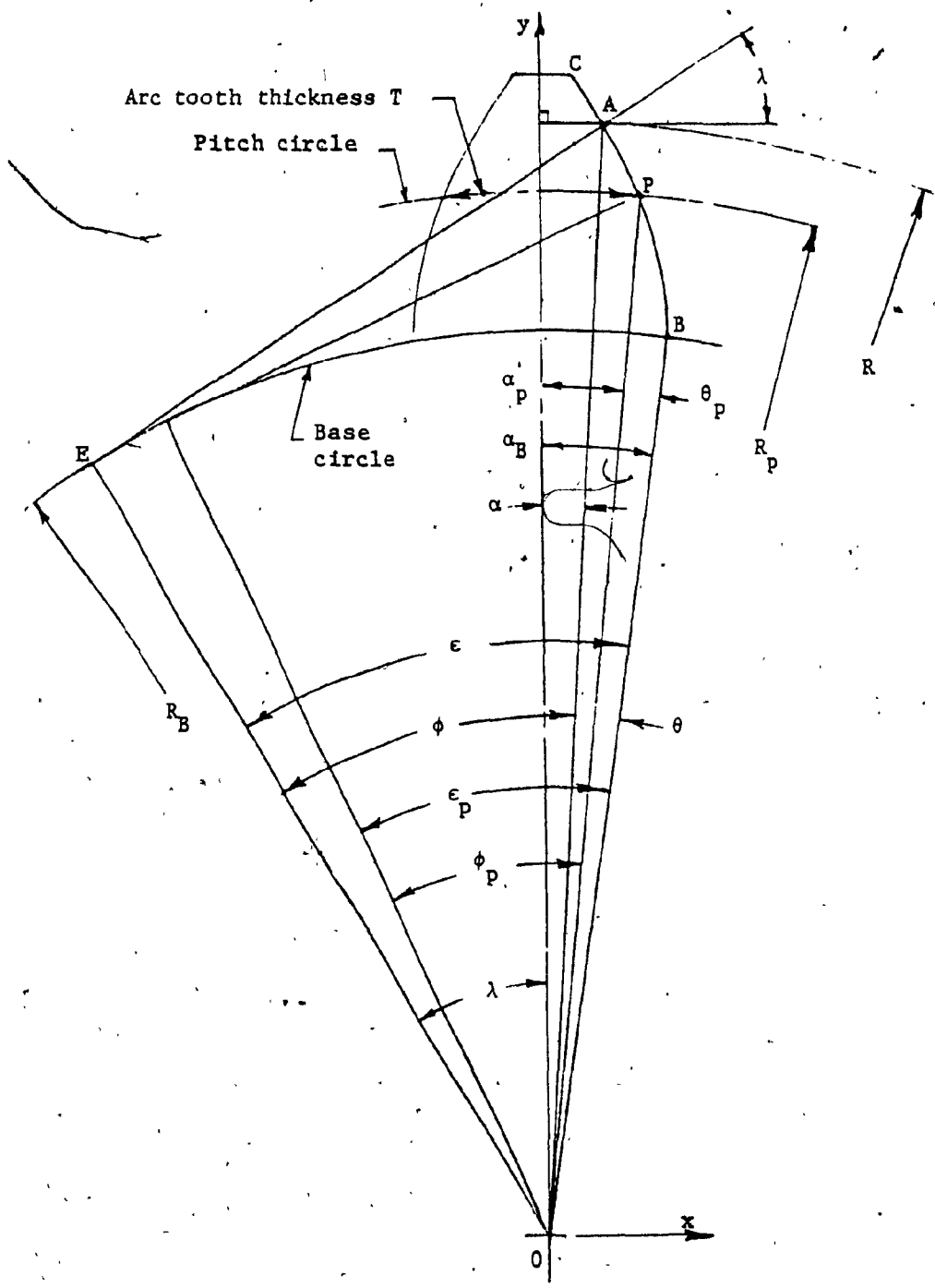


FIG. 4.3 INVOLUTE TOOTH PROFILE

The vectorial angle  $\theta$  is also known as the involute of  $\phi$ .

$$\theta = \epsilon - \phi = \tan \phi - \phi = \text{inv } \phi \quad (4.3)$$

In the design process the base radius  $R_B$  is usually obtained after the pitch radius  $R_p$  and the nominal pressure angle  $\phi_p$  has been chosen.

$$R_B = R_p \cos \phi_p \quad (4.4)$$

Arc tooth thickness  $T$  determines the position of the involute curve in relation to the centerline of the tooth. It is measured on the pitch circle, where the pressure angle is  $\phi_p$  by definition. The origin of the involute point B is at polar angle  $\alpha_B$  with respect to the centerline of the tooth. From Fig. (4.3):

$$\begin{aligned} \alpha_B &= \alpha_p + \theta_p \quad \text{or} \\ \alpha_B &= \frac{T}{2R_p} + \tan \phi_p - \phi_p \end{aligned} \quad (4.5)$$

The polar angle  $\alpha$  for a general point A:

$$\begin{aligned} \alpha &= \alpha_B - \theta \quad \text{or} \\ \alpha &= \frac{T}{2R_p} + \tan \phi_p - \phi_p - \phi + \tan \phi \end{aligned} \quad (4.6)$$

This is a polar equation for the involute curve as a tooth profile. The polar angle  $\alpha$  is implicitly the function of radial position  $R$  via Eq's. (4.1) or (4.2). The tie-in with the gear is through design parameters  $T$ ,  $R_p$  and  $\phi_p$ .

The normal to the involute with respect to the normal to the tooth centerline may be read off Fig. (4.3).

$$\lambda = \epsilon - \alpha_B \quad (4.7)$$

The Cartesian coordinates of a general point on the involute:

$$\begin{aligned} x &= R \cos \alpha \\ y &= R \sin \alpha \end{aligned} \quad (4.8)$$

#### 4.2.1.2 The Fillet

At the time of designing the model, the exact manufacturing process for the prototype was not known, hence the actual shape of the fillet curve was uncertain. As an approximation circular fillets were chosen for both models. The fillet curve was computed according to the geometry shown in Fig. (4.4).

The center of the fillet circle lies on an involute parallel to the original profile at a normal distance of  $r_f$  and at the same radial distance from the root circle.

$$r_C = \overline{OC} = R_r + r_f \quad \text{and} \quad (4.9)$$

$$\Delta \epsilon = \frac{r_f}{R_B} \quad (4.10)$$

The figure indicates that

$$\alpha_C = \alpha_B + \Delta \epsilon - \theta_C = \alpha_B + \phi_C - \epsilon_C + \Delta \epsilon \quad \text{or}$$

$$\alpha_C = \alpha_B + \cos^{-1} \frac{R_B}{R_r + r_f} - \left[ \left( \frac{R_r + r_f}{R_B} \right)^2 - 1 \right]^{\frac{1}{2}} + \frac{r_f}{R_B} \quad (4.11)$$

The center of the fillet circle is determined by

$$\begin{aligned} x_C &= (R_r + r_f) \sin \alpha_C \\ y_C &= (R_r + r_f) \cos \alpha_C \end{aligned} \quad (4.12)$$

The coordinates of a general point F on the fillet at an angle  $\gamma_F$  may be found from

$$\begin{aligned} x_F &= x_C - r_f \cos \gamma_F \\ y_F &= y_C - r_f \sin \gamma_F \end{aligned} \quad (4.13)$$





The fillet radii on the model were increased by approximately 5% over the specified minimum. This represents 1/4 of the possible increase of fillet radius for the pinion, without violating the "True Involute Form Dia" limit. The choice of this amount was arbitrary, the change itself concurs with the findings of Kelley and Pedersen [20]. The radius of curvature of the trochoid, which is the actual shape of the fillet produced by a rack type tool, is substantially larger at the region of the peak stresses, than it is adjacent to the root circle, where its minimum value is located. A moderately oversized radius is thus a more representative substitution.

#### 4.2.1.3 Tip Relief

As the gear tooth is an elastic structure it deflects under the load. Consequently a loaded tooth lags behind in motion in relation to an unloaded tooth next in line. This tooth would then engage in a non conjugate contact with an impact, the sharp edge of the tip scoring the mating face, causing early failure. Manufacturing errors in the tooth form aggravate the problem. Removing some material from the tip to smoothen the initial contact is the usual remedy.

The amount of tip relief may be calculated from the deflection of the tooth to which the composite error is added. If the transmitted torque varies widely, a tip relief corresponding to the maximum loading may cause impact at lower torque values.

At such condition the deflection of the loaded pair does not fill the gap created by the tip modification. As the contacting pair disengages, the next pair has to jump the gap.

A compromise must be made, the designer should be guided by good judgement. The relief has its maximum at the tip, then gradually decreases until it blends at a certain point into the involute. Suggested optimum values are given in two empirical formulas in D.W. Dudley's Gear Handbook [13], Chapter 5, p. 23

The maximum modification at the engagement side:

$$m_{tmax}[\text{mm}] = 5.08 \times 10^{-5} \frac{W_t[\text{N}]}{B[\text{mm}]} \quad (4.14)$$

where material is removed from the tip of the driven gear. The same at the disengagement side:

$$m_{tmax}[\text{mm}] = 2.90 \times 10^{-5} \frac{W_t[\text{N}]}{B[\text{mm}]} \quad (4.15)$$

where material is removed from the tip of the driver gear.

These formulas gave  $m_{max}$  of .0127 mm (.0005") for the driven wheel, and .0072 mm (.0003") for the pinion. The designer of this drive adopted .0102 mm (.0004") for both gears, which was then incorporated into the photoelastic model.

The departure from the involute may take a parabolically increasing form. Such scheme is given by R.W. Cornell and W.W. Westervelt [9]. The modification is given in terms of the position of the contact along the line of action "S":

$$m_t = m_{tmax} \left( \frac{S - S_e}{S_{oe} - S_e} \right)^2 \quad \text{and} \quad (4.16)$$

$$m_t = m_{tmax} \left( \frac{S - S_e}{S_{od} - S_d} \right)^2$$

on the engagement and disengagement sides respectively, where

$S_{oe}$  and  $S_{od}$  are the end points on the line of action.

$S_e$  and  $S_d$  are the respective values where the tip relief starts with zero.

At LCRG usually the "Highest Point for Single Tooth Contact" is chosen for starting the relief curve. For HCRG an analogous "Highest Point for Double Tooth Contact" may be adopted as the initial point of tip modification. Replacing  $P_B$  in Eq. (2.8) by  $2P_B$  and using Eq. (2.9) the respective  $R_H$ 's and their corresponding positions on the line of action were computed, obtaining:

$R_H = 180.4 \text{ mm (7.102")}$  and  $S_e = 5.14 \text{ mm (0.202")}$  for the wheel.

$R'_H = 49.8 \text{ mm (1.960")}$  and  $S_d = 7.71 \text{ mm (0.304")}$  for the pinion.

For the inspection of the profile it was necessary to determine the inclination of the normal to the contour at the check points. This angle for the true involute using Eq. (4.7) and Fig. (4.5)

$$\lambda_A = \epsilon_A - \alpha_B$$

At the modified profile this normal rotates with the rate of change of modification with respect to radial position.

$$\lambda_M = \lambda_A + \frac{dm_t}{dR} \quad (4.17)$$

$dm_t/dR$  may be obtained from Eq. (4.16) and from

$$S = R_p \sin \phi_p - (R^2 - R_B^2)^{1/2} \quad \begin{array}{l} \text{Eq. (5.4), p 92} \\ \text{see also Fig. (5.1), p 86} \end{array}$$

$$\begin{aligned} \frac{dm_t}{dR} &= \frac{dm_t}{dS} \frac{dS}{dR} = 2 m_{tmax} \frac{S - S_e}{S_{oe} - S_e} \frac{-R}{(R^2 - R_B^2)^{1/2}} \\ &= \frac{-2 m_{tmax}}{\sin \phi} \frac{S - S_e}{S_{oe} - S_e} \end{aligned} \quad (4.18)$$

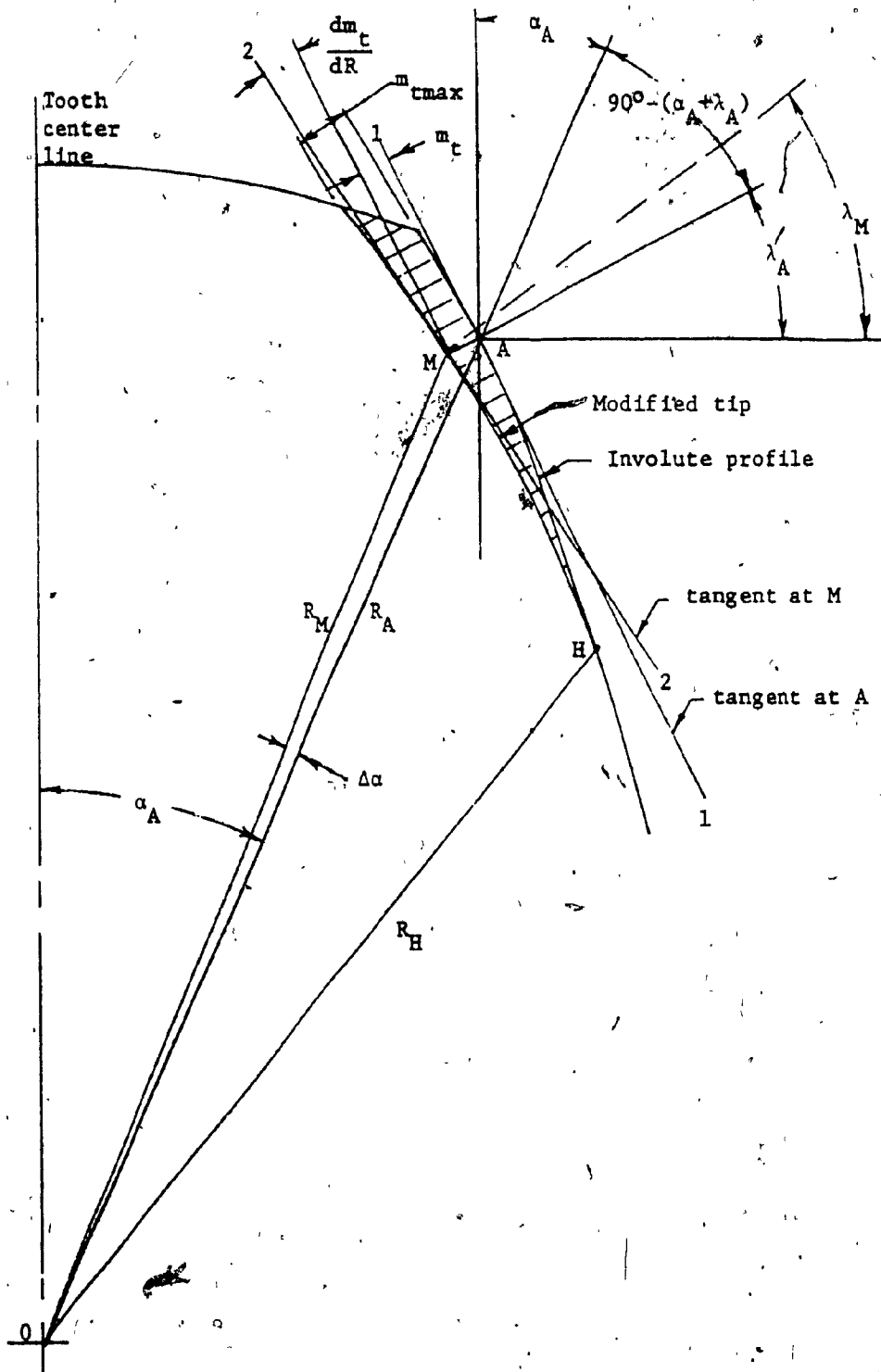


FIG. 4.5 TIP MODIFICATION

where  $\phi$  corresponds to radius  $R$  at point  $A$ .

From Fig. (4.5) it may be seen that  $\angle MAO = 90^\circ - (\alpha_A + \lambda_A)$ .

Triangle  $MAO$  lends itself to find the polar coordinates for point  $M$ .

$$R_M = [R_A^2 + m_t^2 - 2R_A m_t \sin(\alpha_A + \lambda_A)]^{\frac{1}{2}} \quad (4.19)$$

$$\Delta\alpha = \sin^{-1} \frac{m_t}{R_M} \cos(\alpha_A + \lambda_A) \quad (4.20)$$

#### 4.2.2 Making the Models

The coordinates of the profile were used as input for numerically controlled machines (NC). These systems accept discrete points as raw data, the "best fit" curves are internally generated for servo control.

50X (prototype) comparator charts of one tooth with 2 spaces were drawn on mylar using an "Interactive Graphic System". The templates for the models were contoured on an NC Onsrud milling machine.

Unfortunately the latter produced a wavy surface. The templates had to be finished by hand, using the comparator charts as a guide.

The contours were transferred from the templates to the models on a Photolastic HSR-1 router. The two lip router bit works under water, thus significant residual stresses are avoided.

It was soon apparent, that the HCRG system is more sensitive to machining errors, than the conventional LCR gearing. The accuracy so far achieved, produced an unlikely photoelastic picture. It was realized, that if any useful conclusions are to be drawn from a multiple contact test, the precision of the model should be one order higher than that of the prototype. The 5X enlargement is helpful, but adequate

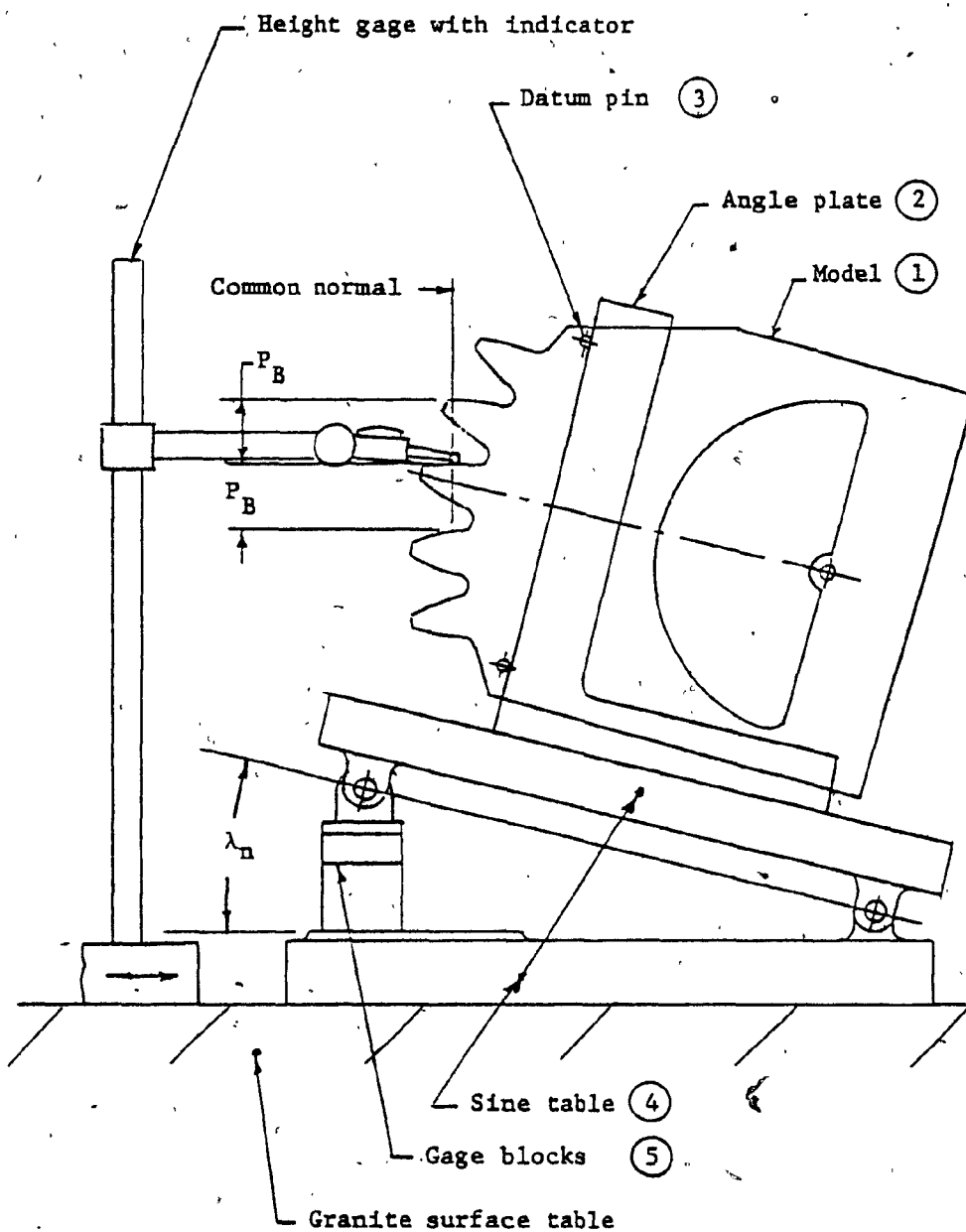
methods for machining and for inspection were yet to be found.

The solution to the problem of inspection came first. A coordinate inspection machine DEA-Gamma was chosen. As the probe of this machine approaches the target the computer registers the position of the probe at the instant of contact. It was claimed, that this machine operates with a repeatability of .005 mm (.0002").

The method which was devised for the adjustment of the profile may be explained with the help of Fig.(4.6). The model (1) is clamped to the angle plate (2) with datum pins (3) held firmly against the side surface of the plate. The assembly is then mounted on the sine table (4). The gage blocks (5) tilt the model to a desired angle with high accuracy. Therefore if the direction of the normal to the profile at a selected point is known this normal can be set exactly vertical. Consequently an abrasive tool with its motion restricted to a horizontal plane may touch the model precisely at that point, see Fig. (4.7).

The preloaded ball slide (1) gave a backlash free linear motion. It was mounted on a cross slide (2), giving vertical adjustment by the means of its lead screw (3). The assembly was bolted to an angleplate (4) so that the top surface of the ball slide could be set horizontal within .005 mm (.0002)". A wedge nosed square tool bit (5) with protruding front was attached to the top of the ball slide. A fine (400 grit) emery paper (6) mounted on the nose with face down gave the abrasive surface.

With some care this set up made it possible to remove as little as .003 mm (.0001"), square to the plane of the model from any convex region of the profile. The contours of the rolling surfaces were



Note: Clamps are not shown.

FIG. 4.6: PROFILE ADJUSTMENT SET-UP, MOUNTING OF THE MODEL

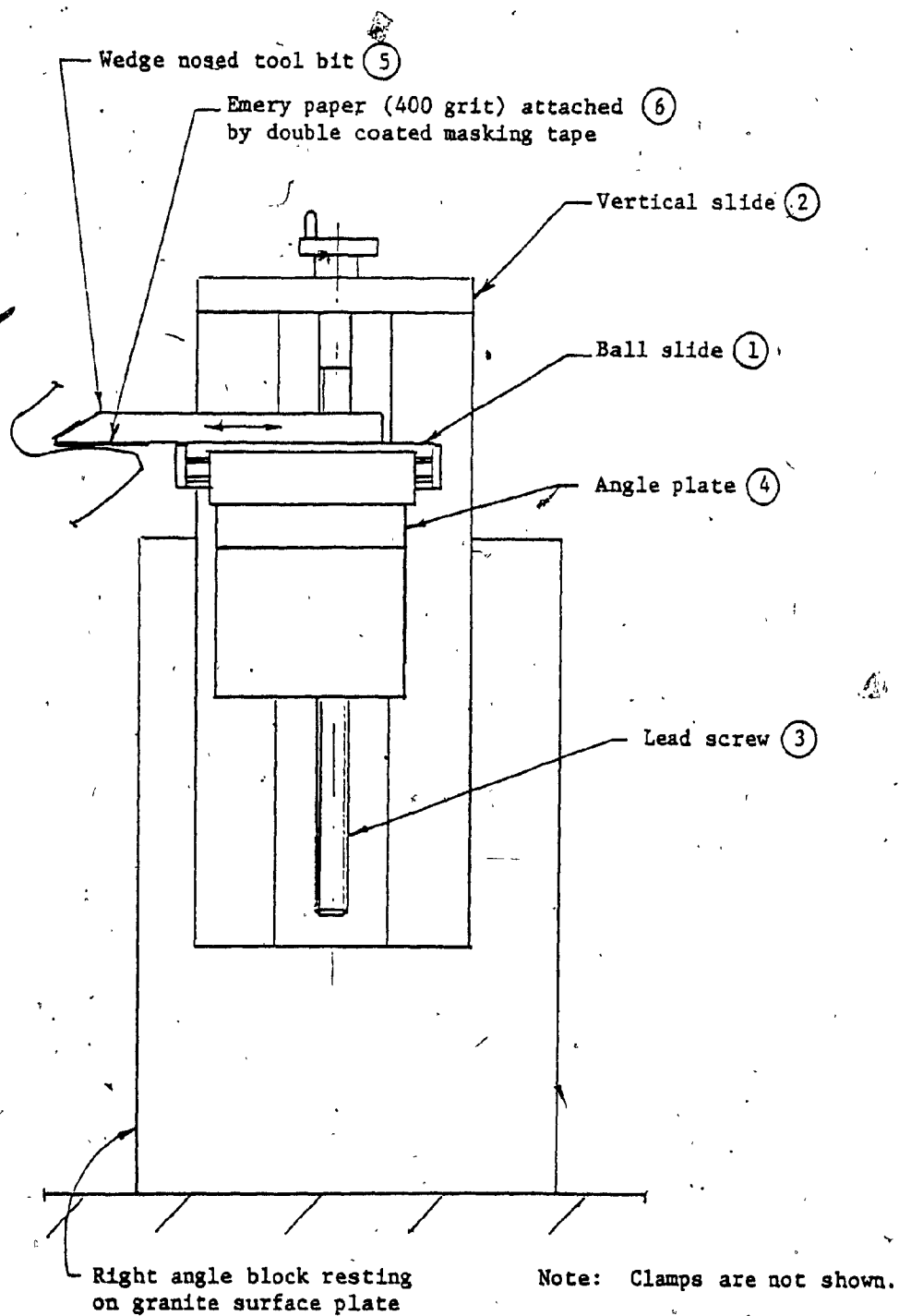


FIG. 4.7 PROFILE ADJUSTMENT SET-UP, GUIDE FOR ABRASIVE TOOL



corrected point by point in several passes.

The true involute was eventually approximated within .013 mm (.0005"). The overall repeatability which was affected also by other conditions such as the flatness of the plastic, the accuracy of the datum holes etc. inhibited further improvement.

The most relevant error, which affects the sharing of the load between pairs of teeth is the deviation between their respective distances along the line of action i.e., the relative base pitch error, see Fig. (4.6). These distances may be measured directly on the tilted set up described above.

As a final step for refinement of the profile the base pitches for points in simultaneous contact for the planned loading positions were tuned within .008 mm (.0003").

When the models were installed into the rig the maximum gap in the involute region was found to be .01 mm (.0004").

#### 4.3 The Rig

The experimental setup is shown in Fig's. (4.8) and (4.9). The models must be mounted on their respective centers to permit genuine rolling. This would require an excessive size of photoelastic material to make a one piece wheel. A commercially available size of plastic was chosen and it was consequently augmented by an aluminum plate, the arm (1), which was joined to the plastic model at the polycarbonate side plates (2) using press fit aluminum bushings (3).

Deadweight loading pulls the arm upward by means of a 1.2 mm (3/64") dia flexible, stainless steel cable (4), passing over two pulleys (5),(6) equipped with ball bearings. Space between the side

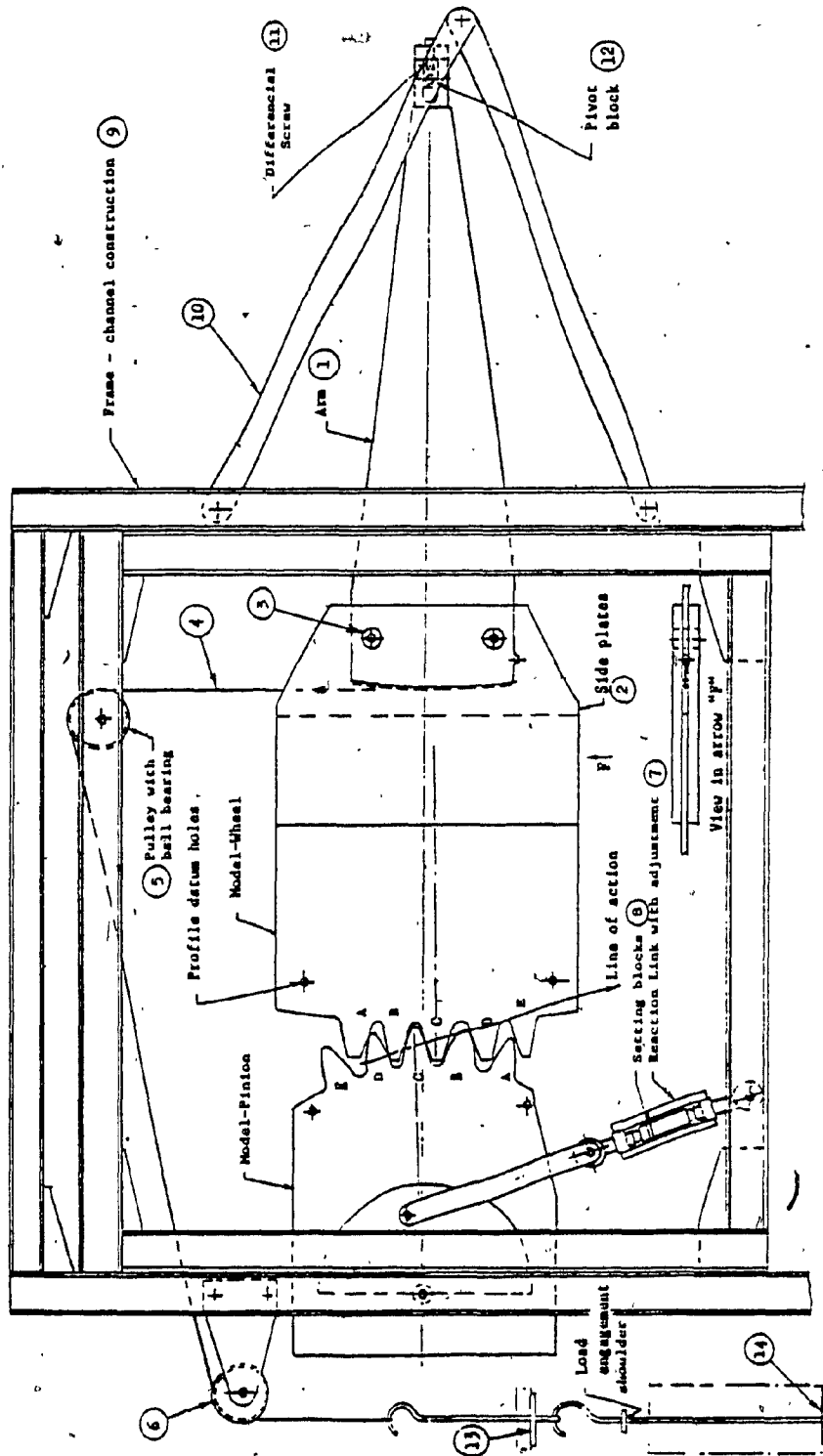


FIG. 4.8 EXPERIMENTAL SET-UP FRONTAL VIEW

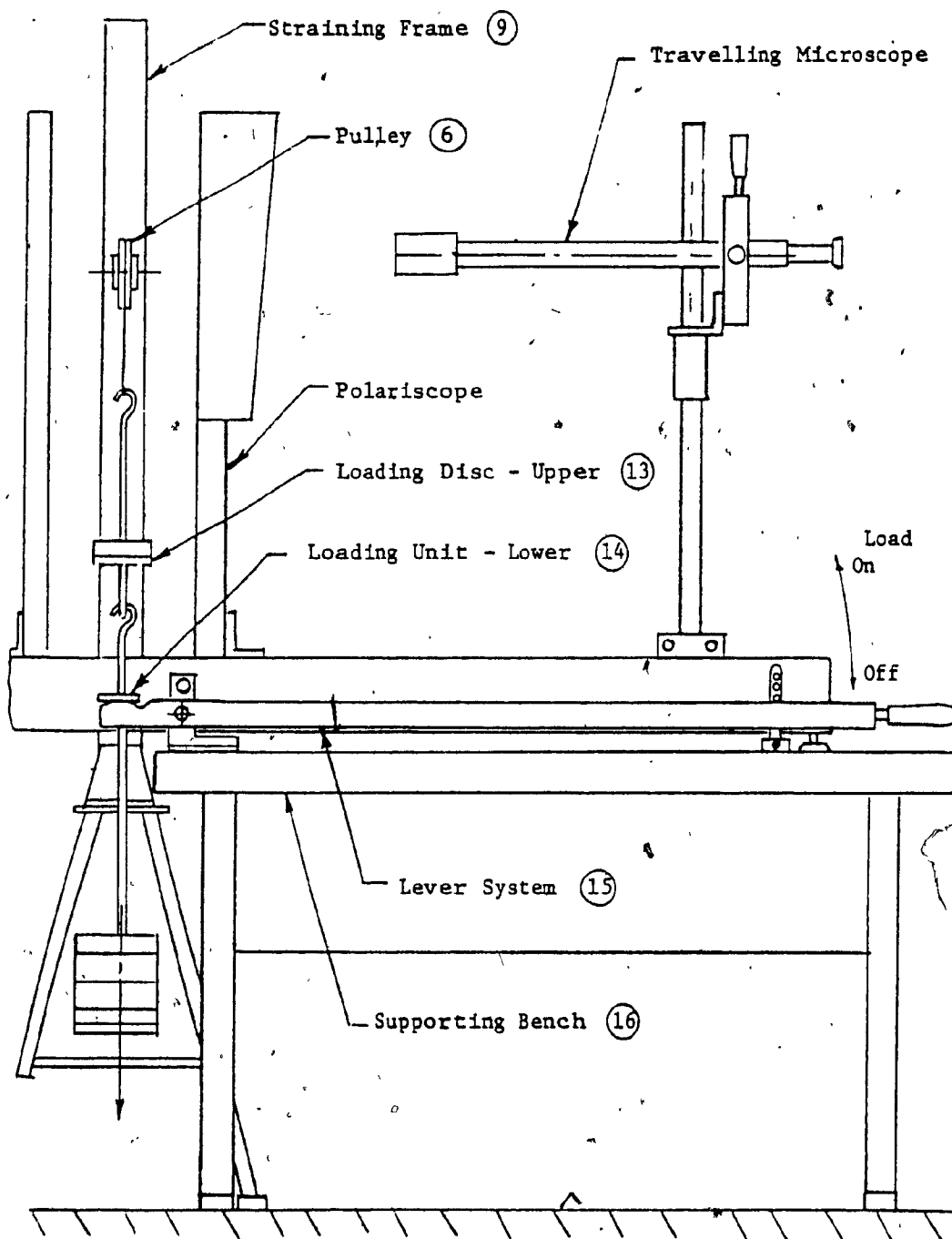


FIG. 4.9 EXPERIMENTAL SET-UP - SIDE-VIEW

plates yields access to the bottom side of the arm, to which the cable is attached. The circular arc on the front end of this arm is furnished with a V-groove in which the cable is seated. This arrangement ensures consistency in torque with respect to rolling and delivers the load to the vertical centerplane of the model.

The rotation of the pinion is restrained by the reaction link (7). Its length is adjustable, hence the points of contact may be moved along the line of action. This device is essentially a turnbuckle, made to accept hardened setting blocks (8), ensuring a repeatability of setting within .025 mm (.001 in.).

The weight of the reaction link is balanced by deadweights via a second cable and a lever (not shown).

The center distance for the models exceeded the width of the straining frame (9). An outboard truss (10) was added to the structure to support the center of the wheel. Fine adjustment of the center distance is accomplished by a differential screw (11), which shifts the pivot hole block (12) within the arm.

The deadweights are seated on two discs hooked in tandem. The upper disc (13) carries a small load just to maintain a positive contact. The main load is applied to the lower loading unit (14). Rapid and smooth loading or unloading is achieved by a lever system (15), which could engage or disengage the lower loading unit, see the side view Fig. (4.9). This device is bolted to the supporting bench (16) of the polariscope and is operated from the viewing seat (not shown). The experimental set up is also shown on photograph Fig. (4.10).

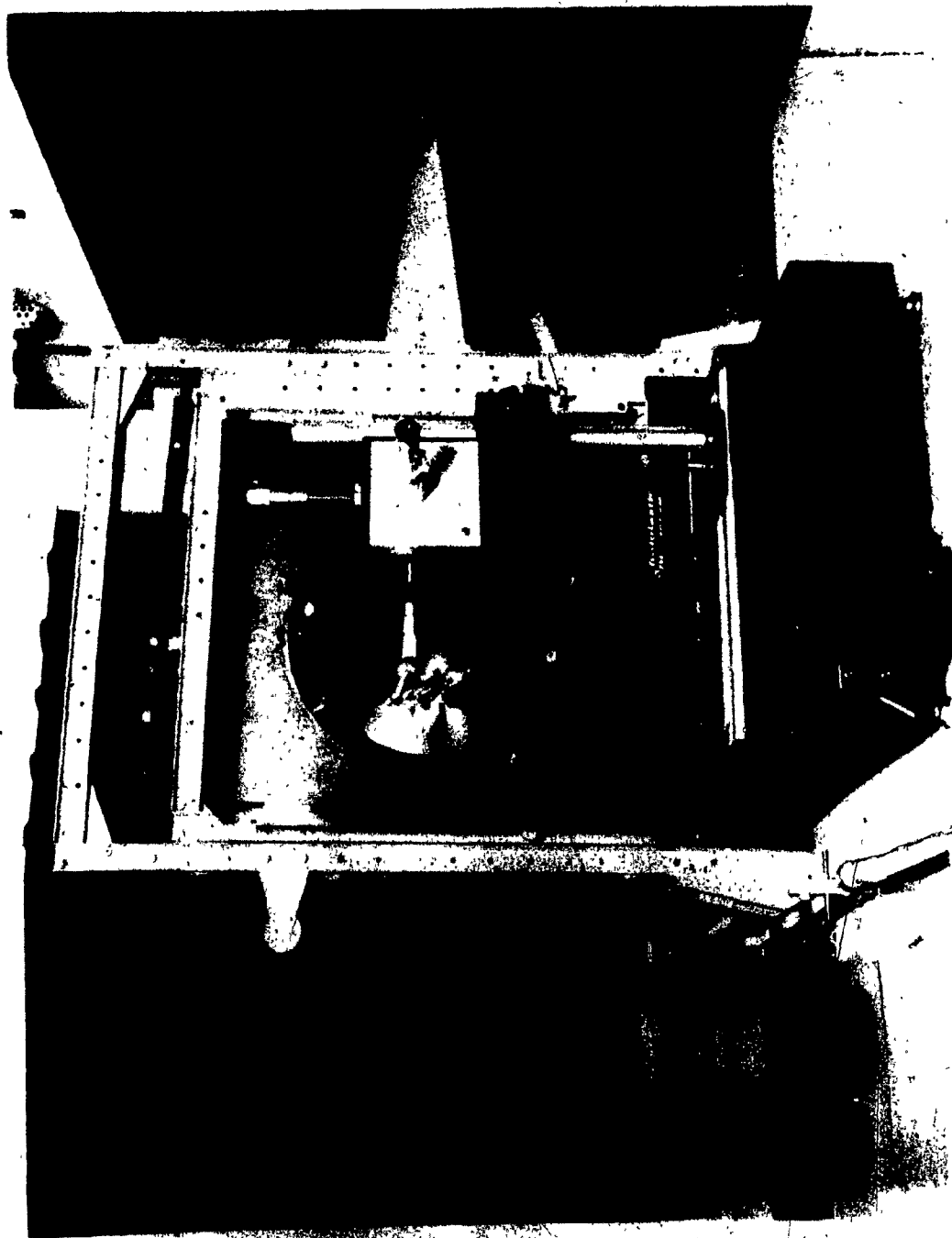


FIG. 4.10 POLARISCOPE AND STRAINING RIG

TEST PROCEDURE5.1 Geometric Considerations

For proper correlation of data and for the planning of the test it is necessary to know in advance:

- a.) The point on the pinion that will be in contact with a given point on the wheel.
- b.) The points which are simultaneously in contact.

5.1.1 Theoretical Match-Points of Pinion and Wheel

These points may be found using Fig.(5.1). The center distance:

$$C = R'_p + R_p \quad (5.1)$$

where the prime refers to the pinion, the unprimed symbol to the wheel.

The angular position of the contact:

$$\psi = \phi_p - \phi = \phi_p - \cos^{-1} \frac{R_B}{R} \quad (5.2)$$

The radius on the rolling surface of the pinion, which matches the point at R on the wheel

$$R' = (R^2 + C^2 - 2RC \cos \psi)^{1/2} \quad (5.3)$$

The position of the contact on the line of action:

$$S = R_p \sin \phi - (R^2 - R_B^2)^{1/2} \quad (5.4)$$

5.1.2 Points of Simultaneous Contact

The points which are in contact at the same time may be determined from Fig. (5.2).

The distance between two contacting points is the base pitch  $P_B$  which may be obtained from:

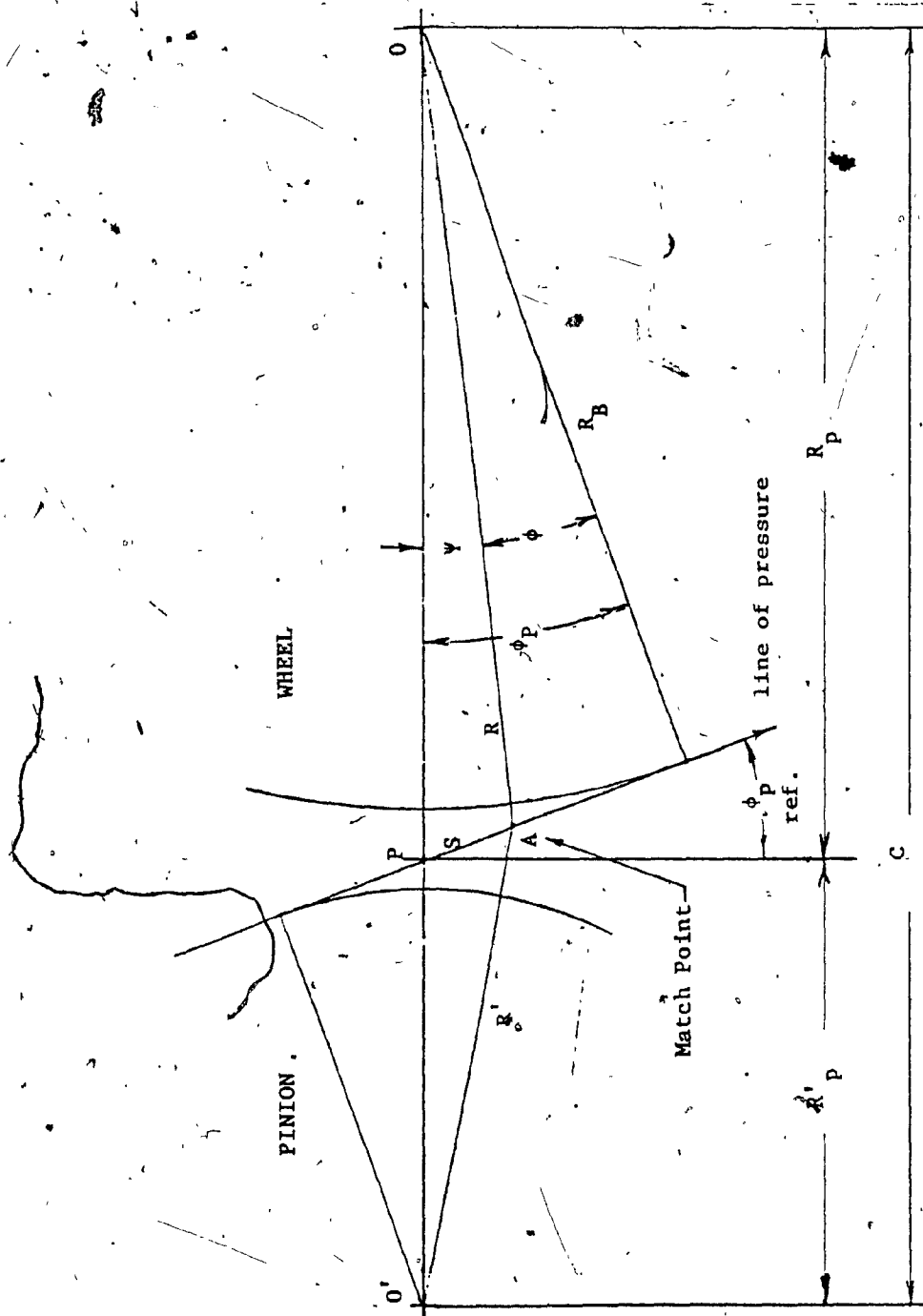


FIG. 5.1 MATCHING RADII.

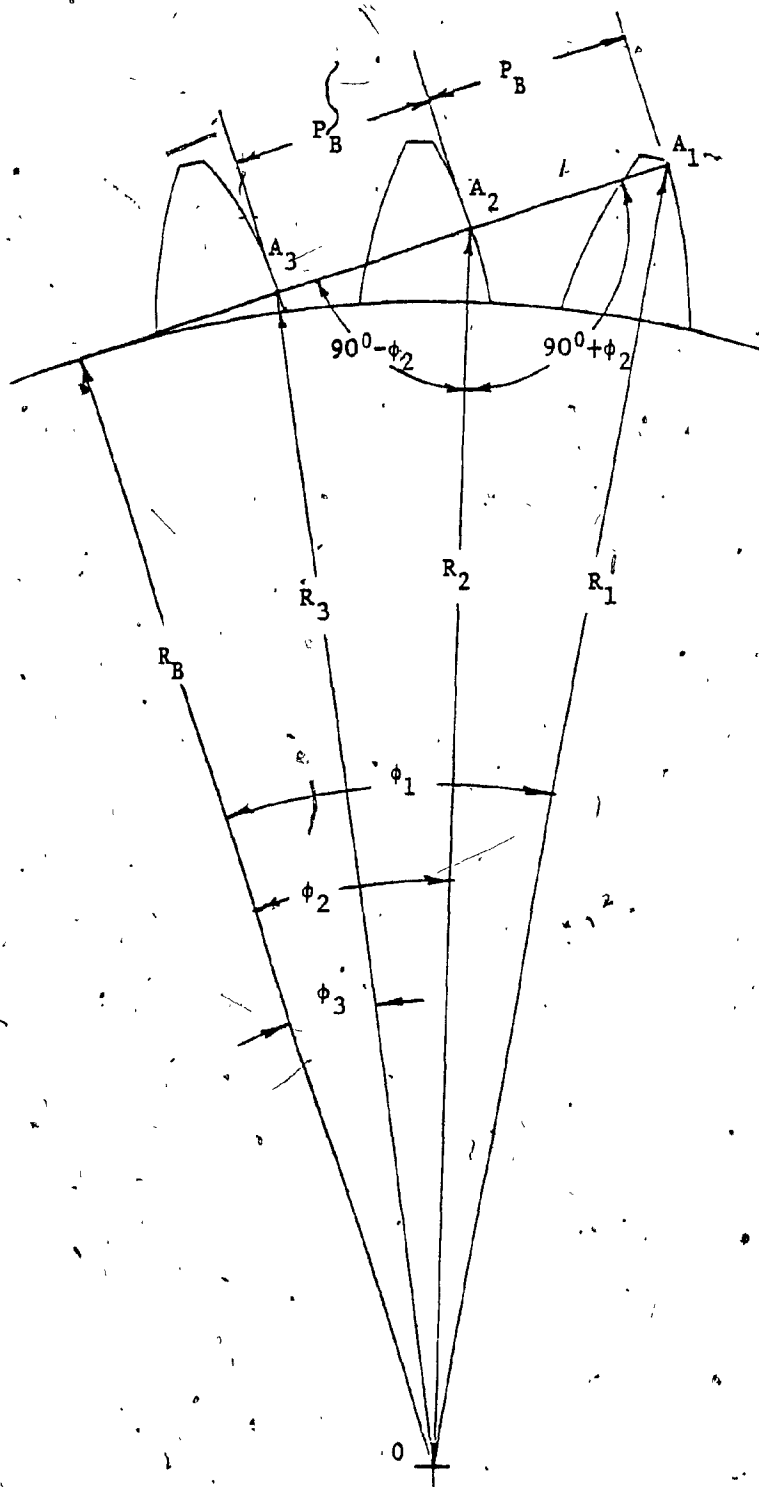


FIG. 5.2: POINTS OF SIMULTANEOUS CONTACT



$$P_B = \frac{2\pi}{N} R_B \quad (5.5)$$

where  $N$  is the number of teeth. Using the nomenclature as shown:

$$\cos(90^\circ + \phi_2) = -\sin \phi_2 \quad (5.6)$$

$$\cos(90^\circ - \phi_2) = \sin \phi_2 \quad (5.7)$$

If the radius of the contact in the tooth on the middle is known ( $R_2$ ), the contact on the higher radius will be at:

$$R_1 = [R_2^2 + P_B^2 + 2R_2P_B \sin \phi_2]^{\frac{1}{2}} \quad (5.8)$$

and the one on the lower radius at:

$$R_3 = [R_2^2 + P_B^2 - 2R_2P_B \sin \phi_2]^{\frac{1}{2}} \quad (5.9)$$

## 5.2 Scaling

As the geometric proportions and material properties of the model are different from those for the prototype, their load, stress and deflection relationships must be established.

Their similarity to remain valid, the distribution of the stresses must be independent of Poisson's ratio [10],[14].

For plane stress analysis of a simply connected structure in a practically uniform gravitational body force field, the Poisson's ratio does not influence the stress distribution. The presence of holes make the models and the prototypes multiply-connected. The loads are reacted at these holes hence their boundaries are not in self equilibrium. Due to this last condition the stresses do depend upon Poisson's ratio. However the fillet areas are sufficiently far from the holes, hence simple connection may be safely assumed.

For these reasons the relationship between model and prototype can be expressed by constant scaling factors. These may be determined from dimensionless ratios  $\pi$ , formed of relevant parameters. Such ratio for stress, using  $\sigma = W/A$ .

$$\pi_1 = \frac{\sigma BL}{W} \quad (5.10)$$

and from uniaxial deflection  $y' = WL/EA$

$$\pi_2 = \frac{y' EB}{W} \quad (5.11)$$

where  $L$  length and  $y'$  displacement are distances in the plane of the model and of the gear respectively.

$B$  the face width of the gear or the thickness of the model are transverse distances.

$W$  is the normal load

$E$  is Young's modulus

If for  $L$  and  $y'$  the same scaling ratio is chosen, and Eq. (5.10) is divided by Eq. (5.11), a new dimensionless ratio is obtained.

$$\pi_3 = \frac{\sigma}{E} \quad (5.12)$$

The similarity will be valid if the dimensionless ratios are the same for the model and for the prototype.

$$\left( \frac{\sigma}{E} \right)_m = \left( \frac{\sigma}{E} \right)_p \quad \text{then} \quad (5.13)$$

$$\frac{\sigma_m}{\sigma_p} = \frac{E_m}{E_p} \quad (5.14)$$

where  $m$  and  $p$  stand for model and prototype respectively. Using Eq's

(5.10) and (5.14), the load scale factor will be:

$$\frac{W_m}{W_p} = \frac{E_m}{E_p} \frac{B_m}{B_p} \frac{L_m}{L_p} \quad (5.15)$$

The scale factor for compliance from Eq.(3.5) and substituting L for y':

$$\frac{C_m}{C_p} = \frac{y'_m}{y'_p} \frac{W_p}{W_m} \quad (5.16)$$

The numerical values of the scale factors which emerged as design choices are:

$$\begin{aligned} \frac{L_m}{L_p} &= \frac{y'_m}{y'_p} = 5 \\ \frac{B_m}{B_p} &= \frac{6.35 \text{ mm } (.25 \text{ in})}{76.2 \text{ mm } (3 \text{ in})} = \frac{1}{12} \\ \frac{E_m}{E_p} &= \frac{2.34 \text{ GPa } (340 \text{ ksi})}{207 \text{ GPa } (30,000 \text{ ksi})} = \frac{1}{88.2} \end{aligned}$$

Therefore, the stress scale factor from Eq. (5.14):

$$\frac{\sigma_m}{\sigma_p} = \frac{1}{88.2}$$

The load scale factor from Eq. (5.15):

$$\frac{W_m}{W_p} = \frac{5}{(88.2)(12)} = \frac{1}{211.8}$$

The scale factor for compliances from Eq. (5.16):

$$\frac{C_m}{C_p} = (5)(211.8) = 1059$$

This scaling scheme assumes plane stress conditions, which is correct for the model. The B = 76.2 mm (3 in.) wide and t = 5.36 mm (.211 in.) deep cantilever beam for the prototype is definately a "wide

beam" ( $B/t = 14.2$ ) to which plane strain assumption fits better.

The problem of stresses in a wide beam was addressed by Wellauer and Seireg [30], Roark [24], p.134, Timoshenko and Goodier [28] in article 124. The aspect of deflections is dealt with by R.W. Cornell [8]. From these sources including some finite element investigation by the writer, no consistent simple factor has emerged for the transformation from narrow beam (plane stress) to wide beam (plane strain) analysis.

It was recognized that this matter requires a thorough investigation, hence it was excluded from the scope of this study. Plane stress was assumed, with the understanding that the results do not reflect the more realistic plane strain condition for the prototype.

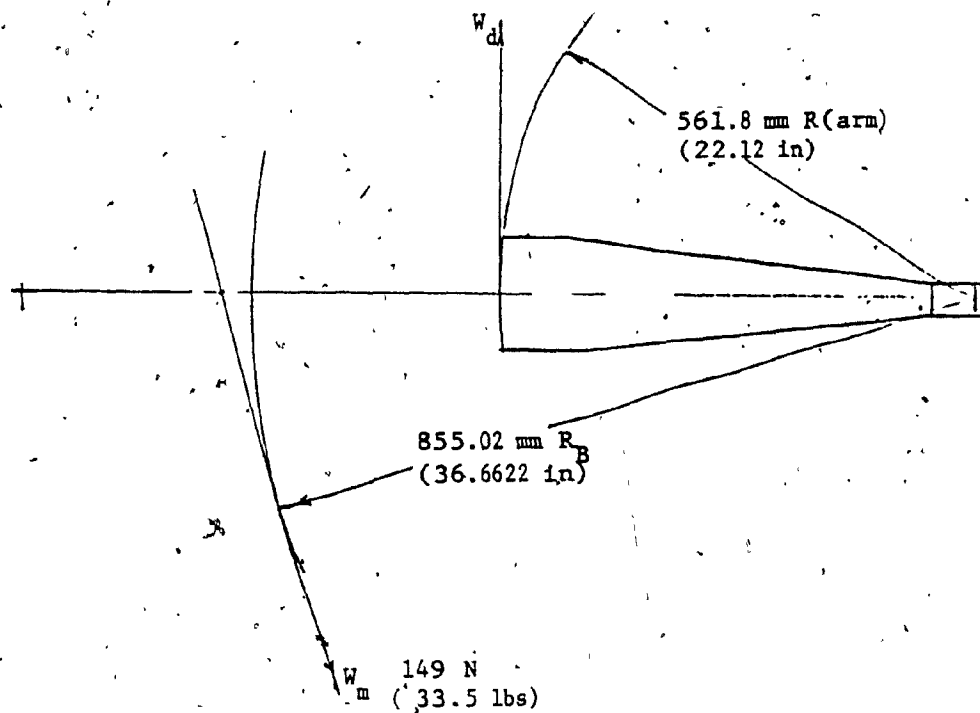
### 5.3.0 Loading

The prototype normal load is given as 31,600 N, (7090 lbs) hence the model normal load:

$$W_m = 31,600 \text{ N} / 211.8 = 149 \text{ N (33.5 lbs)}$$

From equilibrium of moments for the rig the required deadweight is 227 N (51.0 lbs), (Fig. 5.3).

As the model was not completely free of residual stresses, it was decided that the load would be applied at two levels. The fringes were measured accordingly and the differences in load and in fringe readings were considered. Thus the residual stresses and the slowly changing environmental effects were cancelled out. The reduction in bias type error was somewhat offset by an increase in precision errors due to the two readings per data point in place of one.



From equilibrium of moments the necessary deadweights are:

$$W_d = \frac{855.02}{561.8} 149 = 227 \text{ N (51 lbs)}$$

FIG. 5.3 LOADING LAYOUT

For the Multiple Contact tests the following deadweight loads were used:

High level load	239 N	(53.7 lbs)
Low level load	- 12 N	- ( 2.7 )
Test load	227 N	(51.0 lbs)

For the Single Contact tests 50% of the test load was employed.

In the case of the deflection tests the low level load was reduced to 1.1 N (0.25 lbs) and the load required to produce a given deflection was measured each time.

The efficiency of load transmission was checked using a Ravee 5-500 N (1-100 lbs) range load cell. The ball bearing pulleys were found to pass 99.8% of the applied load through.

#### 5.3.1 Scheme of Loading Points

The loading points were first planned in terms of radial position on the wheel. Initially .5 mm (.020 in.) intervals were selected, starting from the pitch point. For one extreme, the critical tip loading, the point .127 mm (.005 in.) below the nominal outside radius was chosen, a conservative estimate of distance left intact on the profile by the actual tip rounding practice.

The matching radius on the wheel of such tip point on the pinion gave the innermost loading point. When the locations of simultaneous contacts were considered as loading sites, the orderly increments were lost. The number of loading points turned out to be 19. As two or three of these contacts were active at the same time, they determined the 8 loading stations.

Table 5.1 shows these stations and loading points with the radial

TABLE 5.1 Loading Scheme

Radial Position of Contact R(wheel), R'(pinion) and its Normalized Position Along the Line of Action (S')

Loading Station S' nom.	Loading Point S'	R on Tooth B mm	R' on Tooth D mm	Loading Point S'	R on Tooth C mm	R' on Tooth C mm	Loading Point S'	R on Tooth D mm	R' on Tooth B
-.43				-.43	179.8	46.1	.57	177.6	48.5
-.22				-.22	179.3	46.5	.78	177.1	49.1
0	-1.00	* 181.3 (181.2)	45.3 (45.4)	0	178.8	47.0	1.00	176.7 (176.6)	49.9
.23	-.77	* 180.7	45.6 (45.5)	.23	178.3	47.5	1.23	176.3	* 50.6 (50.5)
.33	-.67	180.4 (180.5)	45.7	.33	178.1	47.8	1.33	176.0 (176.2)	* 51.0 (50.9)
.46	-.54	180.1	45.9 (46.0)	.46	177.8	48.2 (48.1)			
.70	-.30	179.5 (179.6)	46.4 (46.3)	.70	177.3	48.9 (48.8)			
.82	-.18	179.2	46.6	.82	177.0	49.3			

The theoretical radii of contact are listed. Where the actual values are deviating, they are shown in parentheses.

\* Indicates a location with tip relief

positions on the wheel (R), their matching radii on the pinion (R') and their normalized position (S') on the line of action.

$$S' = \frac{S}{P_B} \quad (5.17)$$

where S is the position of the load on the line of action

$P_B$  is the base pitch

The sign of S' corresponds to the pinion being the driver, which reflects the condition on the engine. On the test this direction is reversed, the load is applied through the wheel, which allowed the use of smaller deadweights.

The identification of the teeth is shown on Fig. (4.8), p.81.

#### 5.4 Stress Measurement

##### 5.4.1 The Photoelastic Method

The model is made of a "temporarily birefringent" material, which is a property of most transparent plastics. When a point in such material is in the state of two dimensional stress and is illuminated by a pencil of polarized light, the latter separates into two wave fronts. Each front is polarized in one of the two principal stress directions, and propagates with different velocities. Whence the name of birefringence. The change of velocity in each front is proportional to the corresponding principal stress. The absolute velocities cannot be measured in ordinary photoelasticity. However as the fronts traverse the model they accumulate a relative retardation, consequently they emerge with a phase shift. In the polariscope this phase shift is made visible. The interference phenomenon is utilized, resulting in dark and bright fringes. With white light illumination one value of relative



retardation corresponds to different phase shifts for each wave length. A given stress difference extinguishes a particular wave length but transmits the complementary colours, resulting in a colourful "Isochromatic" fringe pattern. Such fringe is the locus of points where the difference between the principal stresses is constant.

$$\sigma_1 - \sigma_2 = N'f/B \quad (5.18)$$

ref [10], chapter 7

where  $N'$  is the fringe order

$B$  is the thickness of the model

$f$  is the "material fringe value" [kPa-m] (psi-in) which is determined by calibration

The isochromatic fringes are clearly visible when the light extinction associated with the orientation of the principal stresses is suppressed, which is achieved by interposing the so called "Quarter wave plates." In this mode the instrument is a "Circular Polariscope". The plates are optically removed in the "Plane Polariscope". These settings of the instrument are explained in detail in ref. [10], Chapters 6 & 7. In the Plane Polariscope additional fringes appear, the so called "Isoclinics". Such fringe is the locus of points where the direction of one set of principal stresses coincides with the angular tilt of the instrument. This position is read off a dial, thus the orientation of the principle stresses may be determined.

The tranformation of the polariscope from one mode to the other is simply rotating  $45^\circ$  the quarter wave plates by the means of a lever.

#### 5.4.2 Calibration

Its objective is to relate the fringe orders observed to the stresses in the model. This may be achieved by counting the fringes in

a suitably loaded specimen for which the stresses may be reliably known. In a tensile strip loaded in uniaxial tension the stresses are:

$$\sigma_1 = \frac{W}{tB} \quad \sigma_2 = 0 \quad (5.19)$$

where  $W$  is the normal load

$B$  is the thickness of the strip

$t$  is its width.

substituting (5.19) into (5.18) gives the material fringe value:

$$f = \frac{W}{tN'} \quad (5.20)$$

As the pinion and the wheel were cut from different sheets, one tensile strip was made from each. The specimens were subjected to incremental loading, the fringe order  $N'$  was plotted vs the load. The "best fit" straight line was determined using the method of "Least Squares". An "improved"  $N'$  was then calculated corresponding to a 445 N (100 lbs) load. The following material fringe values were found, using Eq. (5.20):

$f = 7.10 \text{ kPa}\cdot\text{m}$  (40.95 psi-in) for the pinion

$f = 6.95 \text{ kPa}\cdot\text{m}$  (40.07 psi-in) for the wheel.

#### 5.4.3 Determination of Stresses

The fringe orders along the fillets were measured. As the normal stress on a free surface is zero, these fringes give directly the tangential stresses. White light illumination was used, which allows to recognize the integer fringe orders with ease. The fractional fringe orders were determined using Tardi compensation, which is fully explained in ref. [10], Chapter 9.

The accuracy of the location of the measurement is just as important as it is for the fringe orders. Therefore a travelling telemicroscope was used equipped with stage micrometers. The angular positions were found using a protractor reticle.

The fringe orders were recorded at  $10^\circ$  positional increments, the maxima were determined to the nearest integer degree. The fringe measurements were substituted into Eq. (5.18) thus the model stresses were obtained. The latter set was multiplied by scaling constant 88.24, giving the prototype stresses.

For the Multiple Engagement tests two teflon shims were placed between each pair of contacting teeth. Thus friction was reduced to  $\mu=0.1$ . In the Single Pair Engagement runs the shims served an additional purpose. By fitting with the teflons only the pair to be loaded, the unwanted contacts were removed.

#### 5.5 Pair-Deflection Measurements

The search for finding a viable method lead to a improved parameter: the "Relative Pair Deflection".

Deflections of single pairs were considered. Single contact was achieved here by inserting a precision ground shim stock into the contact of the pair, the deflection of which was sought. At a small initial load of 1.1N (.25 lbs) only the shimmed pair was engaged, the adjacent contacts were separated. As the load was increased by small increments the shimmed pair has deflected and the gap at the adjacent pair gradually closed.

The closing of the gap was determined optically. Even a very slight contact is easily recognized due to the comparatively high

Hertzian stresses. e.g. Due to a load of 0.5N (0.1 lbs) a pressure of 538 kPa (78 psi) may develop at the contact. The brightness of the corresponding fringe order of 0.50 makes these slight contacts highly visible against the dark background in the polariscope.

First the initial clearances were determined, those created by tip modification and the smaller ones due to manufacturing errors. This was achieved by using so called "onion papers", the finest of which measures a mere 0.005 mm (.0002").

For setting deflections in fine increments the thickness of the precision shim stock ranged from 0.025 mm (.001") to 0.254 mm (.010").

The magnitude of the deflection was considered to be the width of the gap being closed, which was equal to the thickness of the shim plus the initial clearance established previously by the onion paper.

The corresponding load was taken as the difference between the load at which the second contact reappeared minus the initial load of  $W_d = 1.1 \text{ N } (.25 \text{ lbs})$ .

At each loading point 6 to 8 deflection increments were measured and recorded with the corresponding loads.

This method gave the relative deflection between the shimmed and observed contacts. As both contacts lie on the line of action the loads and the deflections are all in the required direction. No artificial reference datum is imposed, the motions reflect the true action of the teeth.

The measurements are sufficiently sensitive, the resolution of the loading is 1.1 N (.25 lbs) or 1% of the "single pair load level"  $W_d = 113 \text{ N } (25.5 \text{ lbs})$ .

ALTERNATIVE ANALYTICAL METHODS

The objectives of this experimental investigation will be analysed using other techniques also, which are described in the following. The numerical results will be compared in Chapter 7.

6.1 Application of the Kelly-Pedersen Formula [20]

This was chosen as a sample from the family of projection type formulas. For convenience Eq. (2.12) is repeated here:

$$\sigma_t = \frac{W}{B} \left[ 1 + .26 \left( \frac{e}{r_f} \right)^{0.7} \right] \left[ \frac{1.5a_1}{e^2} + \frac{\sin \beta}{2e} + \frac{0.45}{(b_2 e)^{\frac{1}{2}}} \right]$$

The construction for this expression is based on the Lewis layout, where the key step is to find the point of tangency "A", between the parabola and the fillet radius as in Fig. (2.1). The graphical solution is cumbersome and inaccurate, therefore it was replaced by calculation. The nomenclature is shown in Fig (2.1).

$$\text{let } h' = y_D - y_C - x_D \tan \lambda \quad (6.1)$$

$$\text{then } l' = h' + r_f \sin \gamma_L \quad (6.2)$$

$$\text{also } l' = \frac{t}{4} \cot \gamma_L = \frac{(x_C - r_f \cos \gamma_L) \cos \gamma_L}{2 \sin \gamma_L} \quad (6.3)$$

which may be reduced to:

$$r_f = \frac{x_C \cos \gamma_L - 2h' \sin \gamma_L}{\sin^2 \gamma_L + 1} \quad (6.4)$$

Solving for  $\gamma_L$  locates point A. This may be done by trial and error, using a programable hand calculator. The other parameters in Eq. (2.12) may be read off Fig. (2.5).

$$\gamma_{KP} = \gamma_L + \epsilon_{KP}$$

for the second term using Eq. (2.13):

$$\gamma_{KP} = \gamma_L + 25^\circ - \gamma_L/2 = 25^\circ + \gamma_L/2 \quad (6.5)$$

$$e = x_C - r_f \cos \gamma_{KP} \quad (6.6)$$

$$a_1 = (h' + r_f \sin \gamma_{KP}) \cos \lambda \quad (6.7)$$

$$b_2 = [(e - x_D)^2 + (y_D - y_C + r_f \sin \gamma_{KP})^2]^{\frac{1}{2}} \quad (6.8)$$

$$\beta = \gamma_{KP} - \lambda \quad (6.9)$$

## 6.2 Application of the Aida-Terauchi Formula [2]

The rational structure of the formula lends itself to include the calculation of the compressive maxima. Eq. (2.26) is repeated here in a slightly modified form to facilitate this latter application. The nomenclature is shown in Fig. (2.12).

$$\sigma_t, \sigma_c = \left[ 1 + 0.8 \frac{t}{r_f} \right] \{ \pm [ .66\sigma_b + .40 (\sigma_b^2 + 36 \tau^2)^{\frac{1}{2}} ] + 1.15 (\sigma_{rd} \pm \sigma_{rb}) \} \quad (6.10)$$

where the +ve sign applies to the maximum tensile,

the -ve sign to the maximum compressive fillet stresses.

The "direct component" of the nominal radial stress is:

$$\sigma_{rd} = - \frac{W \sin \lambda}{bt} \quad (6.11)$$

The "bending component" for the same:

$$\sigma_{rb} = - \frac{6 W a_1 \sin \lambda}{bt^2} \quad (6.12)$$

The term in the bracket of Eq. (6.10) is the nominal stress due to the bending component of the load. This effect is symmetrically opposite for the tensile and compressive fillets.  $\sigma_{rd}$  is compressive for both sides. However as the radial component of the load acts off

the centerline of the tooth,  $\sigma_{rb}$  is compressive for the tensile fillet and causes tension on the compressive fillet.

This formula may be used also to account for the effects of frictional forces acting tangentially at the contacts. The superposition of this traction modifies the loading and the formula may be applied without change.

Results may justify the extension of the formula. It has worked for this pair of gears, but for full acceptance some further evidence would be needed.

### 6.3 Using the Cornell-Westervelt Dynamic Program

A computer program based on the dynamic analysis in ref's. [9] and [8] was written and was made available for testing. By running it at a very slow speed input (2 rpm) an essentially static analysis was obtained.

This program first optimizes tooth proportions and calculates pair compliance. Then it determines the sharing of the dynamic loads between a possible maximum of (4) pairs of teeth. Finally it computes the tension stress peaks produced by the previously obtained load fractions individually on each of the respective teeth.

The effects of speed, composite tooth error, profile modification, backlash allowance, thermal expansion, manufacturing tolerances, center distance variation are all taken into consideration.

For the computation of compliance, depending upon the ratio of face width over arc tooth thickness, optionally plane stress or plane strain calculation may be selected. As an additional option this operation may be bypassed and the user may input its own compliance

constants. The optimization process in the program may be modified by an input allowing an arbitrary increase in arc tooth thickness for one gear at the expense of the mating one.

In the output the gear data are listed in detail. Compliance properties are given in the form of constants fitting Eq. (2.45). Hertzian and maximum tension stresses are printed out. Tooth load sharing, contact and peak root stresses are also available in graphical form as an option. A sample of load sharing curves is shown in Fig. (6.1). The load ratio is the fraction of the individual branch loads with respect to the total load.

The horizontal axis extending from 0 to 1.00 represents one base pitch. The simultaneous contacts are plotted as they occur giving a compact presentation of the full length of the line of action.

The vertical lines were added onto the computer generated graphs by hand. They represent the experimental loading stations, with the simultaneously engaged loading positions identified by the typing. Thus the experimentally determined loads may be compared with those generated by the computer.

#### 6.4 An Application of Finite Elements

##### 6.4.1 Element Network

Grids representing the photoelastic models were constructed using triangular elements. The three central teeth were fully modelled, the side teeth were truncated leaving only the fillets, as in Fig's. (6.2 thru 6.6). The thickness of the elements was unity except at the polycarbonate reinforcing plates shown by the heavy lines, where it was 4 times that value. A typical side of an element in a general area of



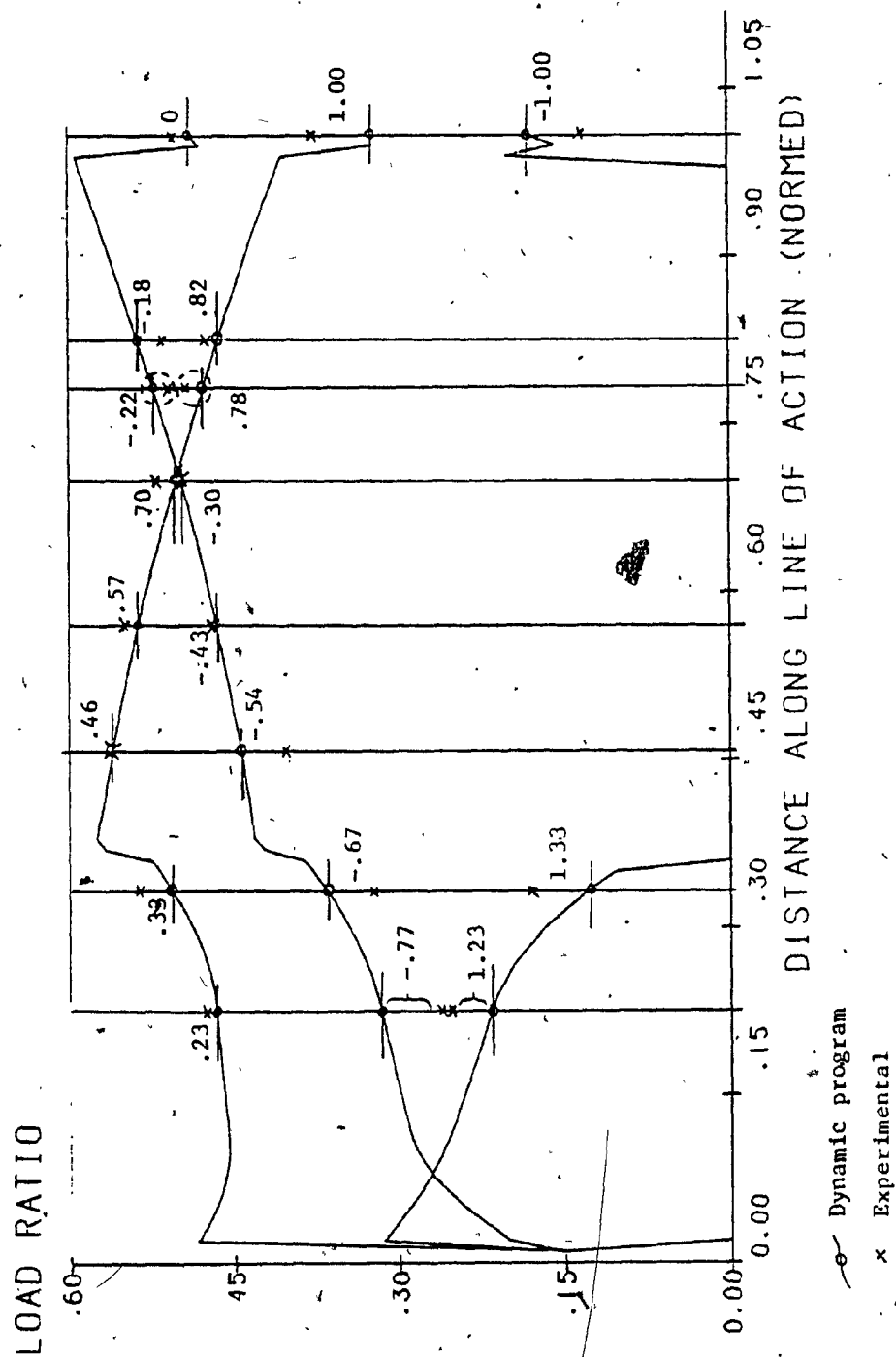
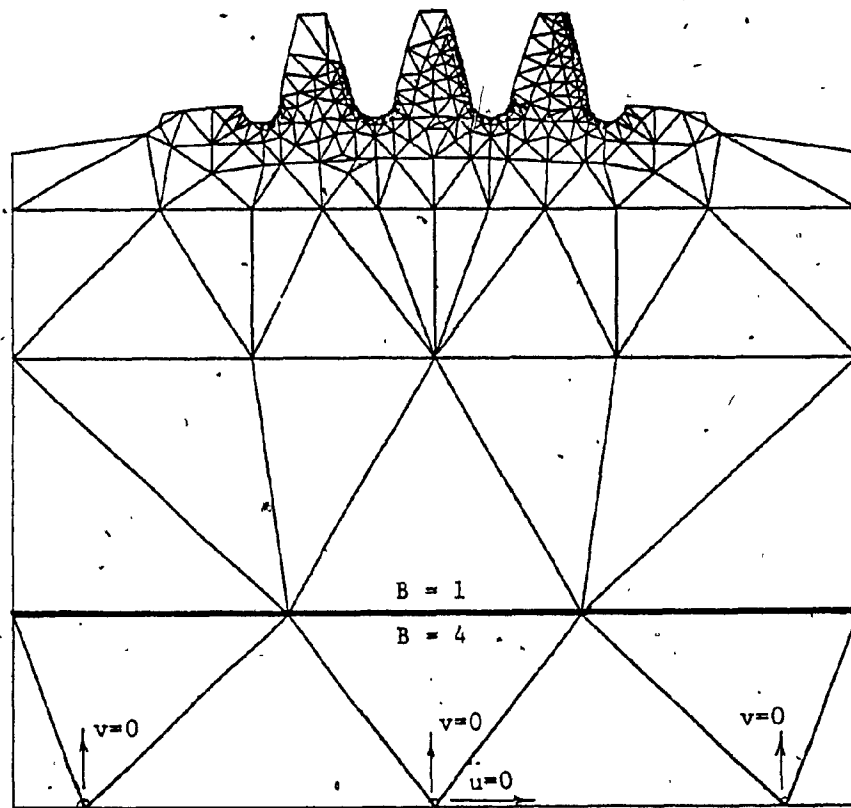


FIG. 6.1. LOAD SHARING - DYNAMIC PROGRAM



Number of elements: 882  
Number of primary nodes: 555

FIG. 6.2 FINITE ELEMENT MODEL - WHEEL

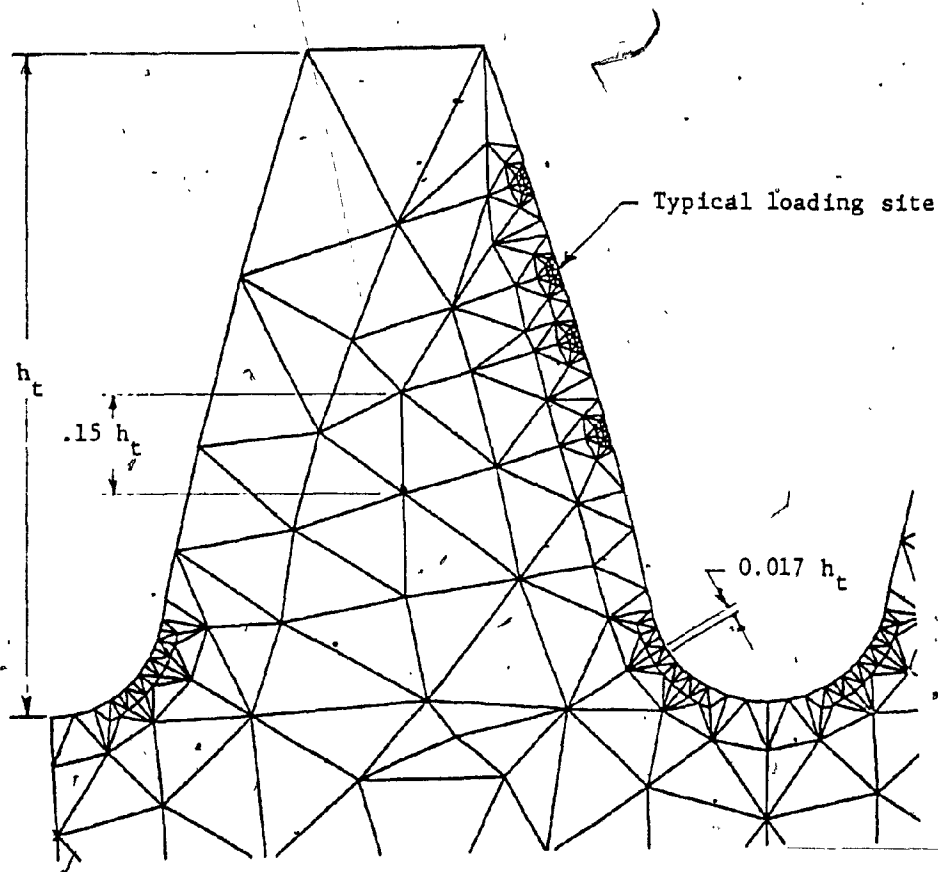


FIG. 6.3 FINITE ELEMENT GRID, CLOSE UP - WHEEL

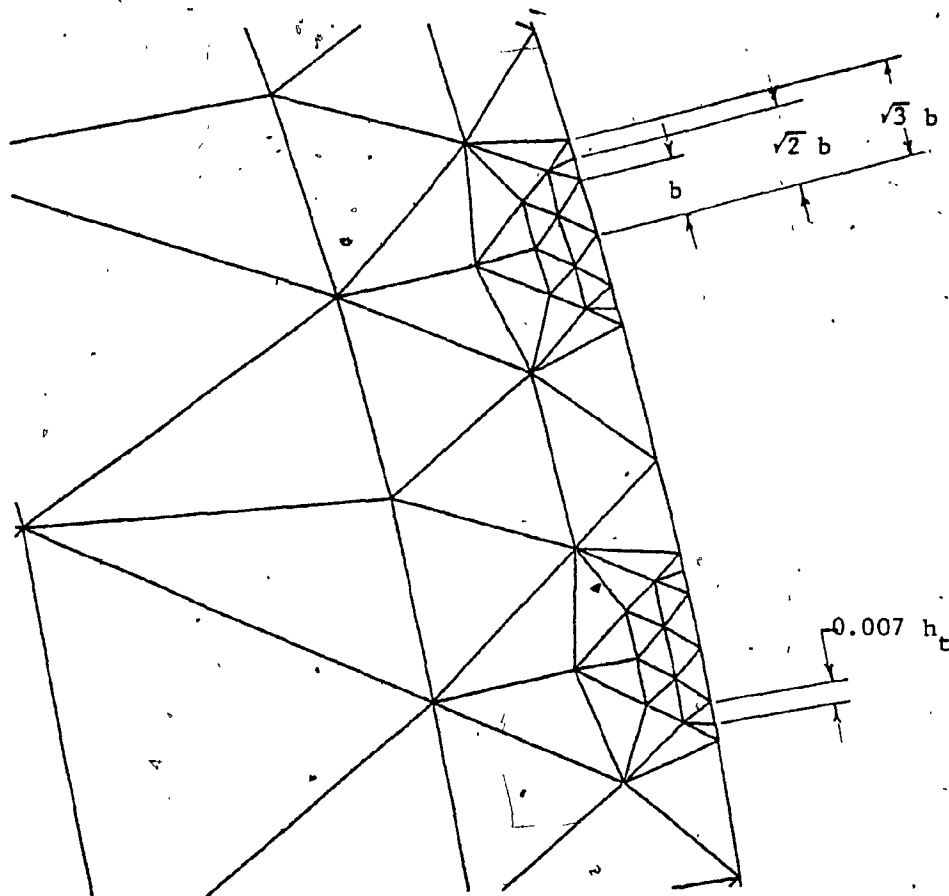
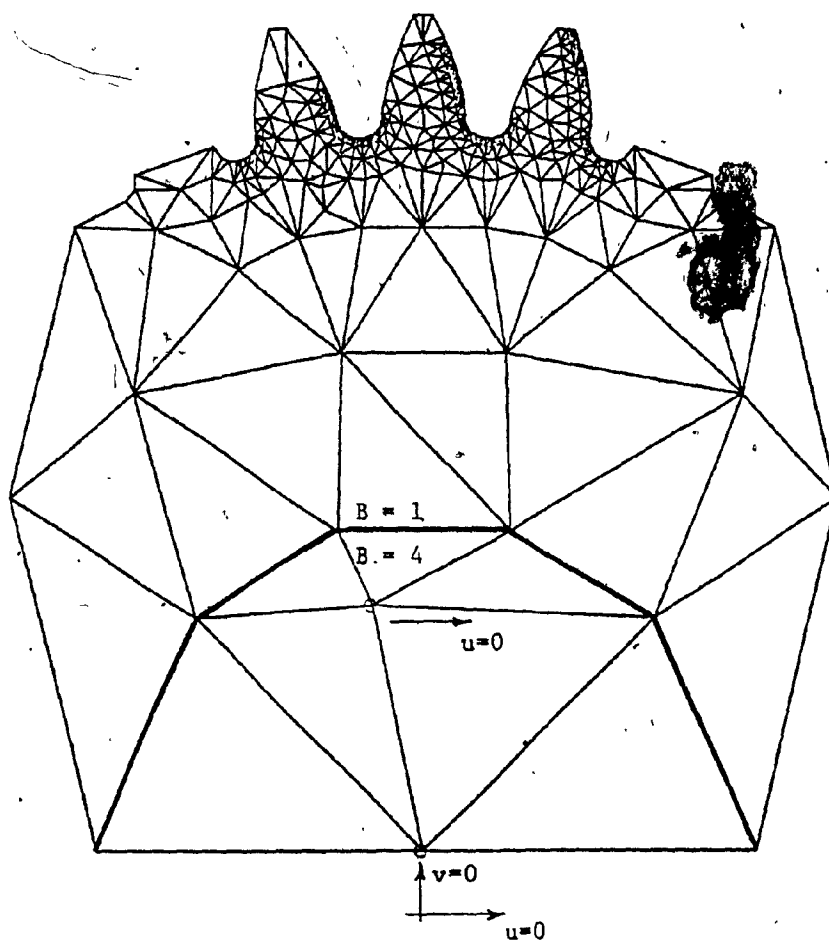


FIG. 6.4 FINITE ELEMENT GRID, CLOSE UP - TYPICAL LOADING SITE

L.KENEDY 3387. 2062. 846. 161181. 11618.

1.0000	XMMU, XMMU	-1.0000	1.0000	SM	0.0000
2.0110	YMMU, YMMU	0.0000	2.0110	SV	0.0000
0.0000	ZMMU, ZMMU	0.0000	0.0000	SZ	0.0000



Number of elements: 870

Number of primary nodes: 537

FIG. 6.5 FINITE ELEMENT MODEL - PINION

L.KENEL	6387.	8888.	848.	181181.	11818.
1.0000 XMMU, XMMU	-1.1529	.2087 0X	0.0000		
0.0110 YMMU, YMMU	1.6188	0.0183 0Y	0.0000		
0.0000 ZMMU, ZMMU	0.0000	0.0000 0Z	0.0000		

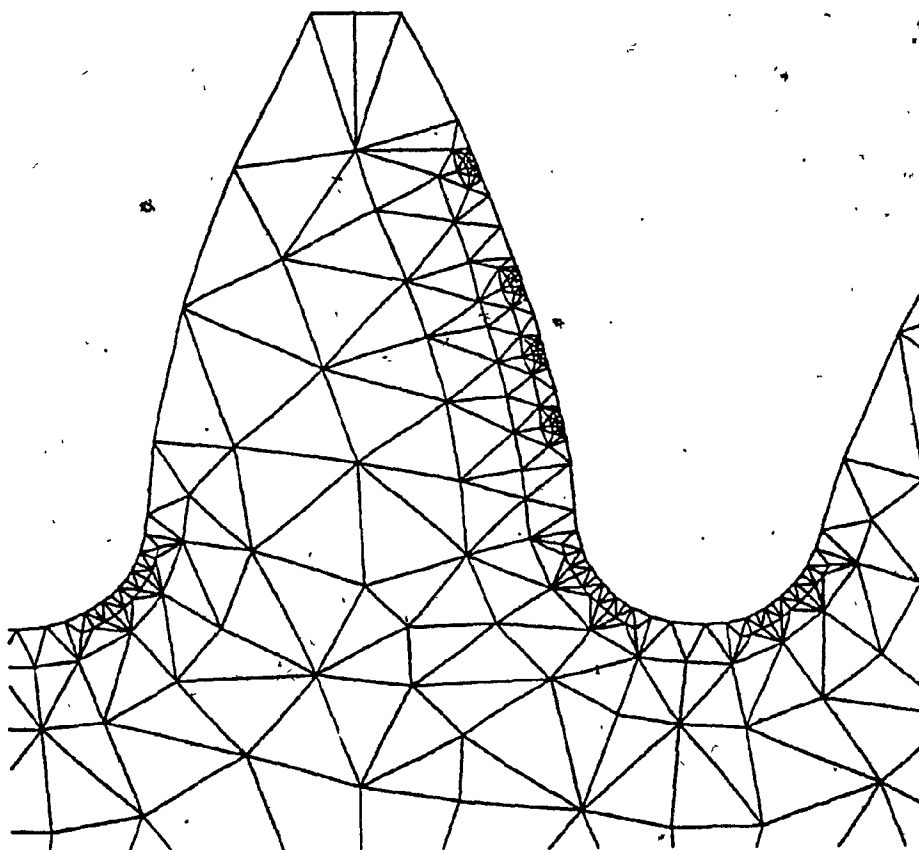


FIG. 6.6 FINITE ELEMENT GRID, CLOSE UP - PINION

the tooth was approximately 15% of tooth depth. The same for a fillet element was 1.7% and for those carrying the distributed load was 0.7%. The model for the wheel was constructed of 882 elements and 555 primary nodes. For the pinion 870 elements and 537 primary nodes were used.

#### 6.4.2 The Program

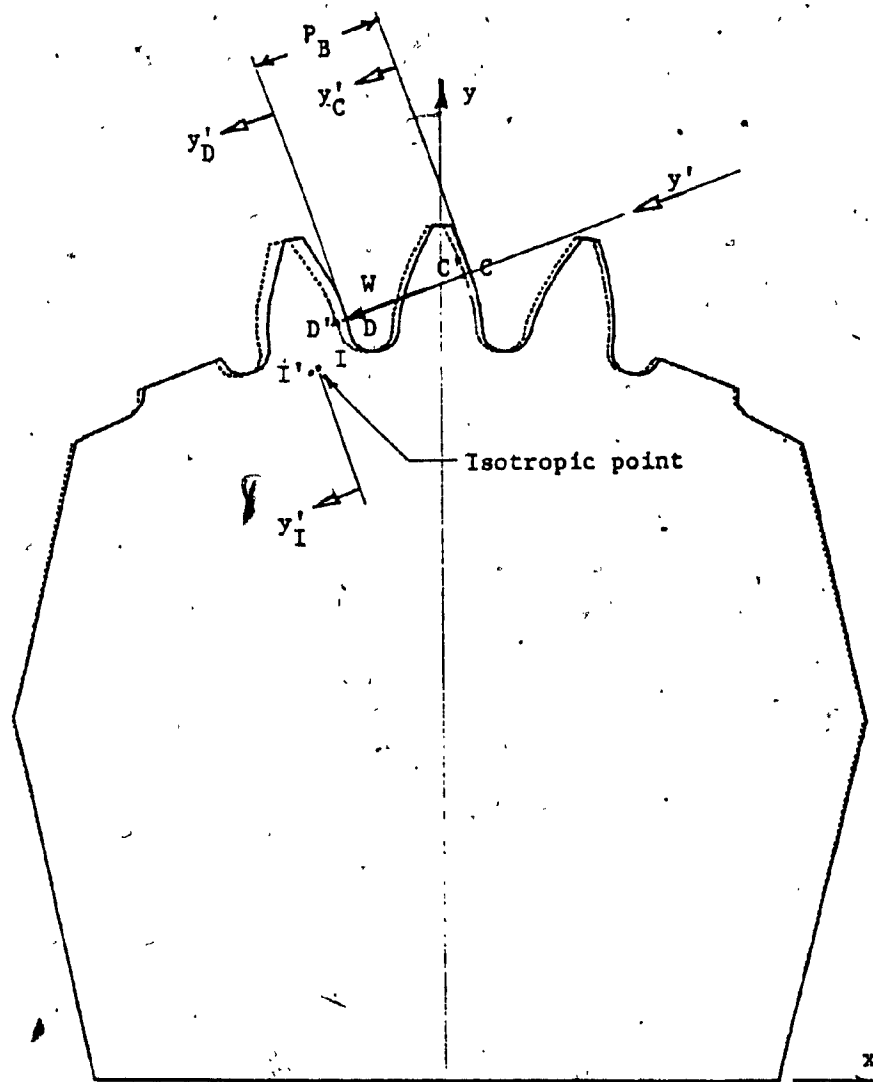
A versatile two dimensional Finite Element program was used for the task. It has sweeping capabilities such as handling plate and axisymmetric problems under external, centrifugal and thermal loading, with applying elastic, plastic and/or creep analysis. For this study only the elastic analysis of a plate under inplane external loads was needed.

Quadratic assumed displacement fields are employed. The corner nodes are specified by the user, additional midside nodes are generated internally. This allows more particulars in specifying boundary conditions and returns finer detail in the output. Plane stress or plane strain analysis may be chosen. In a standard output external and reaction forces, displacements at all nodes, coordinate stresses at the primary nodes and at the center of gravity of the elements are listed. Optionally the principal stresses may be included.

The program may be linked up with a graphics program, which displays the network. This was instrumental in debugging the input and for printing Fig's. (6-2 thru 6.6). The output was treated similarly giving samples of the deflected shape for the pinion, Fig. (6.7) and of the isostress lines for principal stresses Fig's. (6.8 & 6.9).

#### 6.4.3 Boundary Conditions

As the photoelastic models were held in space by a pair of large



"Absolute" deflection:  $y'_D - y'_I$

"Relative" deflection:  $y'_D - y'_C$

FIG. 6.7 DEFLECTED SHAPE, - PINION



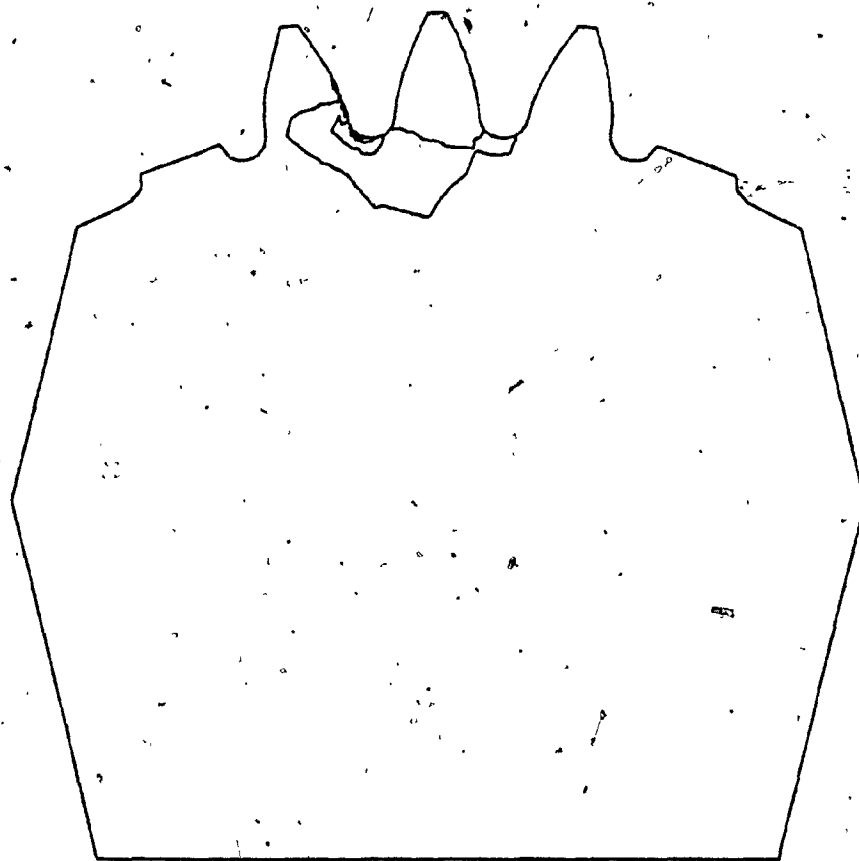


FIG. 6.8 ISOSTRESS LINES, MAJOR PRINCIPAL STRESSES - PINION

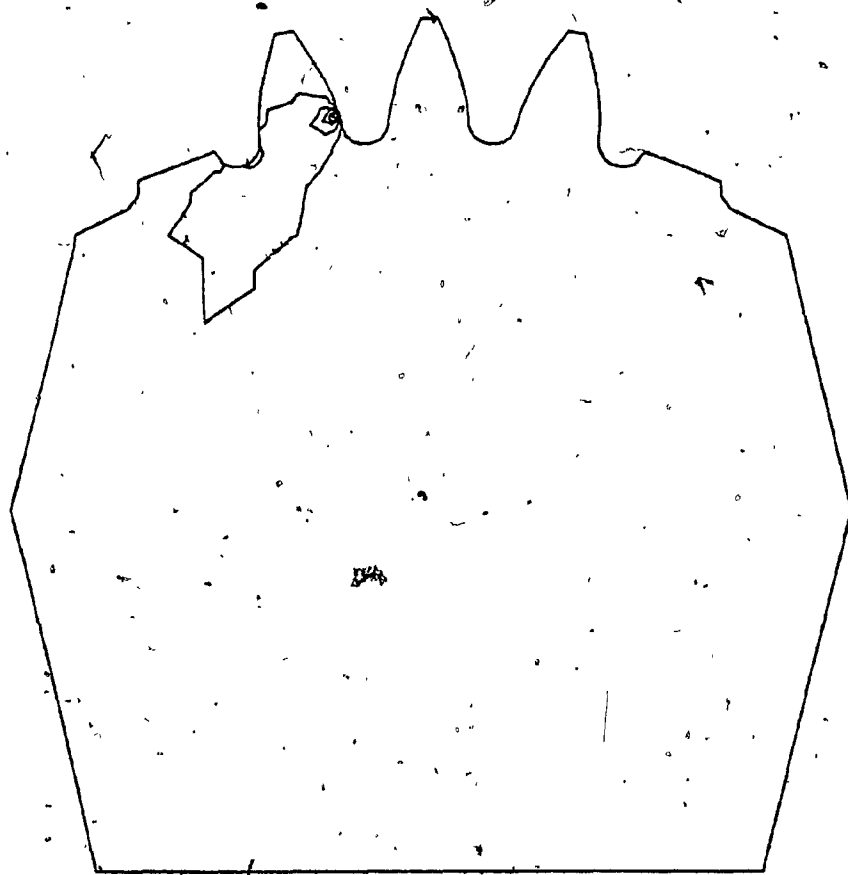


FIG. 6.9 ISOSTRESS LINES, MINOR PRINCIPAL STRESSES - PINION.

diameter pins, the finite element models were also fixed at nodes representing these points.

#### 6.4.4 Loading

It was intended to reproduce the Hertzian displacements as closely as feasible. Therefore the grid at the sites for the contacts were prepared for that purpose. Due to the non linear nature of the displacement as in Eq. (2.44), incremental loading was planned. The spreading of the contact width was to reach precisely a new pair of primary nodes at each increment.

The width of the rectangle at the contact of two parallel cylinders pressed against each other is proportional with the square root of the load as in Eq. (2.29). Hence if the subsequent load levels are

$$W_b = 2W_a \quad \text{and} \quad W_c = 3W_a$$

then the subsequent widths of the contact rectangles will be:

$$b_b = \sqrt{2} b_a \quad \text{and} \quad b_c = \sqrt{3} b_a \quad (6.13)$$

Distributed loading is represented by so called "work-equivalent" or "consistent" loads acting at the nodes. These may be calculated for a parabolically distributed line load, spread over the edge of an element from:

$$W_1 = \frac{L}{30} (4p_1 + 2p_2 - p_3)$$

$$W_2 = \frac{L}{30} (2p_1 + 16p_2 + 2p_3)$$

$$W_3 = \frac{L}{30} (-p_1 + 2p_2 + 4p_3)$$

(6.14)

where  $W_i$  represent consistent nodal loads

$p_i$  represent the intensities of the distributed line loading at the nodes

Nodes 1 and 3 are primary, node 2 is a midside node.

Eq's. (6.14) are derived in Appendix (1), which was based on ref's [11] and [16]. The distances between the nodes were determined using the rule set by Eq's. (6.13).

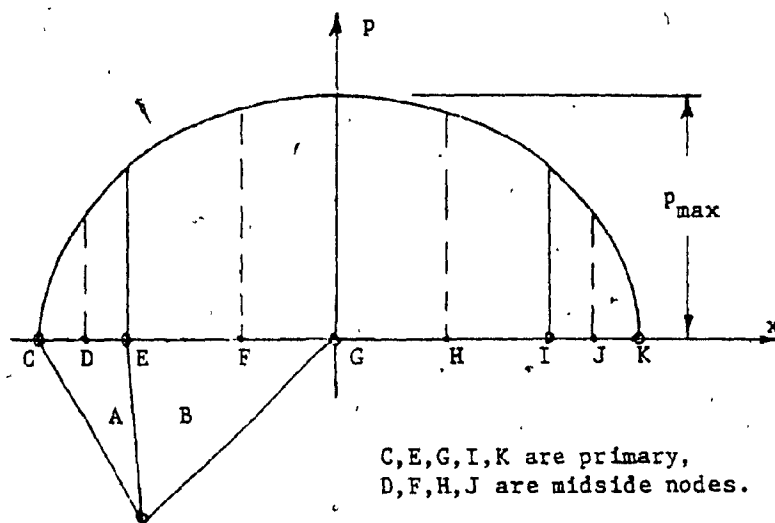
An elliptic load distribution of a contact extending over five primary nodes is shown in Fig. (6.10). The load intensities were obtained from Eq. (2.28) repeated here for convenience:

$$P = P_{\max} [1 - (x/b)^2]^{\frac{1}{2}}$$

where  $P_{\max}$ , the vertical half axis of the ellipse, represents the maximum load intensity. For normalization purposes the total load was first taken as unity, which must equal the area of the half ellipse.

$$A = \frac{1}{2} P_{\max} b \pi = 1 \quad (6.15)$$

Then using Eq's. (2.28), (6.15) the pressure at each node was determined. Next the fractions of the consistent loads over each element were calculated employing Eq's. (6.14). Finally the fractions of nodal loads were assembled as shown in Fig. (6.10) for three load levels. The results are listed in Table (6.1).



For element "A"

$$P_1 = P_C$$

$$P_2 = P_D$$

$$P_3 = P_E$$

For element "B"

$$P_1 = P_E$$

$$P_2 = P_F$$

$$P_3 = P_G$$

Giving nodal loads for each element using Eq's. (6.14):

$$W_{1A}$$

$$W_{2A}$$

$$W_{3A}$$

$$W_{1B}$$

$$W_{2B}$$

$$W_{3B}$$

Then the assembled nodal loads are:

$$W_C = W_{1A} = W_K$$

$$W_D = W_{2A} = W_J$$

$$W_E = W_{3A} + W_{1B} = W_I$$

$$W_F = W_{2B} = W_H$$

$$W_G = 2 W_{3B} \quad \text{by symmetry}$$

FIG. 6.10 / CONSISTENT LOADS [11]

Table 6.1 Non-dimensional Load Fractions

Contact extending to:	3	5	7
	primary nodes		
Node #			
1			.001
1-2			.031
2		.003	.027
2-3		.061	.072
3	.032	.080	.072
3-4	.338	.276	.233
4	.260	.160	.128
4-5	.338	.276	.233
5	.032	.080	.072
5-6		.061	.072
6		.003	.027
6-7			.031
7			.001
Total	1.000	1.000	1.000

Note: Midside nodes are indicated by the adjacent corner node numbers.

To determine the load which would extend the width of the contact to a predetermined distance, Eq. (2.29) was used. This is rearranged here:

$$b = \left[ \frac{8W}{\pi B} \frac{r_1 r_2}{r_1 + r_2} \frac{1-v^2}{E} \right]^{\frac{1}{2}} = \left( \frac{W}{B} K_3 \rho \right)^{\frac{1}{2}}$$

where:

$$K_3 = \frac{8(1-v^2)}{\pi E} \quad (6.16)$$

$$\rho = \frac{r_1 r_2}{r_1 + r_2} \quad (6.17)$$

hence:

$$W = \frac{b^2 B}{K_3 \rho} \quad (6.18)$$

The face width  $B$  of the gears and constant  $K_3$  do not vary with the position of the contact. The equivalent radius of curvature " $\rho$ " was calculated for each loading point. The required half width of the contact determined the magnitude of the total load over a given site. The load fractions were then calculated and the group was orientated into the normal direction at the central primary node of the contact.

#### 6.4.5 Determination of Deflections - Using Novel Reference Data

The main objective of this investigation is to determine the flexibility of these gear teeth. As everything deflects, the choice of a suitable datum such that "all relevant displacements but nothing else" would be included is of paramount importance.

The dynamic program considers tooth deflections only, but includes the effects of the elastic nature of the foundation region.

This datum is determined by maximizing deflections. A reasonably specific point may be found by entering photoelastic considerations. In the photographs of Fig. (7.11), p.133 certain black areas appear in the foundation region repeatedly. These spots move with the position of the load. Inside these areas there is an "Isotropic Point" which is unique for a given loading. Its location may be determined by using the isoclinics mentioned in Paragraph 5.4.1.

The black colour indicates that  $\sigma_1 - \sigma_2 = 0$ . Therefore such point is in a state of pure hydrostatic stress. The shear strain here is zero, hence no local rotation, only translation can take place. It represents the distortion free displacement of the rim.

This property makes the isotropic point a suitable datum. From here on the displacement at a contact in reference to the isotropic point will be labelled as an "absolute" deflection, which excludes the rigid body displacements of the rim. These deflections are comparable with those generated by the dynamic program.

In contrast, the displacement at a contact relative to the displacement at the contact site on the adjacent tooth is defined by the parameter of "relative deflection". The equivalents of the latter were measured experimentally.

The locations of the isotropic points, each corresponding to a loading site, were determined using the photoelastic models. Then a node was assigned to each such point in the finite element model. Thus the advantages of photoelasticity and finite element analysis are combined.

In all cases, first the resultant displacements were computed and



then these were resolved into components along the line of action, and those perpendicular to it. The former gave the deflections, the latter represent sliding.

The versatility of the finite element method yields a common ground to compare the results from the dynamic program with those from the physical model.

At each loading site the loads were applied in three increments. Thus, including zero load, four points became available to expose the suspected non-linearity.

#### 6.4.6 Determination of Fillet Stresses

The fillet stresses due to single tooth loading were extracted from the output of the third load level computer runs. Then they were linearly adjusted to the standardized single engagement prototype load of 15.8 kN (3545 lbs). The output was plotted and smooth lines were drawn through the data points, which constitute the final results.

The tooth loads on Multiple Engagement runs were based on the compliance results and on the subsequent load sharing analysis.

Four group loadings were applied to each model.

RESULTS & CORRELATION WITH ALTERNATIVE METHODS.

The data are expressed in terms of the prototype. The reader may relate to these results better than, for example, to the small stresses in the plastic. The scaling factors were described in Paragraph 5.2.

The fillet stresses are plotted vs angular position. The zero polar position is defined by the line connecting the centers of the tensile and compressive fillet radii for a tooth. Positive angles are reached through anti-clockwise rotation. At points I and J as in Fig. (7.1) the fillet circle blends into the short segment of the root circle. They are at slightly different angles for the pinion and for the wheel.

The position of the load is defined as "Normalized Position Along the Line of Action", referred to as  $S'$  and is obtained by dividing the directed distance from the pitch point over the base pitch. Thus distances between contacts are integer numbers and the full length of the engagement gives the contact ratio. Such normalization provides common ground for pinion and wheel data.

"Best fit" lines were drawn "by eye" aided by "French curves" though numerical curve fitting could have been applied for this purpose.

#### 7.1 Stresses - Single Tooth Pair Engagement

Samples of fillet stress distribution vs fillet angles due to loads acting on individual teeth, are shown in Fig's. (7.1), (7.2) and (7.3) for the wheel and in Fig's. (7.4), (7.5) and (7.6) for the pinion. The tensile and the compressive peak stresses and their angular location are plotted vs normalized position along the line of action in Fig's. (7.7) thru (7.10).

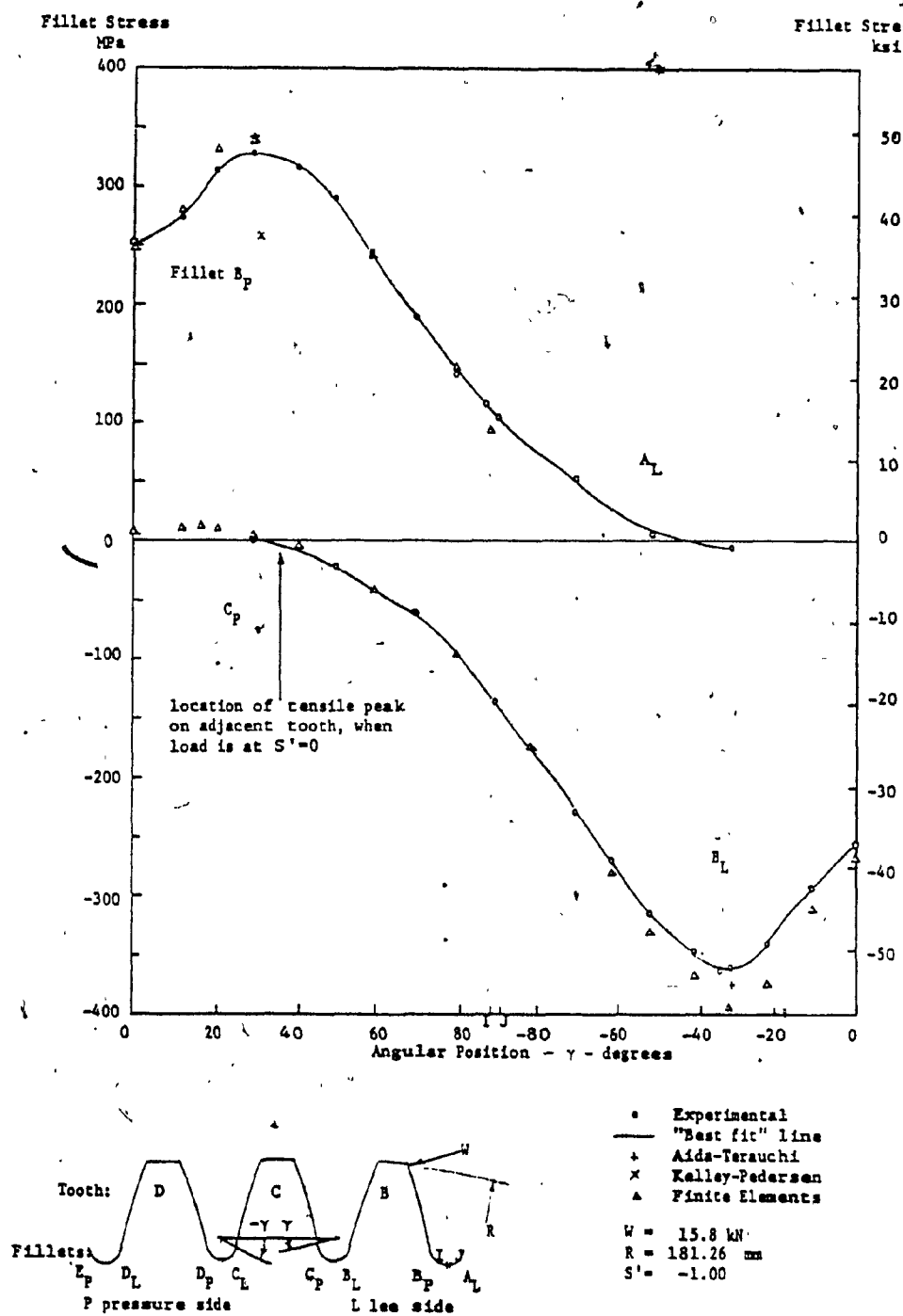


FIG. 7.1 FILLET STRESSES VS. ANGULAR POSITION,  
SINGLE ENGAGEMENT - WHEEL,  $S' = -1.00$

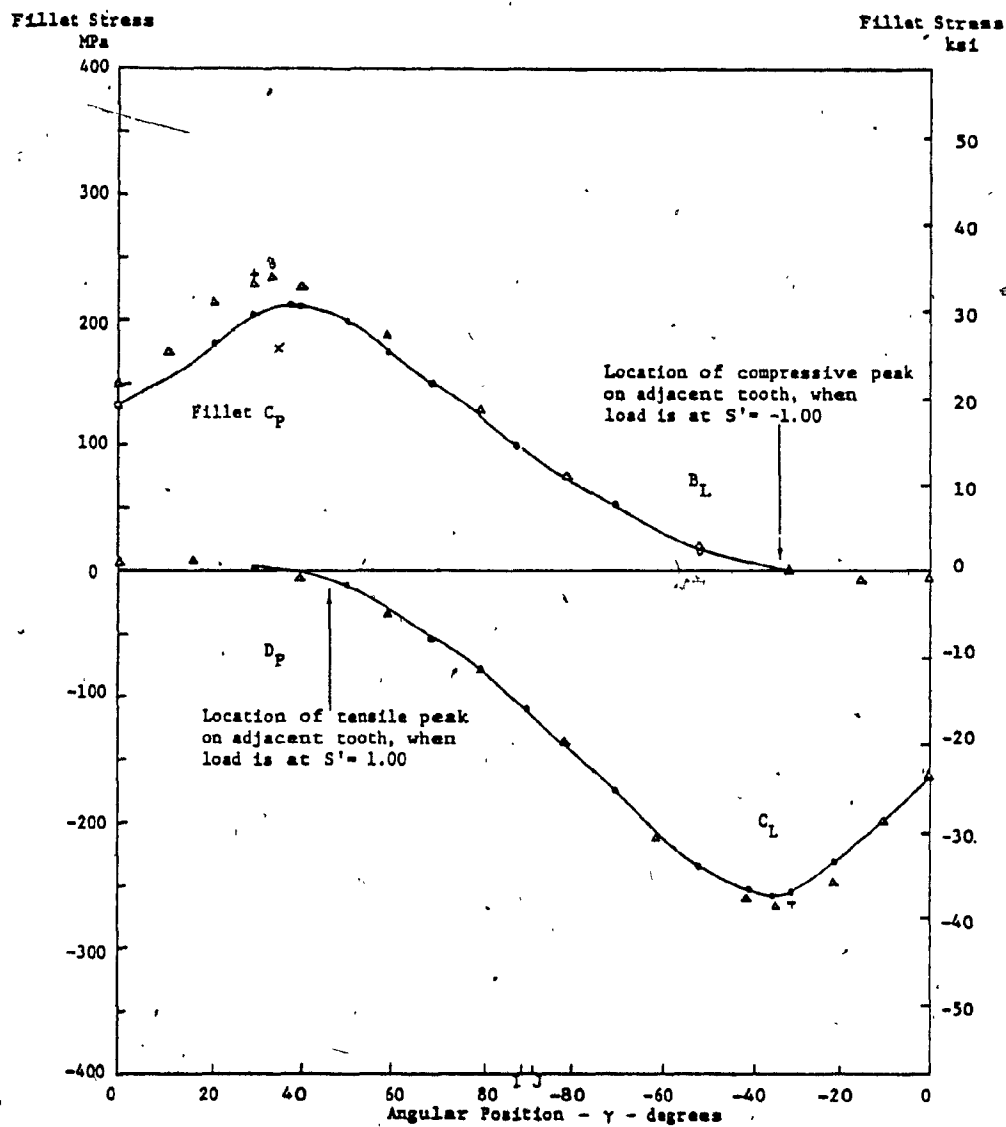


FIG. 7.2 FILLET STRESSES VS. ANGULAR POSITION,  
SINGLE ENGAGEMENT - WHEEL,  $S' = 0$

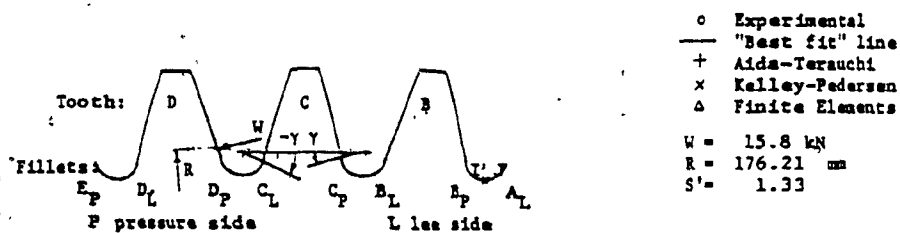
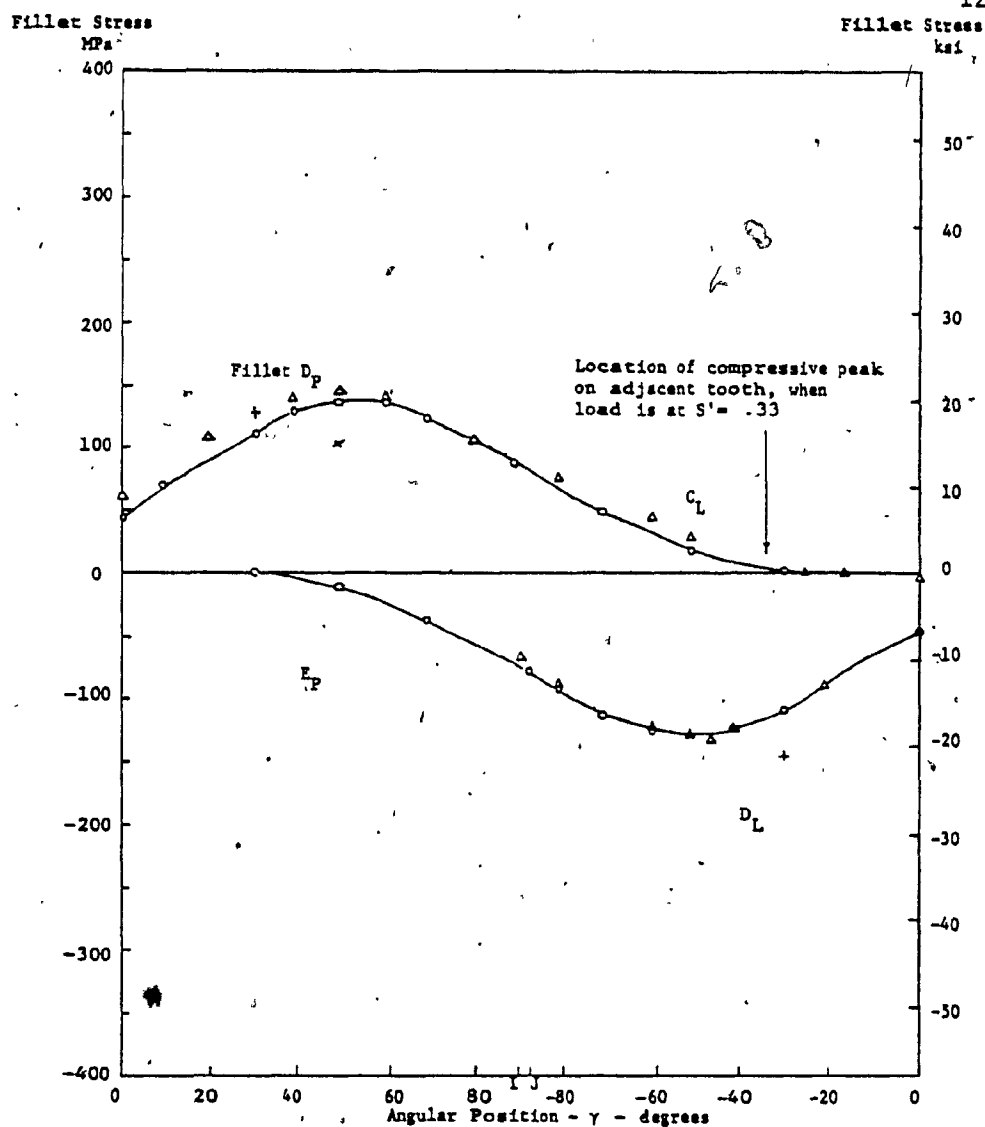


FIG. 7.3 FILLET STRESSES VS. ANGULAR POSITION, SINGLE ENGAGEMENT - WHEEL,  $S' = 1.33$

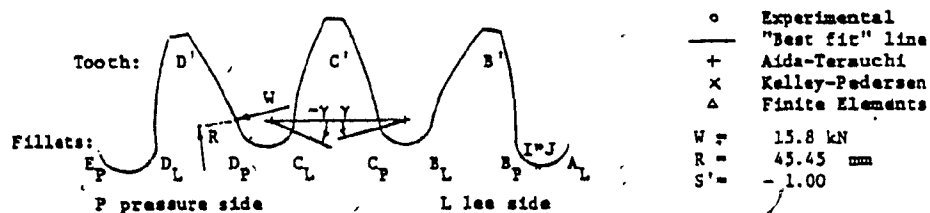
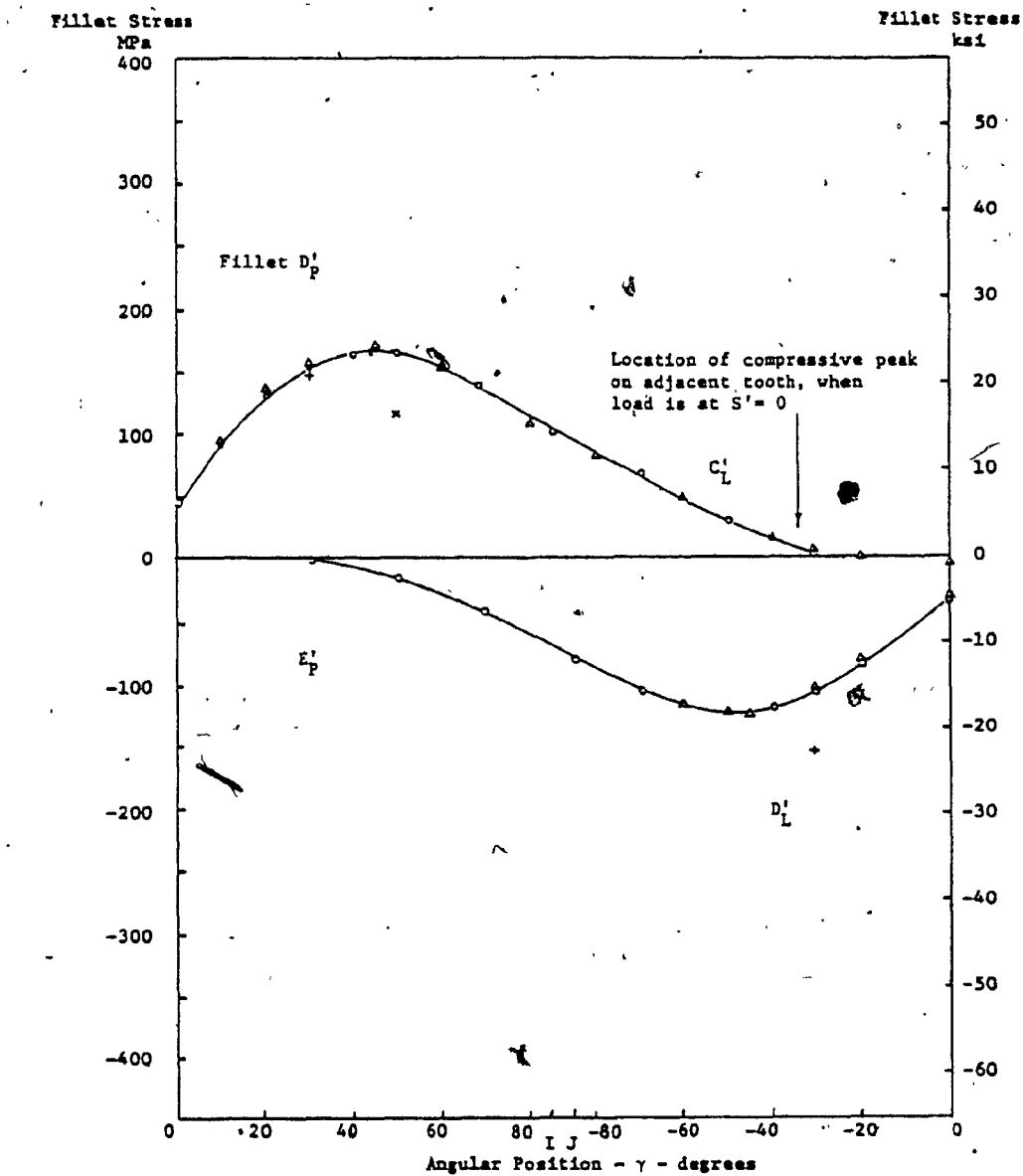


FIG. 7.4 FILLET STRESSES VS. ANGULAR POSITION, SINGLE ENGAGEMENT - PINION,  $S' = -1.00$

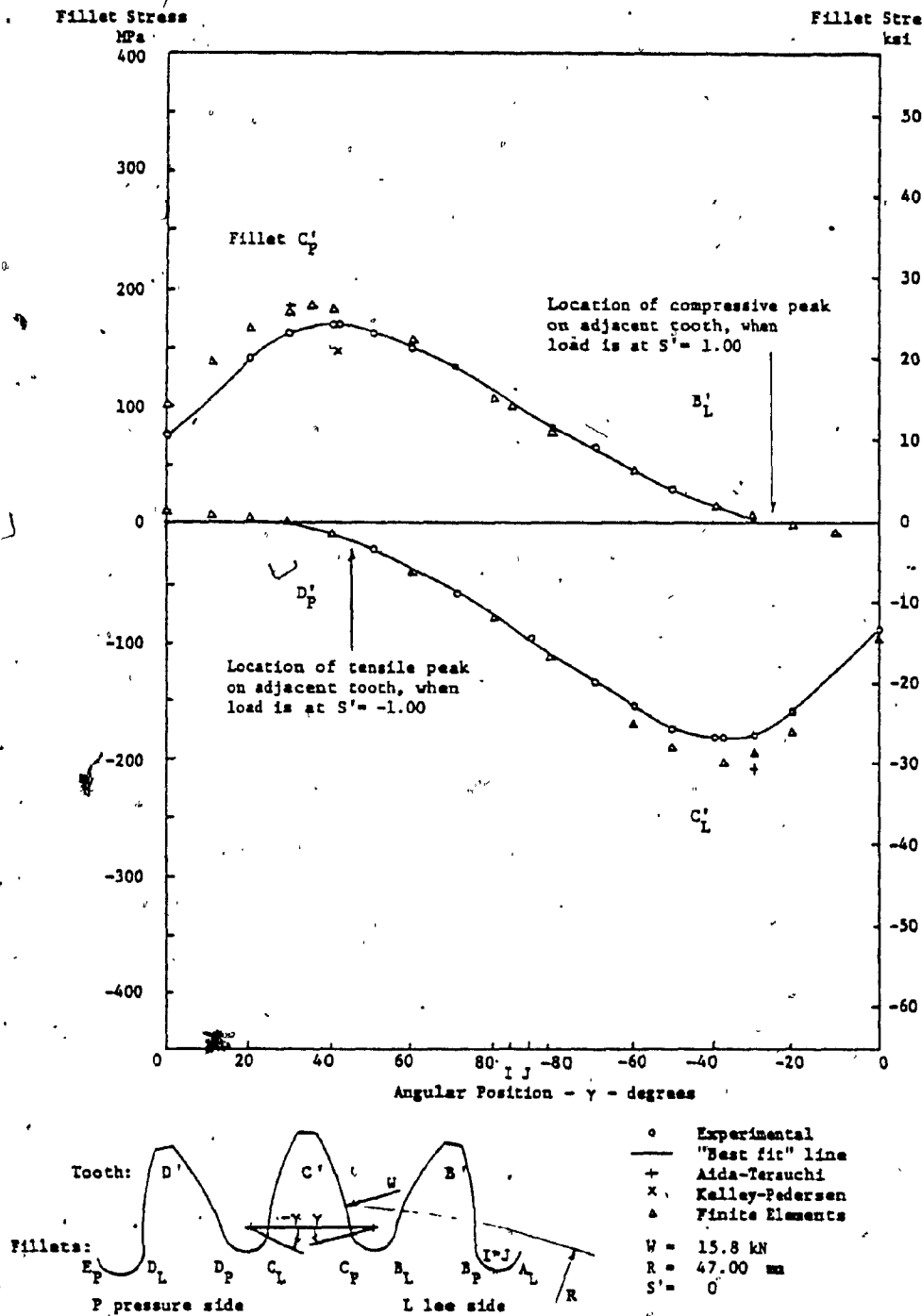


FIG. 7.5 FILLET STRESSES VS. ANGULAR POSITION,  
SINGLE ENGAGEMENT - PINION,  $S' = 0$

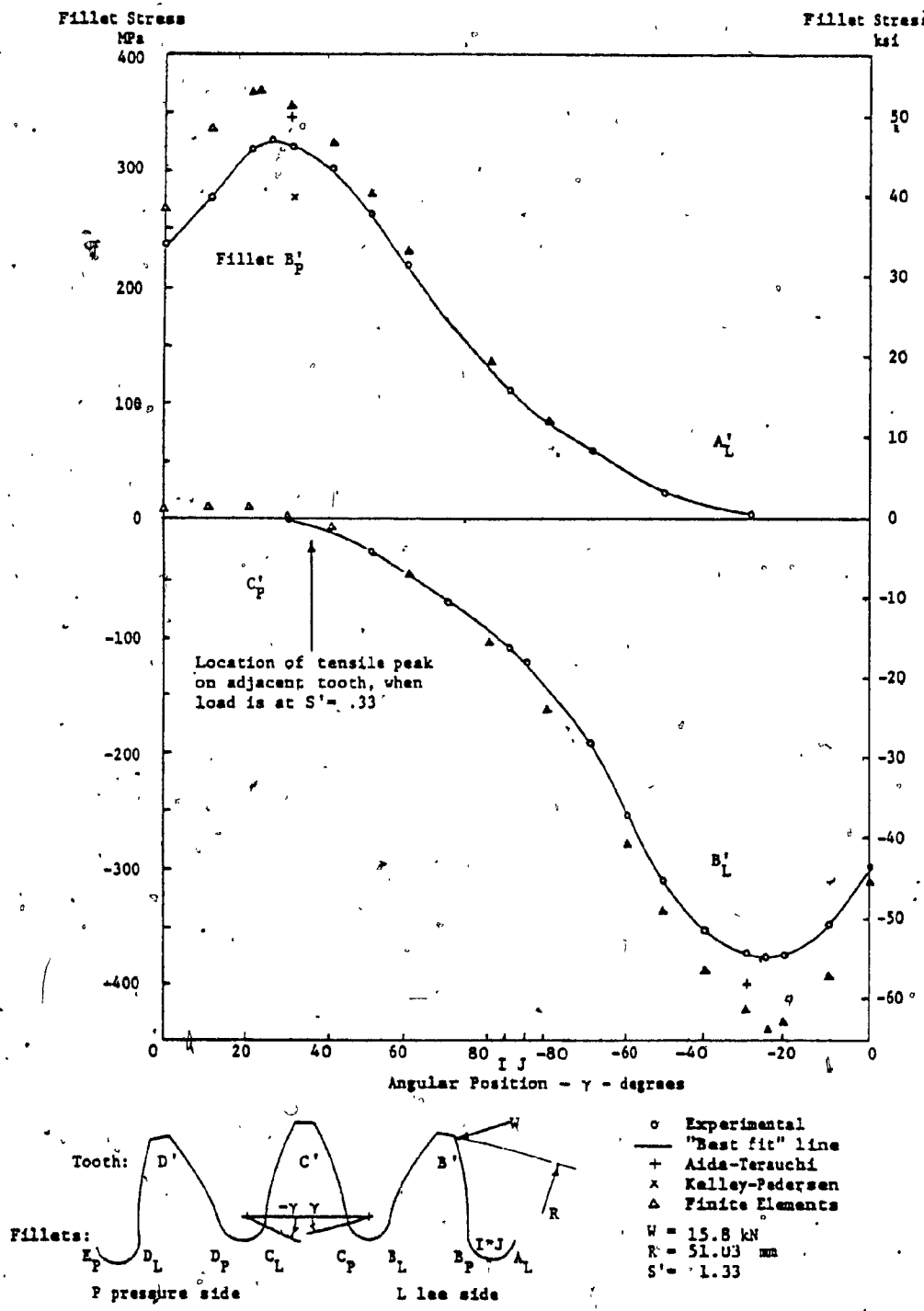


FIG. 7.6. FILLET STRESSES VS. ANGULAR POSITION, SINGLE ENGAGEMENT - PINION,  $S' = 1.33$



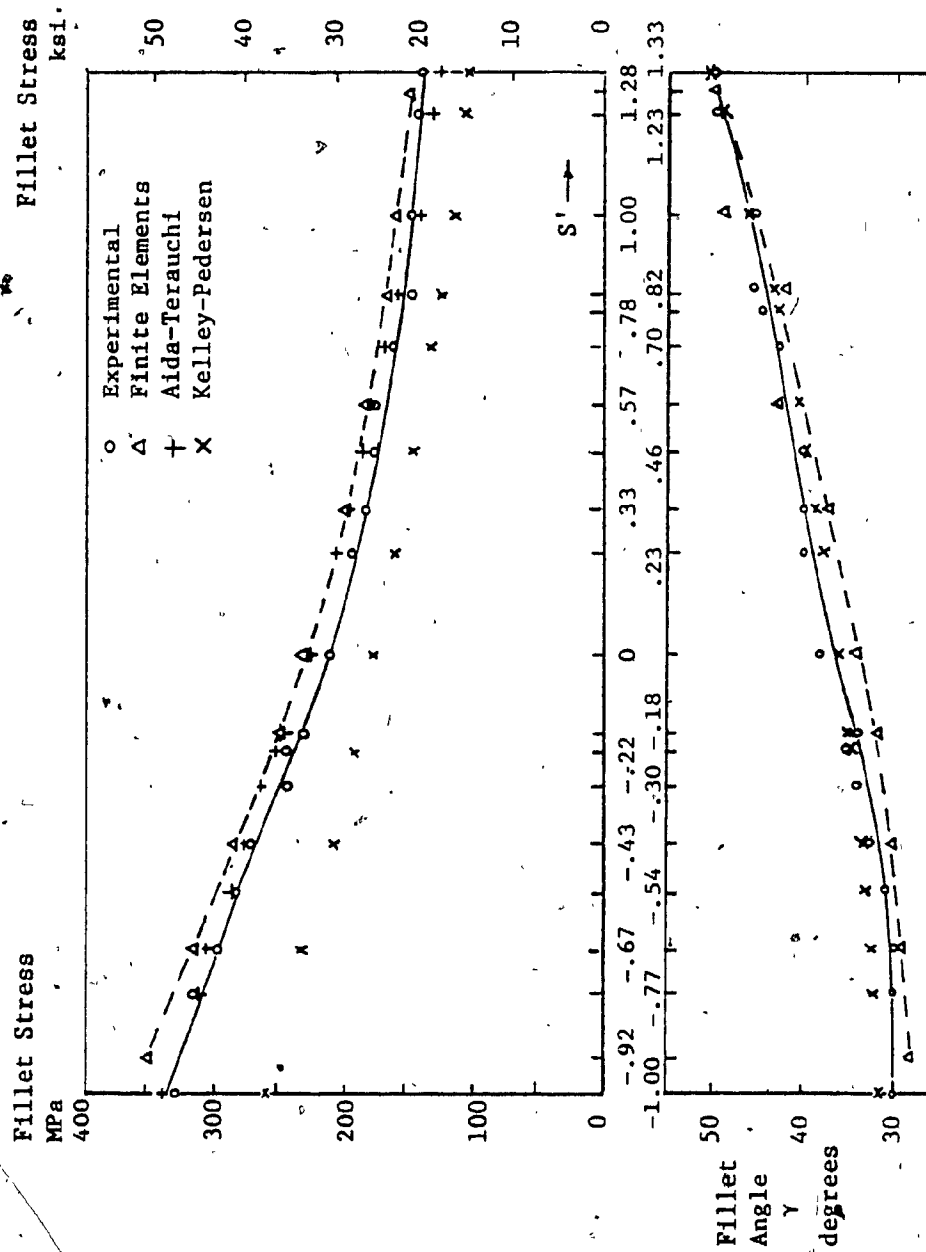


FIG. 7.7 PEAK TENSILE STRESSES AND THEIR ANGULAR LOCATION VS  $S'$  (NORMALIZED POSITION ALONG THE LINE OF ACTION)  
SINGLE ENGAGEMENT - WHEEL

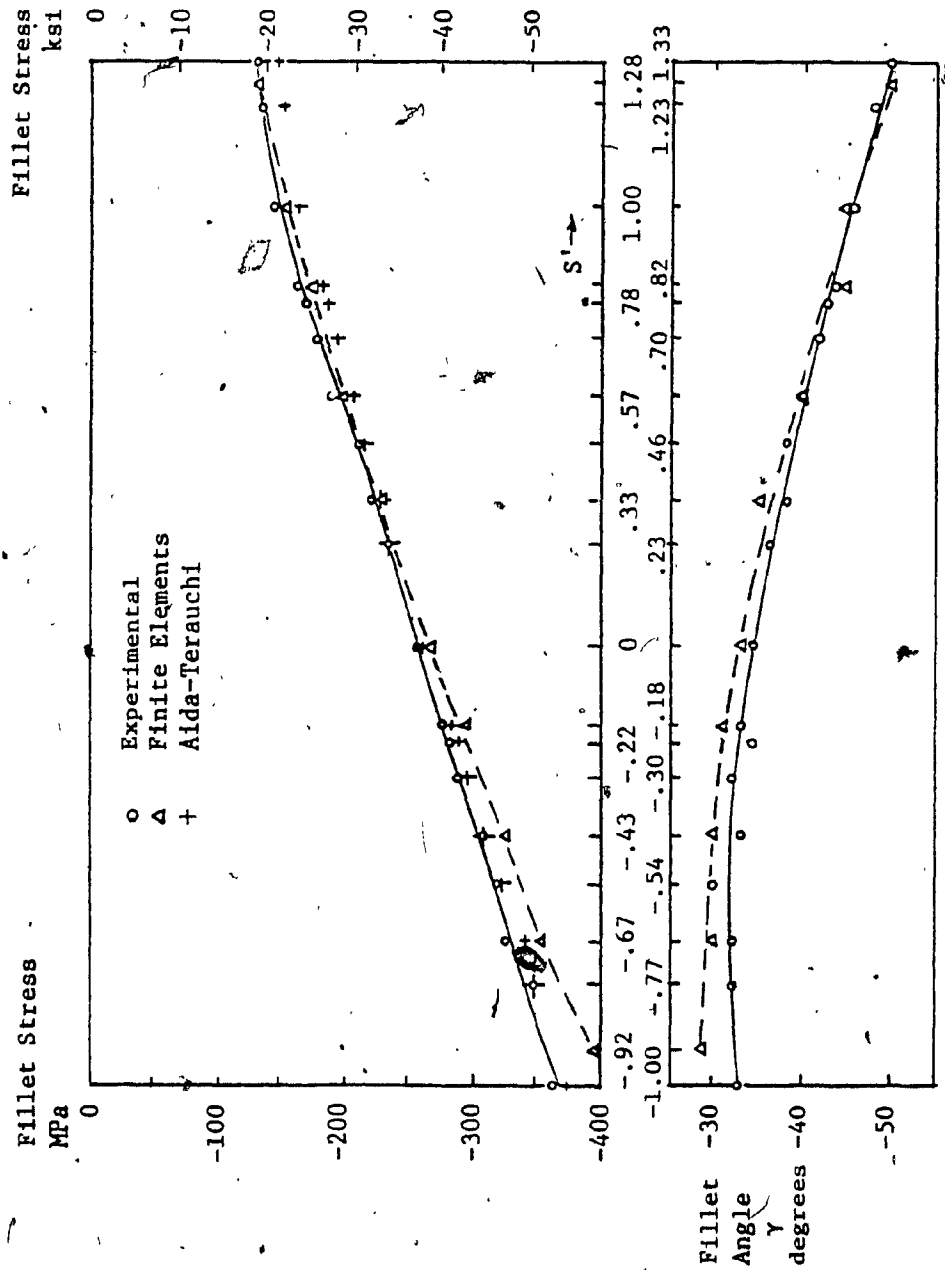


FIG. 7.8 PEAK COMPRESSIVE STRESSES AND THEIR ANGULAR LOCATION VS.  $S'$   
SINGLE ENGAGEMENT - WHEEL

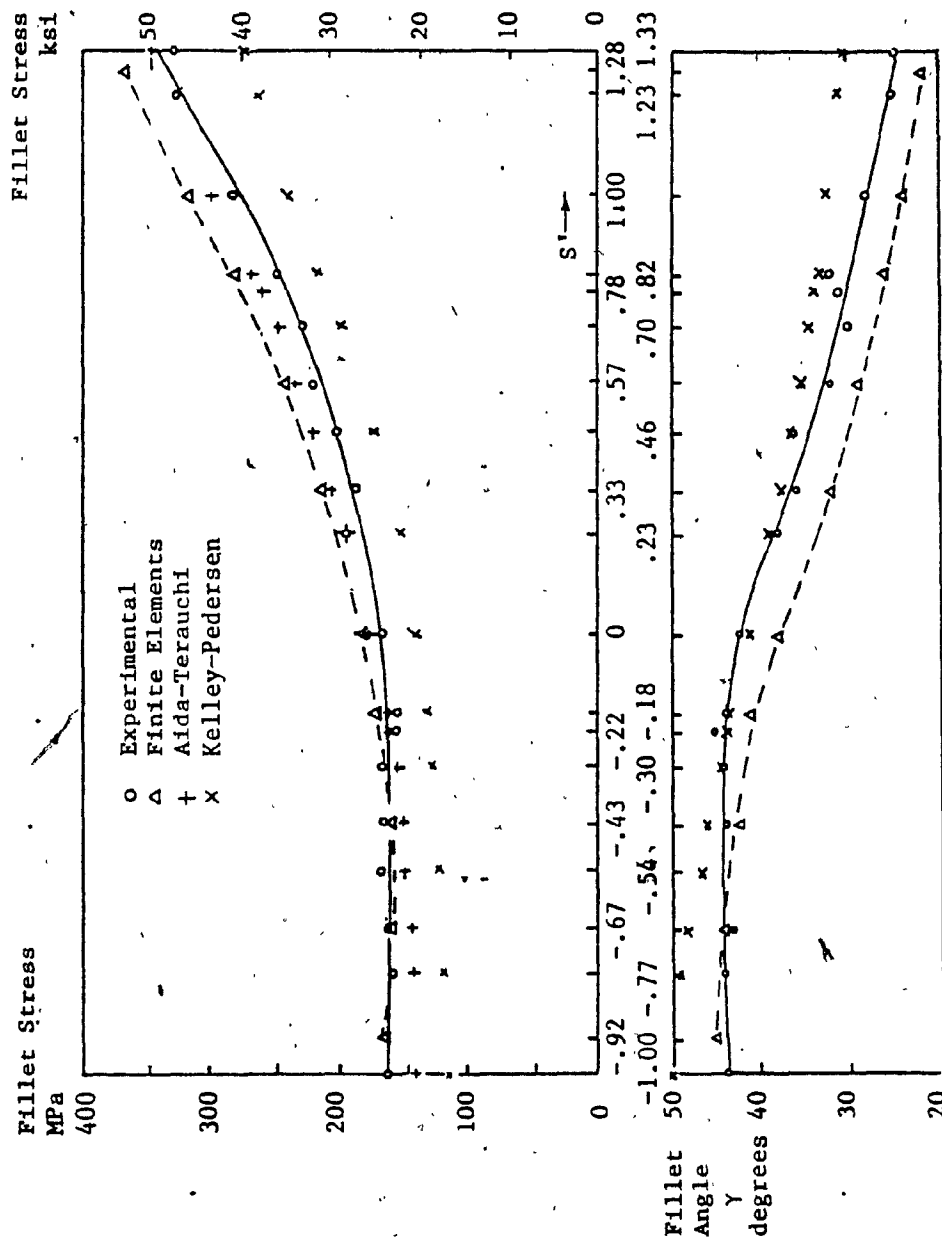


FIG. 7.9 PEAK TENSILE STRESSES AND THEIR ANGULAR LOCATION VS:  $S'$   
SINGLE ENGAGEMENT - PINION

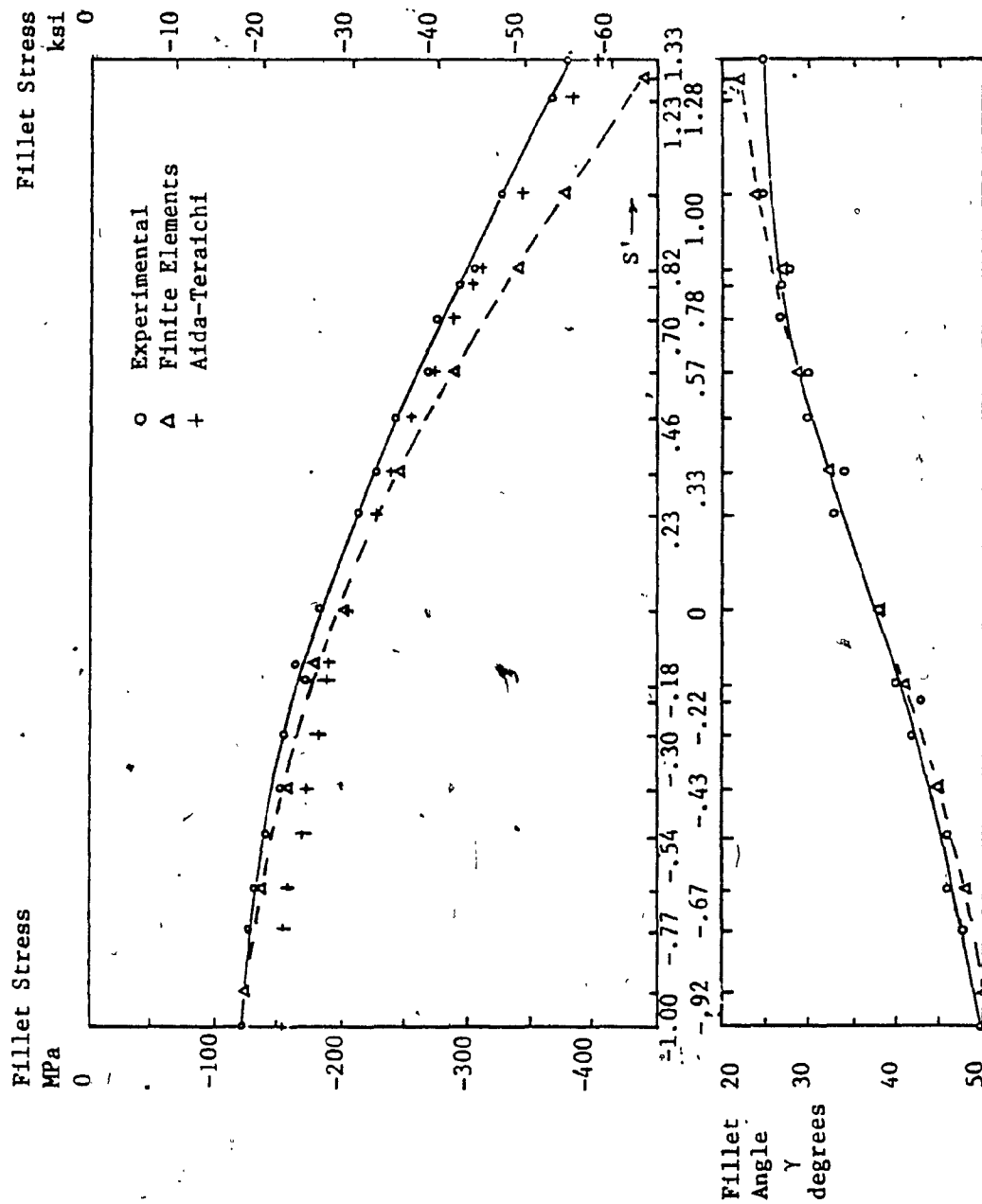


FIG. 7.10 PEAK COMPRESSIVE STRESSES AND THEIR ANGULAR LOCATION VS.  $S'$   
SINGLE ENGAGEMENT - PINION

As may be expected, the tensile and the compressive maxima increase in magnitude as the load moves toward the tip. The reversal of this trend for tensile stresses at low dedendum loading [19] may be observed for the pinion, but for the wheel, only the slope of the curve is reduced. Similarly as the load moves toward the tip the location of the peak climbs toward the flank, with some reversal at the dedendum.

On figures, which display the peaks, the stresses obtained from the photoelastic experiment are shown in full line. Those found on finite element analysis are connected with dashed lines. The stresses determined using the closed form equations appear as unattached points.

The locations, where the plotted stresses would superimpose on the peaks at the adjacent teeth as "direct cross effect of stresses" on an assumed multiple engagement, are indicated.

The finite element, photoelastic results and those obtained by using the Aida-Terauchi formula in general correlate well. The Kelley and Pedersen stresses appear to be under estimates, however their angular position fit the data neatly. The photoelastic peak stresses seem to fall behind the finite element maxima as the load approaches the tips. The maximum deviations for the tensile and compressive peaks are respectively 6% and 9% for the wheel, 11% and 16% for the pinion.

Friction at the contact may be partially responsible for these discrepancies. This subject is discussed in more detail in Para. 9.1.

Photograph Fig. (7.11) displays the isochromatic fringe pattern in black and white for a pair of teeth in single engagement. Six loading cases are shown. The crescent like fringes indicate the fillet stresses, the isotropic points and the contacts are clearly recognisable.

FIG. 7-11 PERMEABLE FRINGE PATTERN - SINGLE LINE

## 7.2 Stresses - Multiple Tooth Pair Engagement

Sample plots of fillet stresses vs angular position are shown in Fig's. (7.12 thru 7.17).  $S'_{nom}$  refers to the load on the central tooth "C". The insert on the graphs illustrates the location of the loads and the convention for the fillet angles. The experimentally determined loads and the radii of contacts are also shown in the boxes.

The fillets are identified by two letters. The first of these stands for the tooth to which the fillet belongs, the index letter P or L refers to pressure or lee sides respectively. The finite element results are represented only by the peak values. These points are left unattached, they are identified where they may be ambiguous.

The highest stresses appear when only two pairs of teeth are engaged simultaneously. The magnitudes of the compressive stresses in general exceed those of the tensile stresses. The cross effect of the loads on the adjacent teeth appreciably modifies the stress distribution. This is most apparent at the fillet bottom between two loaded teeth, where the tensile field due to one load and the compressive stresses owing to the other one are mutually reduced. The dominant influence on each peak stress is still the load on the tooth to which the fillet belongs, the cross effect here is small.

The maxima were plotted vs position along the line of action in Fig's. (7.18) and (7.19). The experimental, finite element and dynamic program results and those which were calculated from "Stress Admittances" (Para.8.4), all correlate well. The latter is based on data obtained from single engagement stress and deflection measurements, and gave an average deviation of 6%. This value may be used as a rough

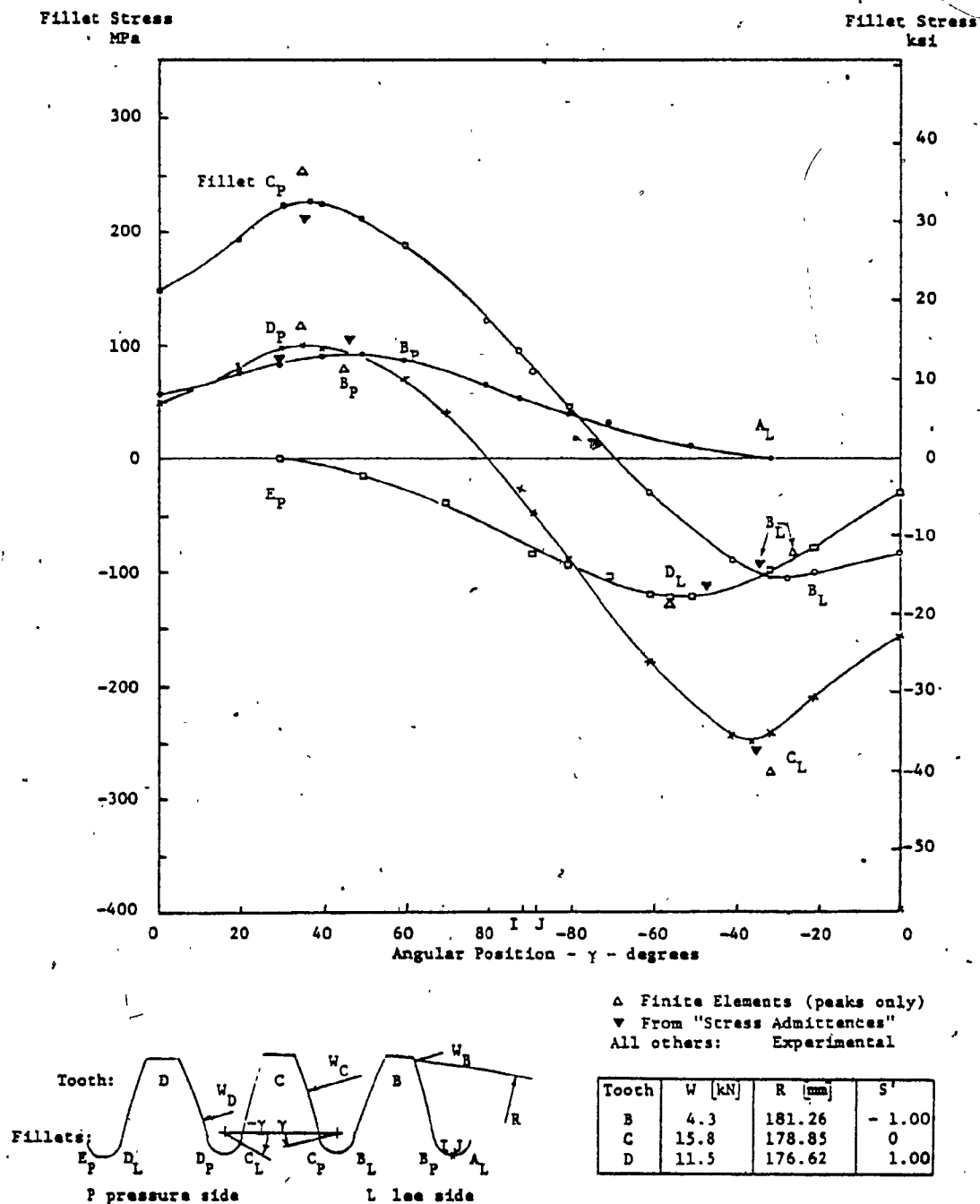


FIG. 7.12 FILLET STRESSES VS. ANGULAR POSITION,  
MULTIPLE ENGAGEMENT - WHEEL,  $S'_{nom} = 0$



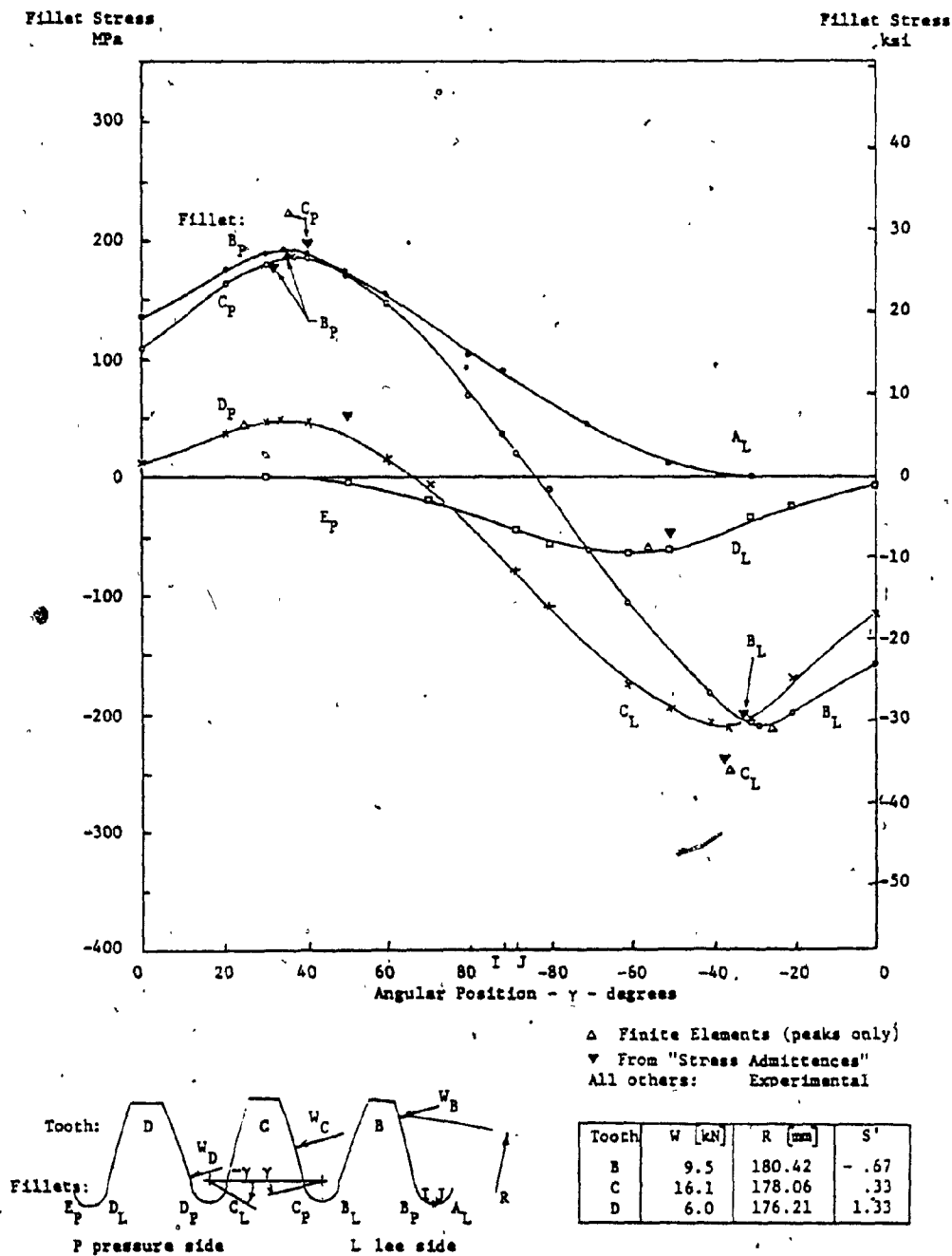
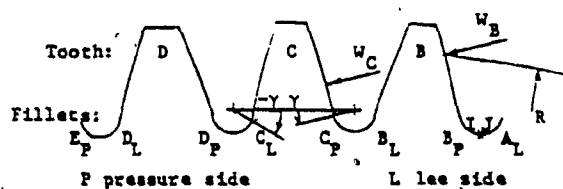
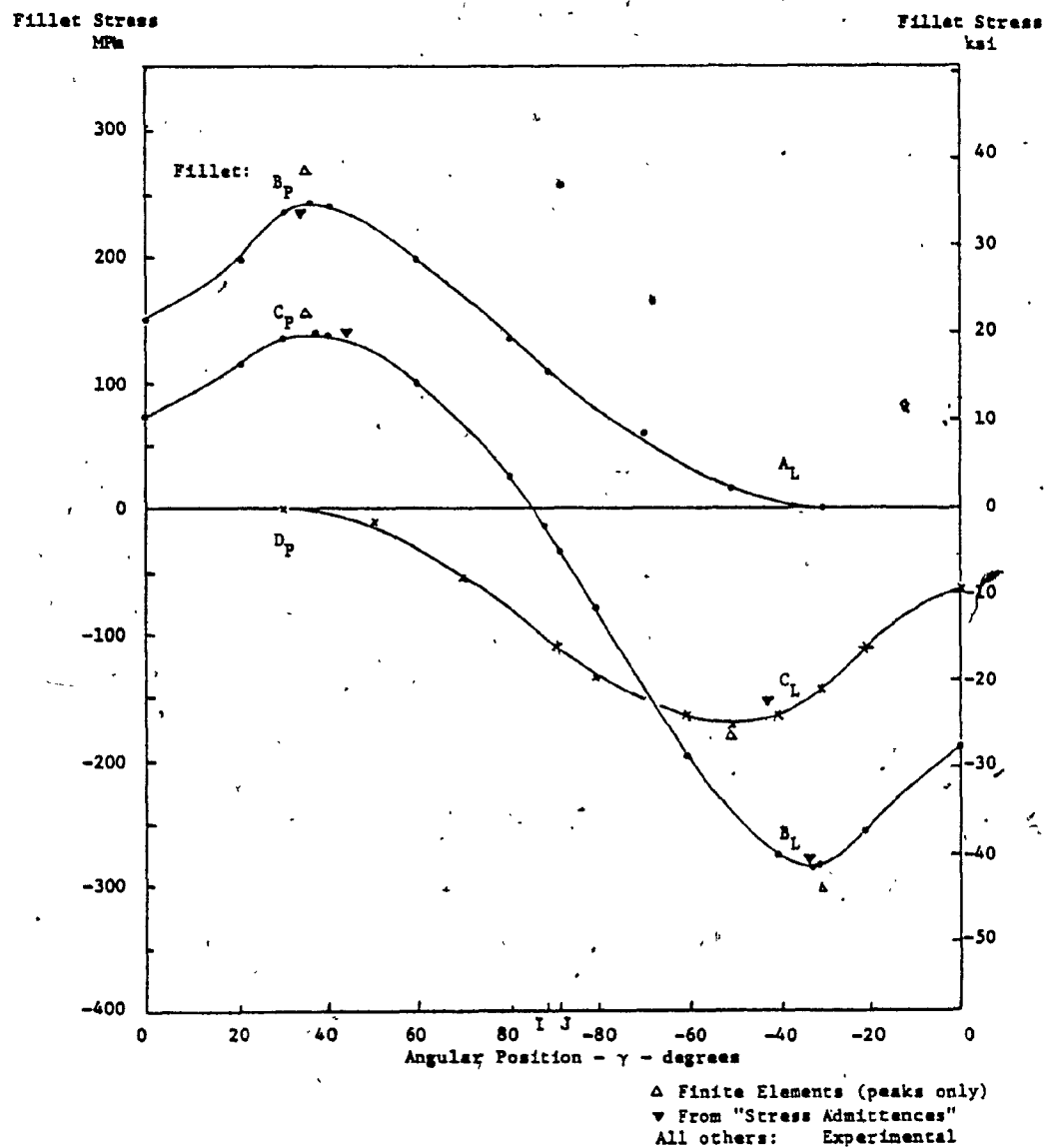


FIG. 7.13 FILLET STRESSES VS. ANGULAR POSITION,  
 MULTIPLE ENGAGEMENT - WHEEL,  $S'_{nom} = .33$



Tooth	W [kN]	R [mm]	S'
B	16.2	179.24	-.18
C	15.4	177.04	.82

FIG. 7.14 FILLET STRESSES VS. ANGULAR POSITION,  
 MULTIPLE ENGAGEMENT - WHEEL,  $S'_{nom} = .82$

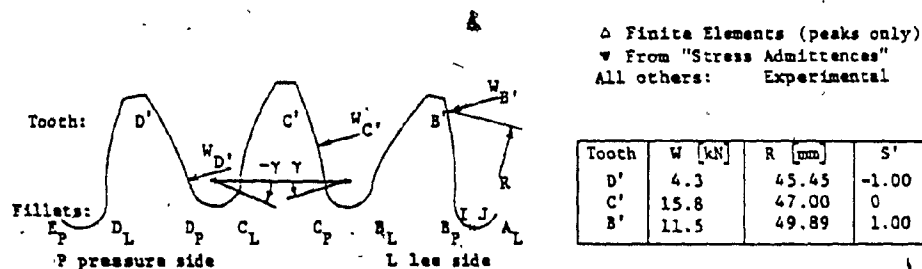
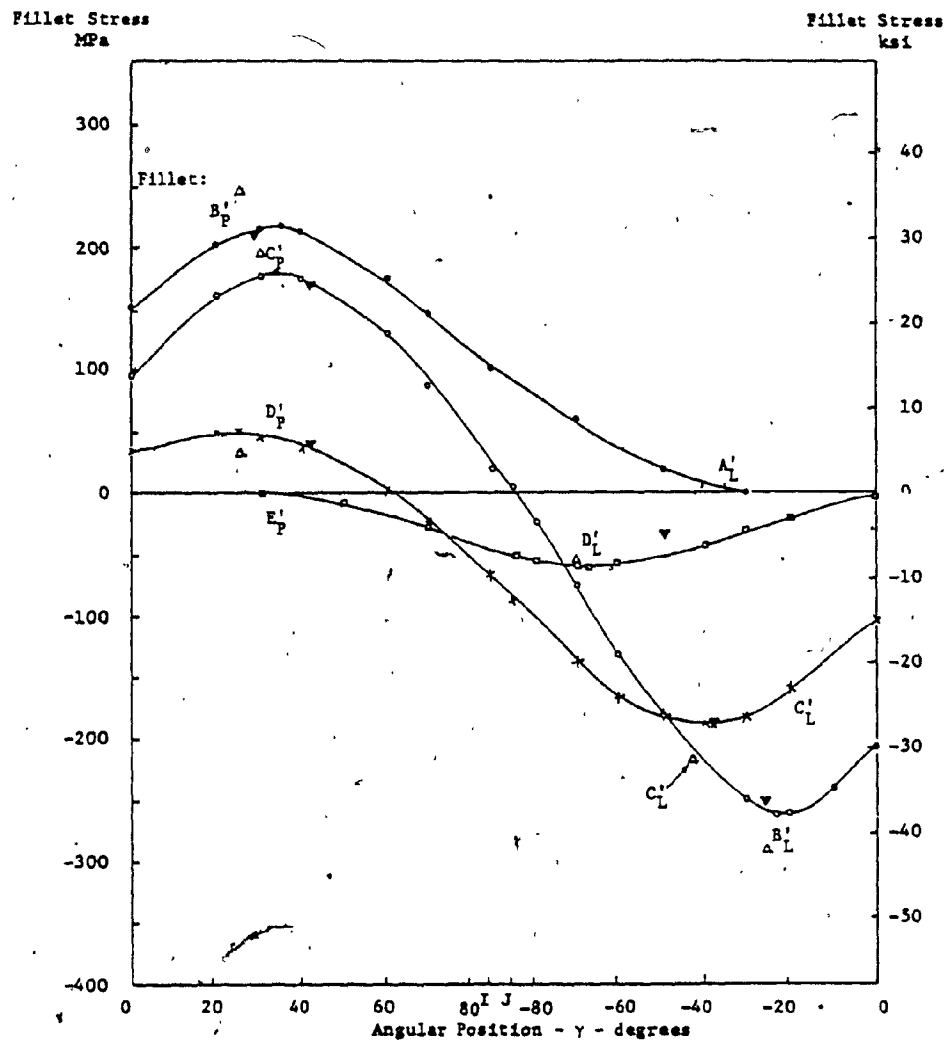
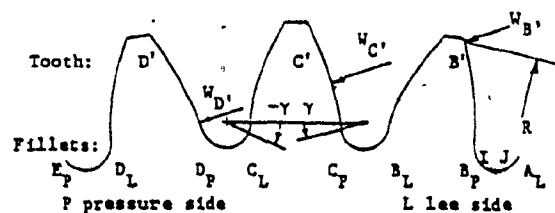
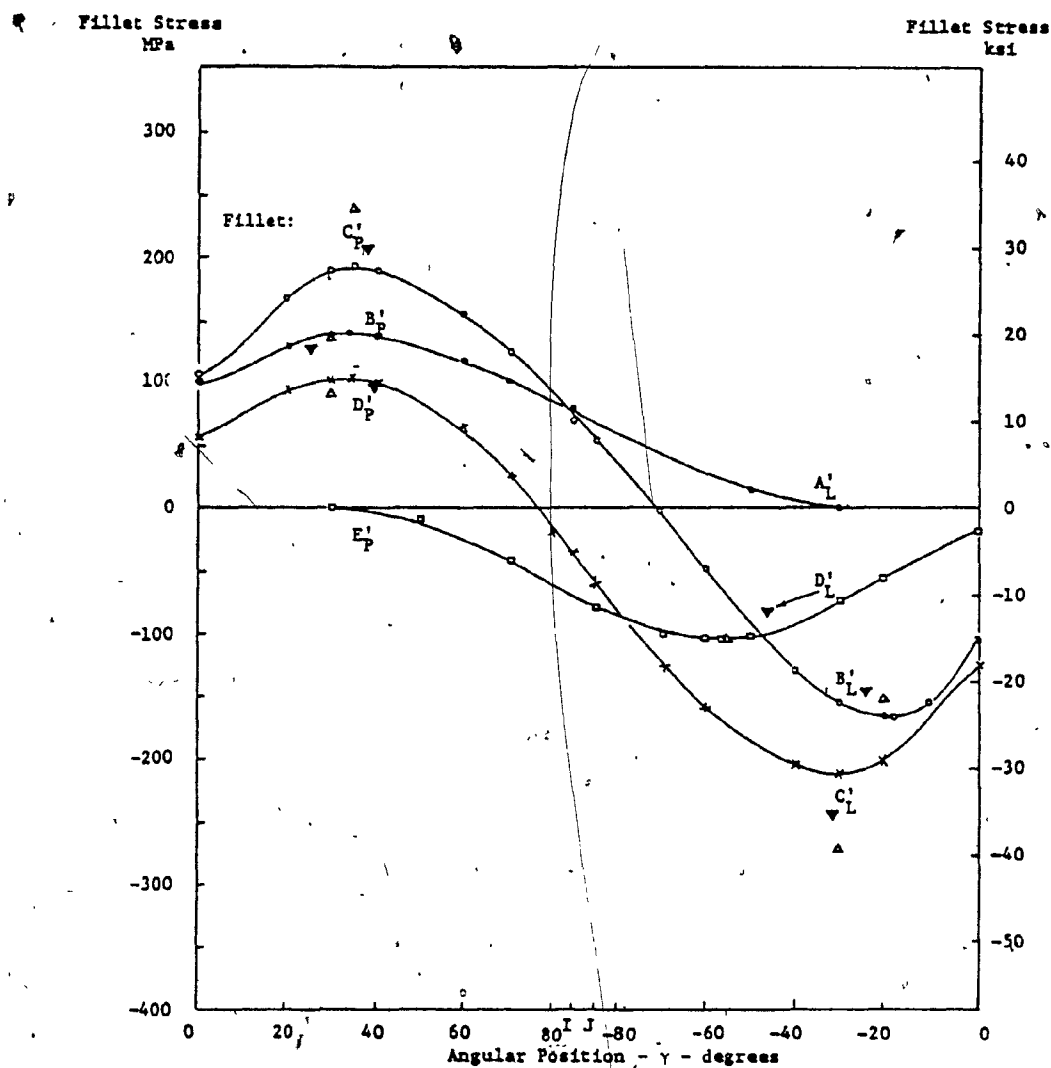


FIG. 7.15 FILLET STRESSES VS. ANGULAR POSITION, MULTIPLE ENGAGEMENT - PINION,  $S'_{nom} = 0$



△ Finite Elements (peaks only)  
 ▼ From "Stress Admittances"  
 All others: Experimental

Tooth	W [kN]	R [mm]	S'
D'	9.5	45.69	-.67
C'	16.1	47.77	.33
B'	6.0	51.03	1.33

FIG. 7.16 FILLET STRESSES VS. ANGULAR POSITION,  
 MULTIPLE ENGAGEMENT - PINION,  $S'_{nom} = .33$

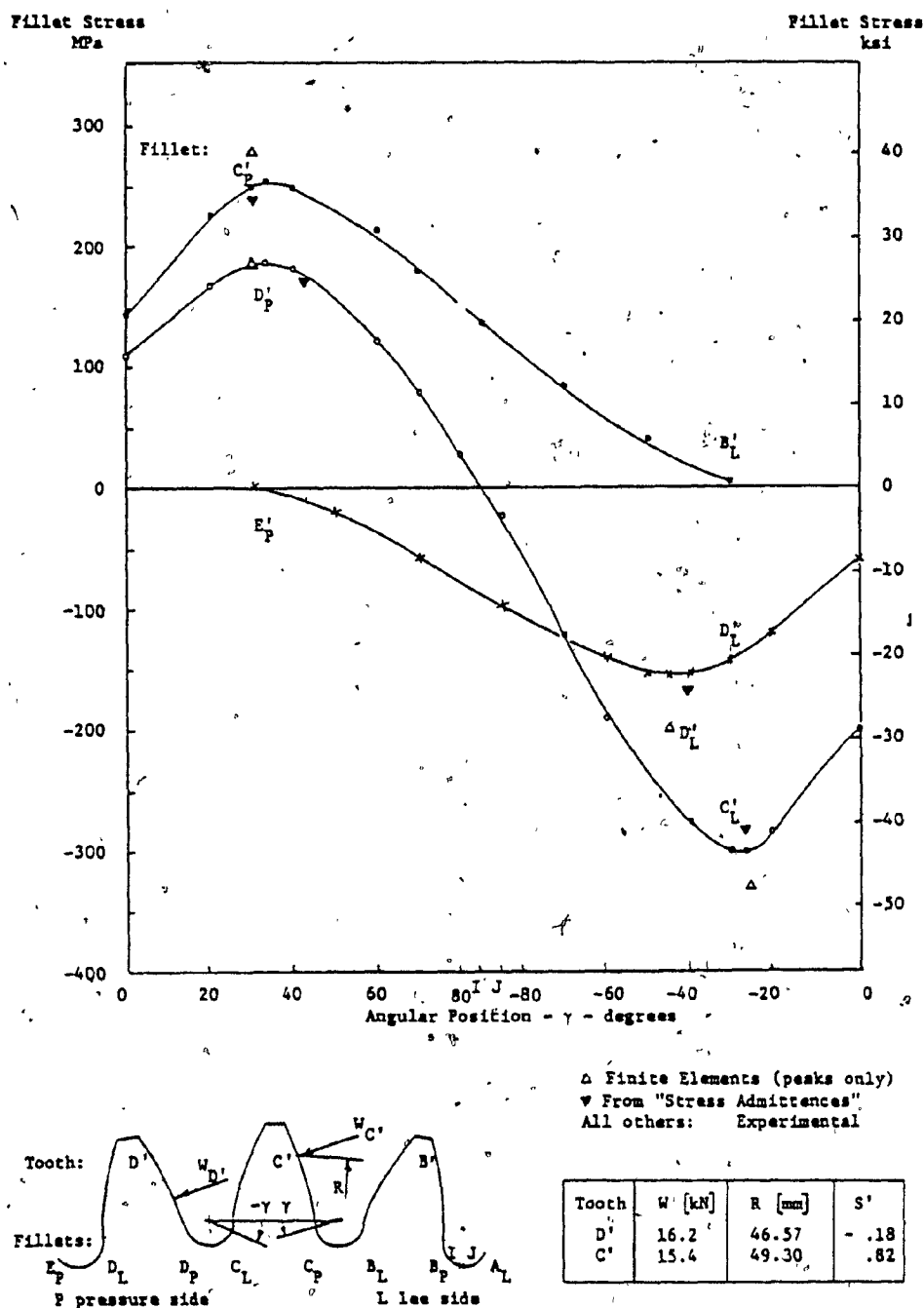


FIG. 7.17 FILLET STRESSES VS. ANGULAR POSITION,  
MULTIPLE ENGAGEMENT - PINION,  $S'_{nom} = .82$

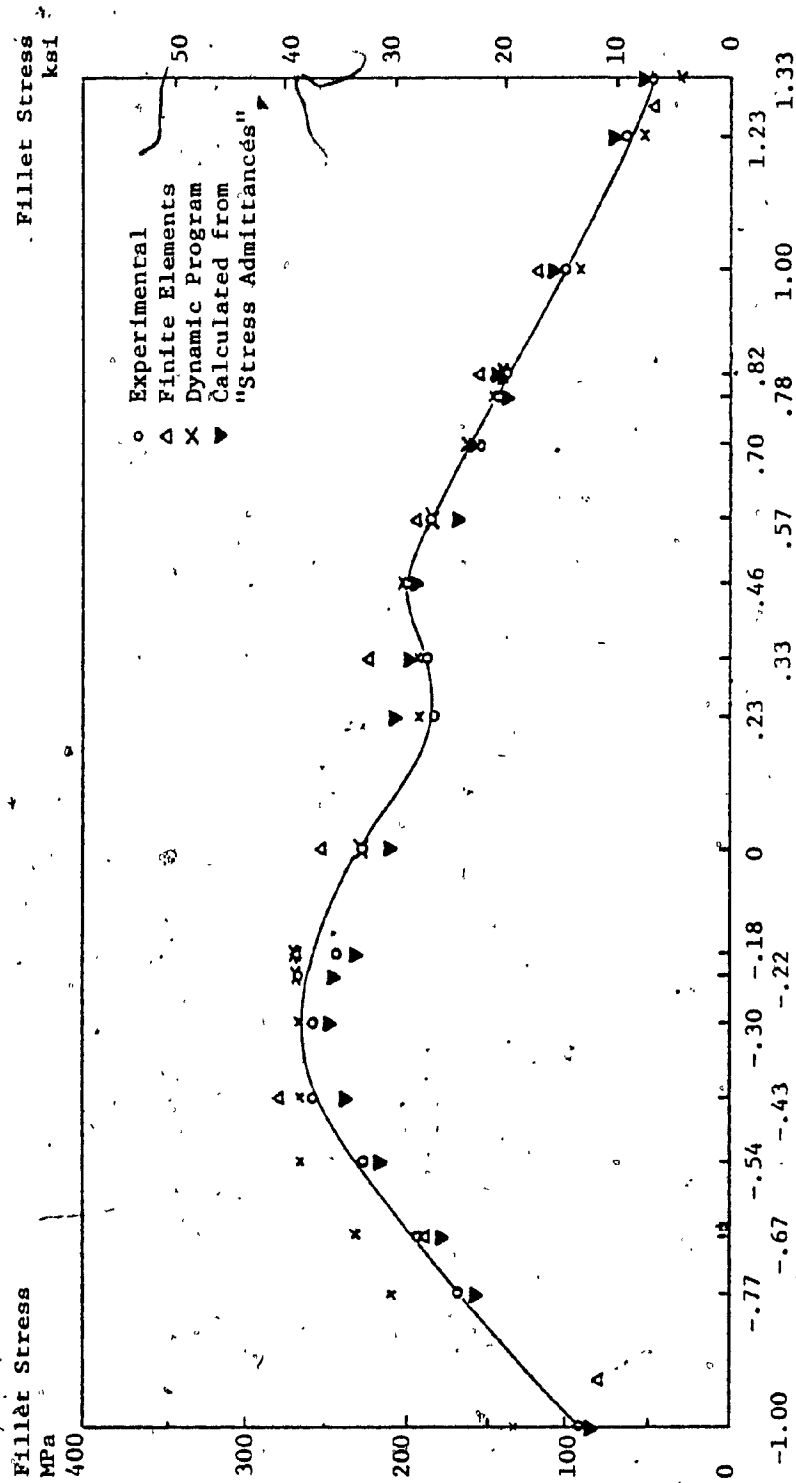


FIG. 7.18 PEAK TENSILE STRESSES VS  $S'$  - MULTIPLE ENGAGEMENT - WHEEL

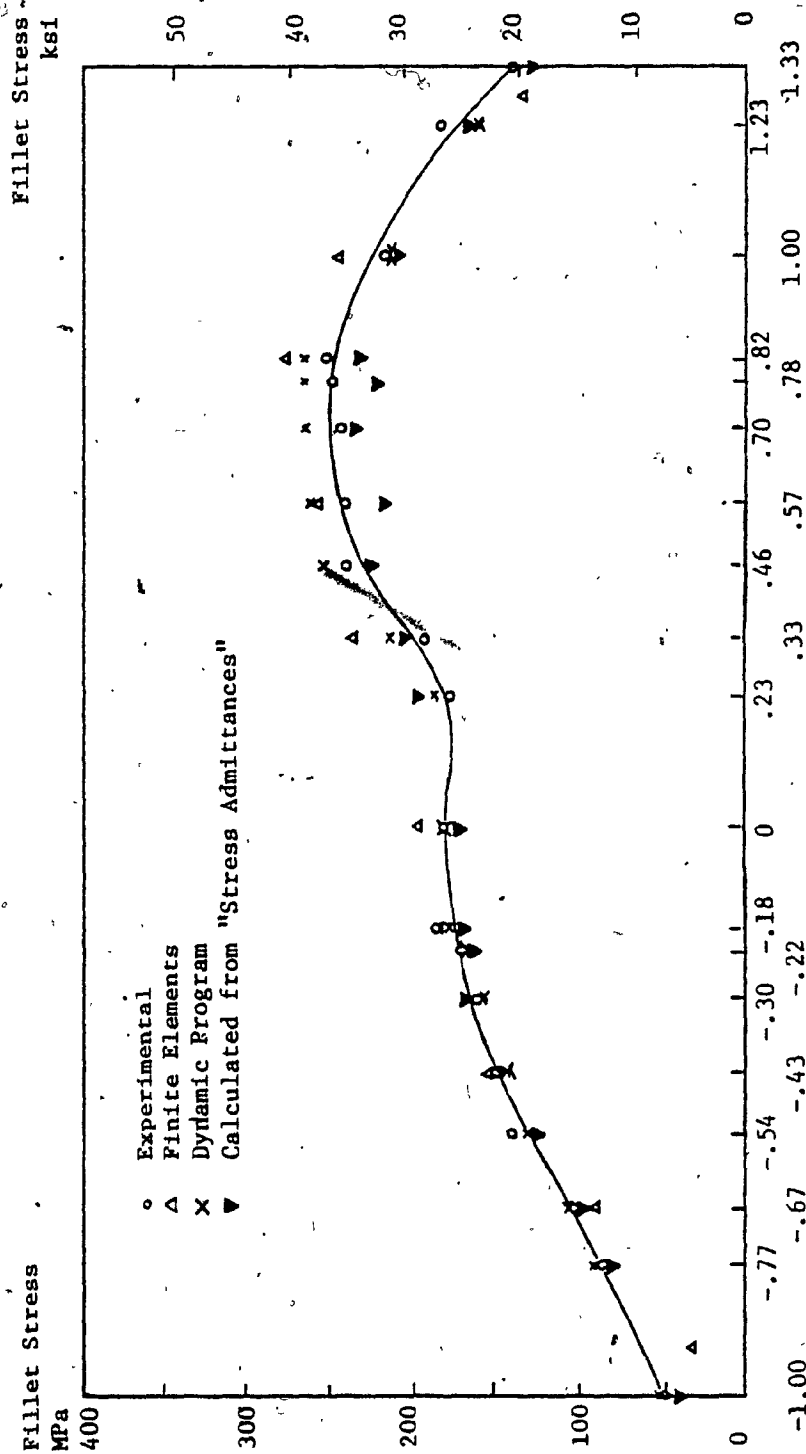
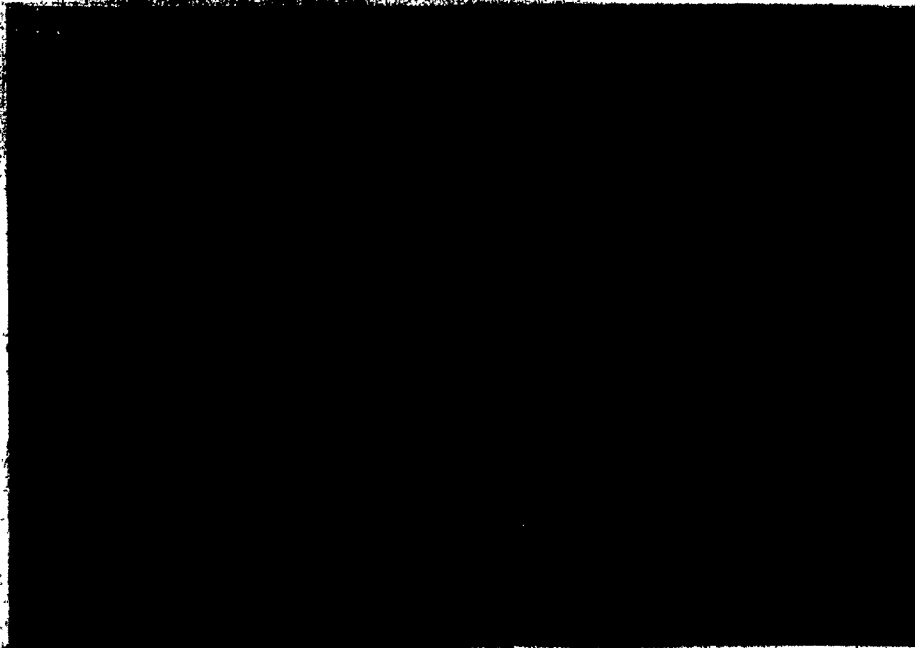


FIG. 7.19 PEAK TENSILE STRESSES VS S' - MULTIPLE ENGAGEMENT - PINION



S' nom - .23



S' nom - .43

FIG. 7.20 PHOTOELASTIC FRINGE PATTERN - MULTIPLE PAIR ENGAGEMENT



estimate of the cross effect of stresses at the location of the peaks.

Photographs on the preceding page (Fig. 7.20) are samples of fringe patterns obtained on multiple tooth pair engagement tests. The double crescents indicate peaks of opposite signs on each side of the fillet.

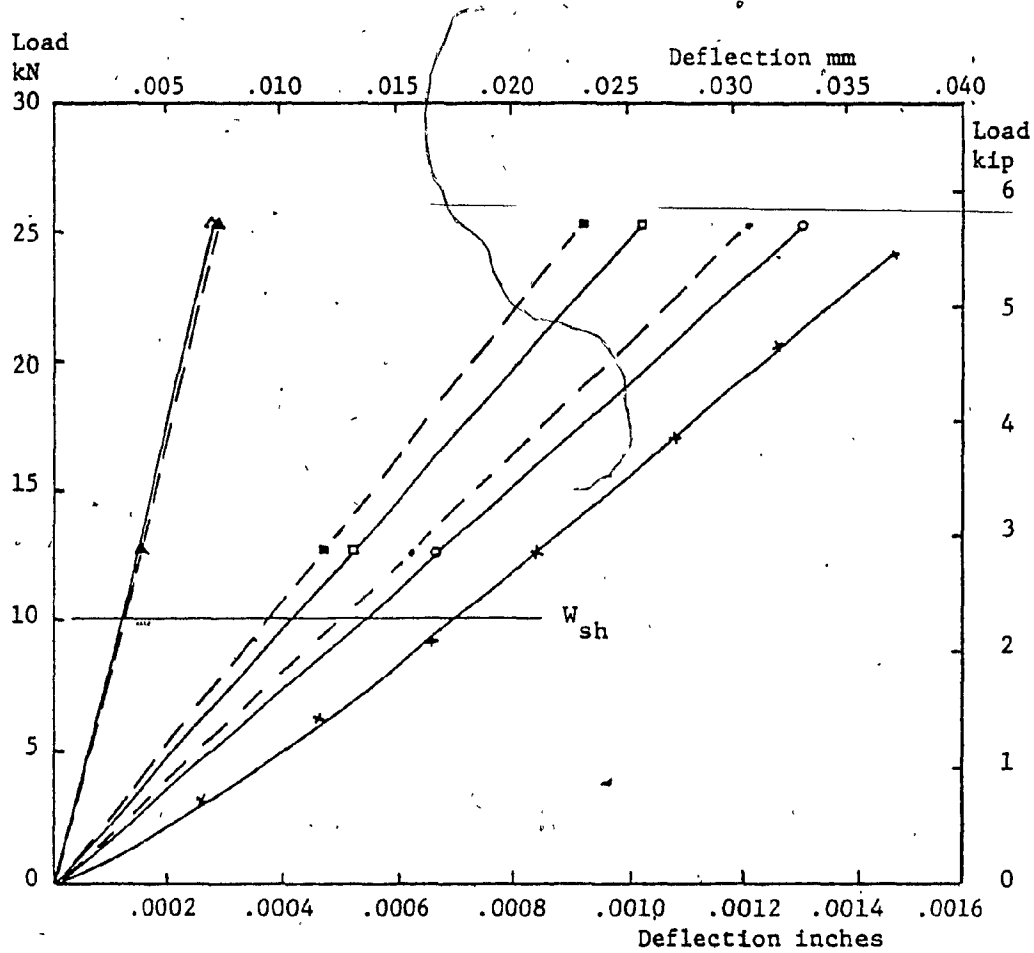
### 7.3 Deflections

Samples of load vs deflection curves are shown in Fig's. (7.21), (7.22) and (7.23). The "relative" deflections are shown with full lines. The "absolute" data are given in dashed lines.

By employing the finite element method it was possible to obtain the deflections for the pinion and for the wheel individually. They were plotted separately, then their sum curve, which represents the deflections of a pair, was added to each graph.

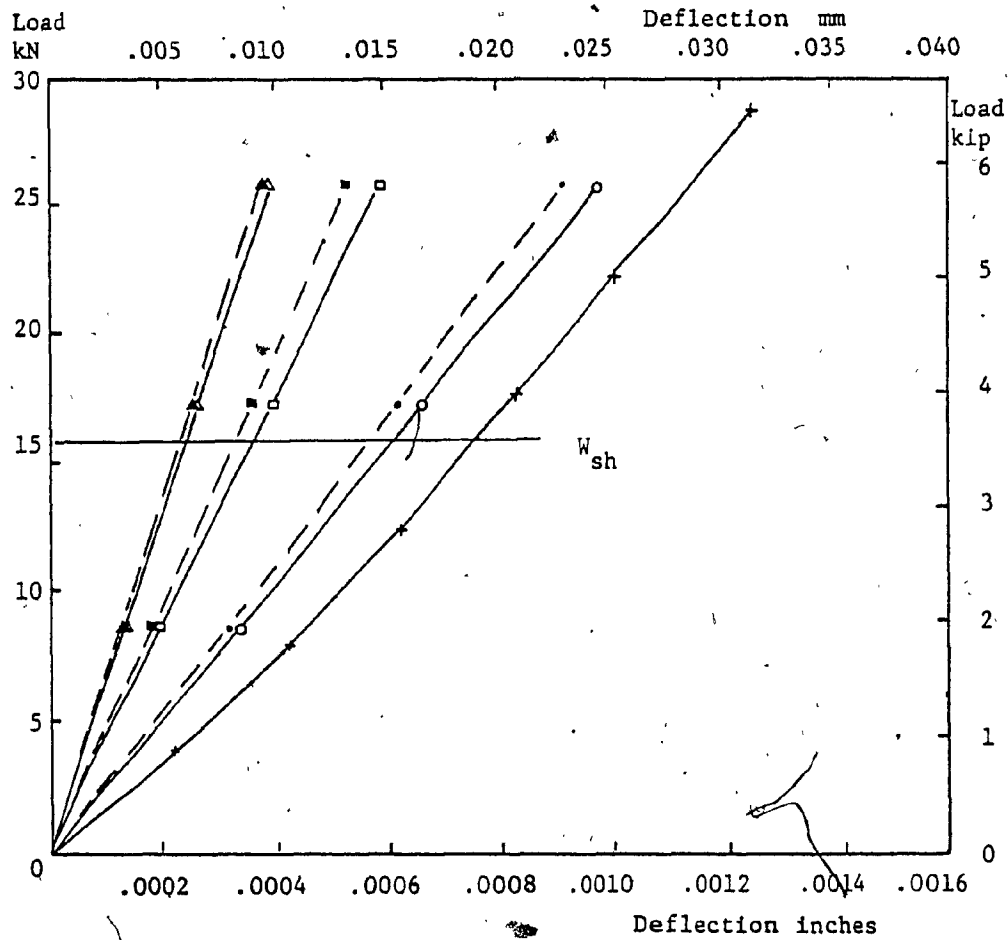
The experimental measurements which yielded relative pair deflection directly, are also included. A line indicating the "shared" load level was added at which the compliances were later evaluated.

Weber [29] and Cornell [8] suggest by Eq's. (2.29), (2.31) & (2.44) that these curves are non linear. The finite element results indicate that this affect is very slight. The measurements on the photoelastic model display a more pronounced deviation from linearity. The plastic model appears to be markedly more flexible at lower loads than the finite element model. As the loads increase the curves tend to become parallel, thus the non-linear action on the photoelastic model happens at light loadings. Geometric imperfections at the contact may be partially responsible for this discrepancy, though the reason for this behaviour is not yet clear.



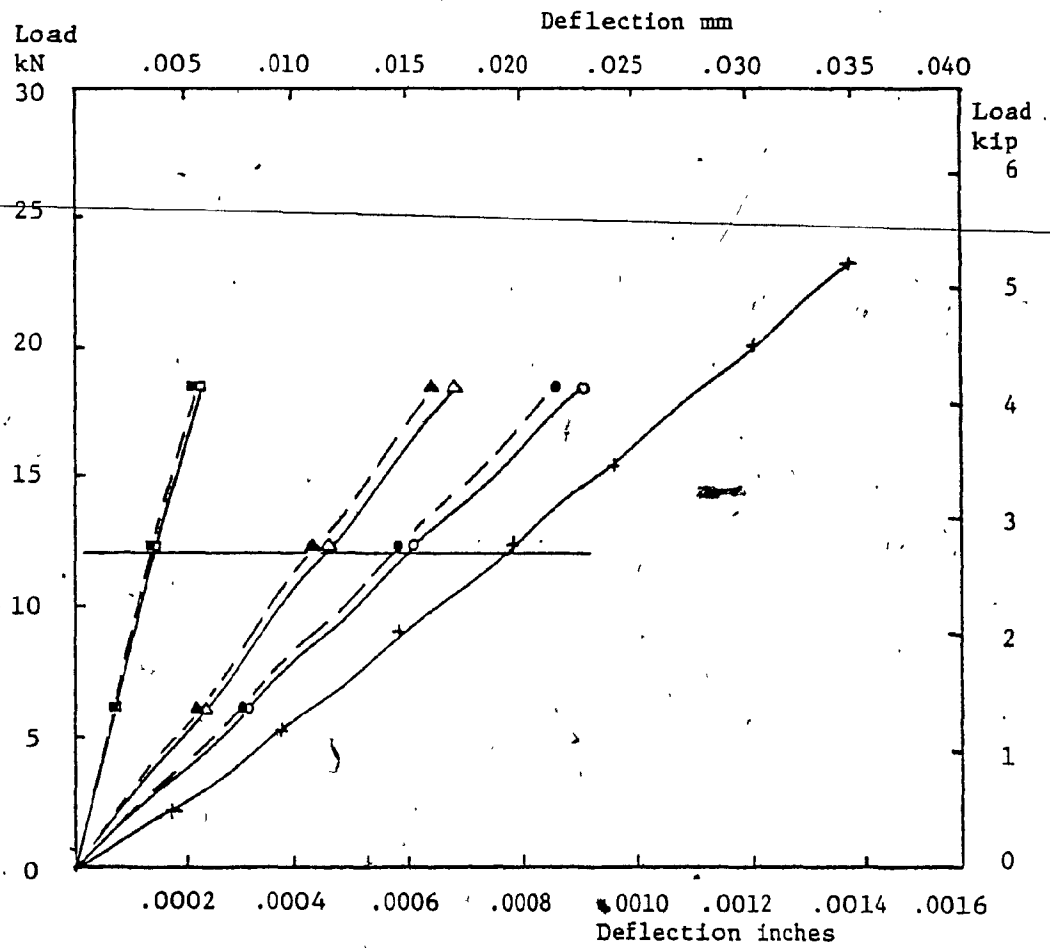
	Finite Elements		Experimental
	Absolute	Relative	
Wheel	■	□	
Pinion	▲	△	
Pair	●	○	×

FIG. 7.21 DEFLECTION VS LOAD,  $S' = -.67$



	Finite Elements		Experimental
	Absolute	Relative	Relative
Wheel	■	□	
Pinion	▲	△	
Pair	●	○	×

FIG. 7.22 DEFLECTION VS LOAD,  $S' = 0$

FIG. 7.23 DEFLECTION VS LOAD,  $S' = 1.00$

ANALYSIS OF RESULTS

From the stresses and displacements obtained from the experiments and finite element analysis, the pair-compliance, the sharing of the load, the "Stress Admittance" and the "Equivalent Static Alternating Stresses" will be calculated in the following.

8.1 Pair Compliance - Experimental

The compliance by definition is the ratio of deflection over load (Eq. 3.5). In the experiment relative deflections were measured, dividing them by the load "relative compliances" are obtained.

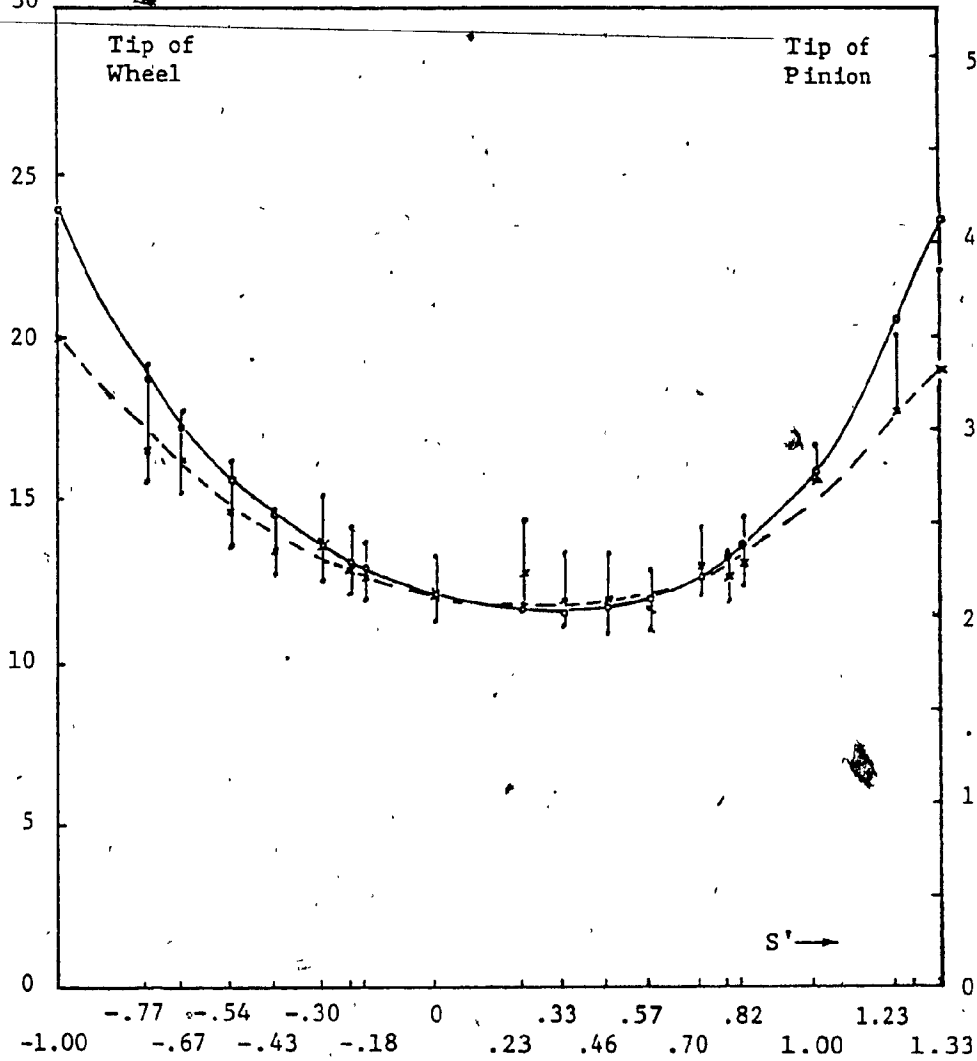
It was shown in ref's. [8] and [9] that the deflections are substantially non-linear with respect to the position of the load. Eq's. (2.31) and (2.29) and test results indicate, finite element results to a lesser degree, that they are also slightly non linear with respect to the magnitude of the load. Based on the experimental data a single value cannot describe the flexibility of a pair of teeth at a given contact point.

The compliances in the experiment were evaluated at arbitrary load levels of 25, 50 and 75% of "full test load" as shown in Fig. (8.1). A "best fit" dashed line was drawn through the 50% points. The 25 and 75% values are connected with vertical bars, giving a measure of the non-linearity corresponding to each load deflection curve. After the problem of load sharing has been settled, the experimental compliances were reevaluated at the levels they were shared in the multiple engagement tests. Their "best fit" curve is shown in full line.

At  $S' = .23$  an odd point appears. Based on the adjacent data it seems, that two slightly different curves may intersect at this point.

Compliance  
mm/N  
 $\times 10^{-7}$   
30

Compliance  
in/lbs  
 $\times 10^{-7}$   
5



Compliance evaluated at:

- 25
- x --- 50 % of 31.6 kN full test load
- 75
- o — "sharing" load levels (Best fit line shown)

FIG. 8.1 COMPLIANCE VS S' - EXPERIMENTAL

The test records indicate, that from  $S' = -1.0$  to  $.23$  the closing of the gap was observed at contact sites lying to the right of the loaded pair ( $S'$  increasing) whereas from  $S' = .33$  to  $1.33$  it was done from the opposite side. It is reasonable to expect that the two loading sites on the adjacent teeth due to a load on a middle tooth would not deflect in exactly the same manner.

Hence in cases of triple contact the relative compliances are ambiguous. However the differences are small and a fair average value may be obtained by curve fitting.

## 8.2 Compliances from Finite Elements, Correlation of Results

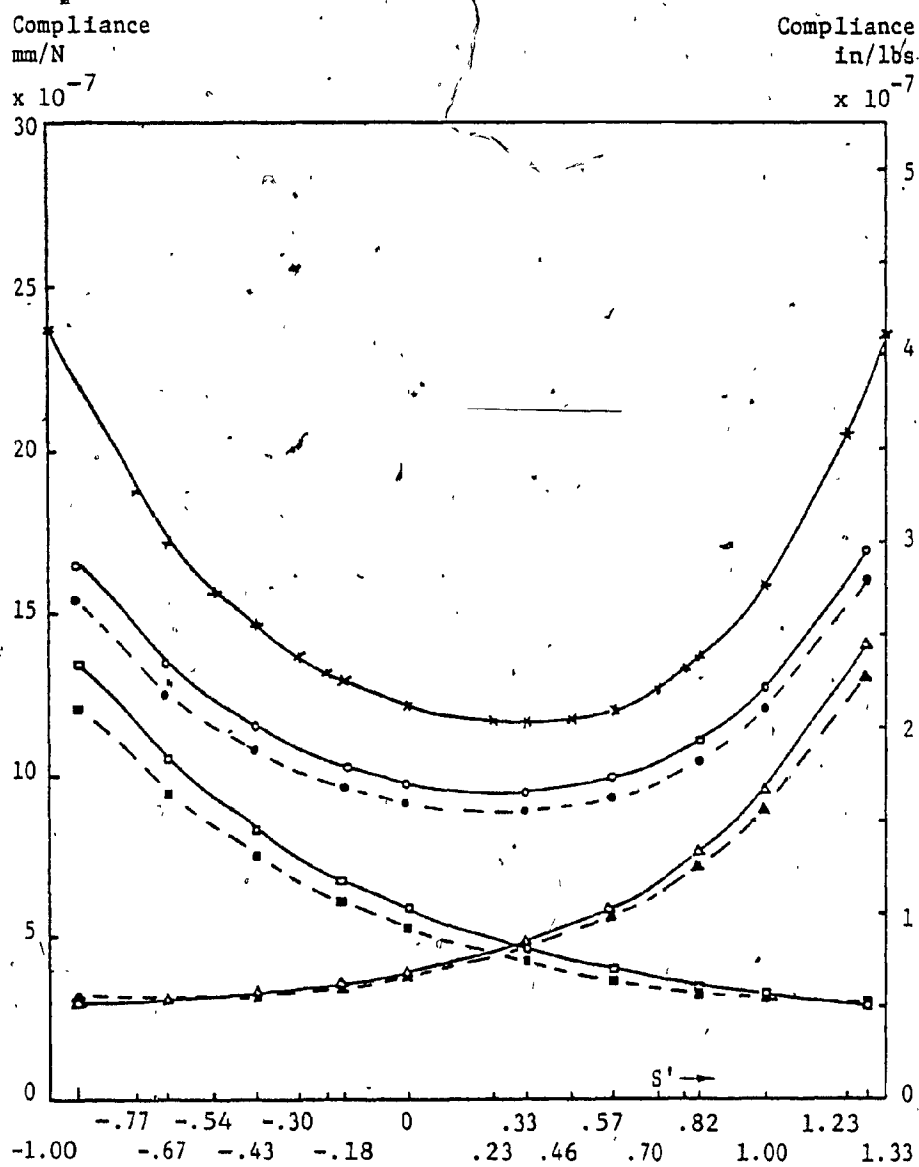
The finite element compliances were evaluated at the experimental "sharing loads", and are shown in Fig. (8.2). The "absolute" pair compliances (dashed line) will serve to correlate data from the preprocessor of the Cornell-Westervelt dynamic program, which will be available at a later date.

The "relative" and "absolute" pair compliances are nearly parallel, suggesting that either set leads to almost identical load sharing. The relative values exceed the latter by approximately 7%.

The deviation of relative compliances due to shifting the "viewing" datum from one side to the other is less than 1%. Hence the ambiguity mentioned in Paragraph 8.1 may be safely ignored.

The experimental compliances run nearly parallel with the relative compliances obtained from finite elements. Their deviation at  $S' = 0$  is a significant 24.4%.

This discrepancy originates from deflection data. The possibility of geometric inaccuracies at the contact were mentioned in Para. 7.3.



	Finite Elements		Experimental
	Absolute	Relative	Relative
Wheel	■	□	
Pinion	▲	△	
Pair	●	○	×

FIG. 8.2 COMPLIANCE VS S' FROM FINITE ELEMENTS AND EXPERIMENTAL



It is also possible that the mesh of the finite element structure was not fine enough. The number of elements used was near the 900 maximum permissible.

Fortunately the parallel appearance of these curves suggests that the most important aspect of the compliance property is preserved. The affect on load sharing is nearly the same using either curve. This is true if the ratio of compliances of the simultaneously engaged teeth remains the same. An example is shown in the table below.

	$C_1 (S'=1.00)$ $\times 10^{-7} [\text{mm/N}]$	$C_2 (S'=0)$ $\times 10^{-7} [\text{mm/N}]$	$C_1/C_2$
Experimental	15.8	12.1	1.31
Finite elements	12.6	9.7	1.30
Deviation	25.4%	24.7%	0.8%

The resulting maximum deviation in load sharing was 3.7%.

### 8.3 Sharing of the Load in Multiple Engagement

The sharing of the load for each contact on the multiple engagement tests were found from the:

- a) Measured stresses at the "gauge points",
- b) Deflections, using graphical means.

From these experimental data a "best fit" curve was obtained as shown in Fig. (8.3)

The sharing of the load from the finite element results was determined by calculation, using Eq's. (3.9), (3.8) and (3.6).

The correlation between the experimental and finite element results and those obtained from the Cornell-Westervelt dynamic program with external compliance data was good as may be seen from Fig. (8.4).

These methods are described below.

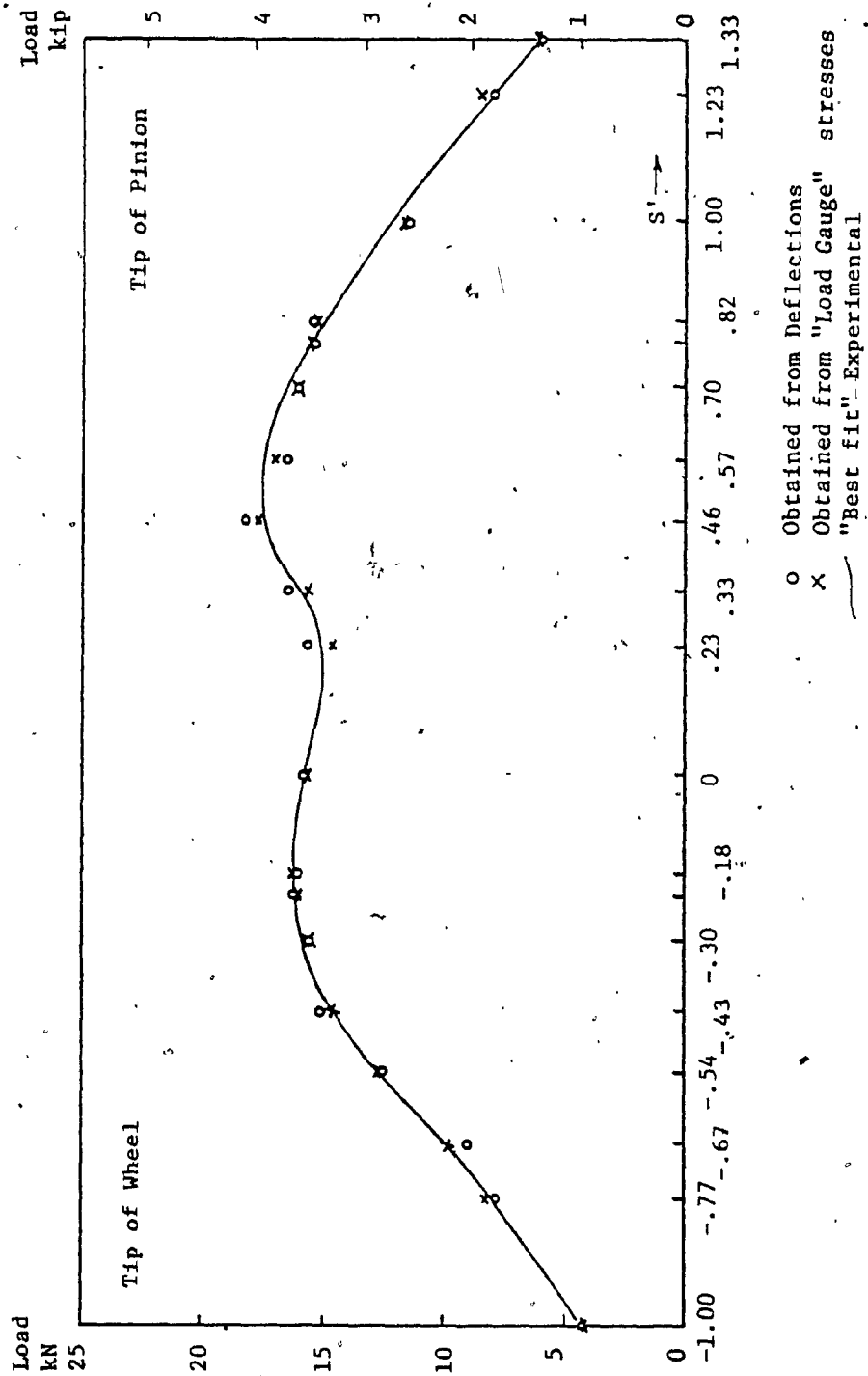


FIG. 8.3. BRANCH LOADS IN MULTIPLE ENGAGEMENT - EXPERIMENTAL

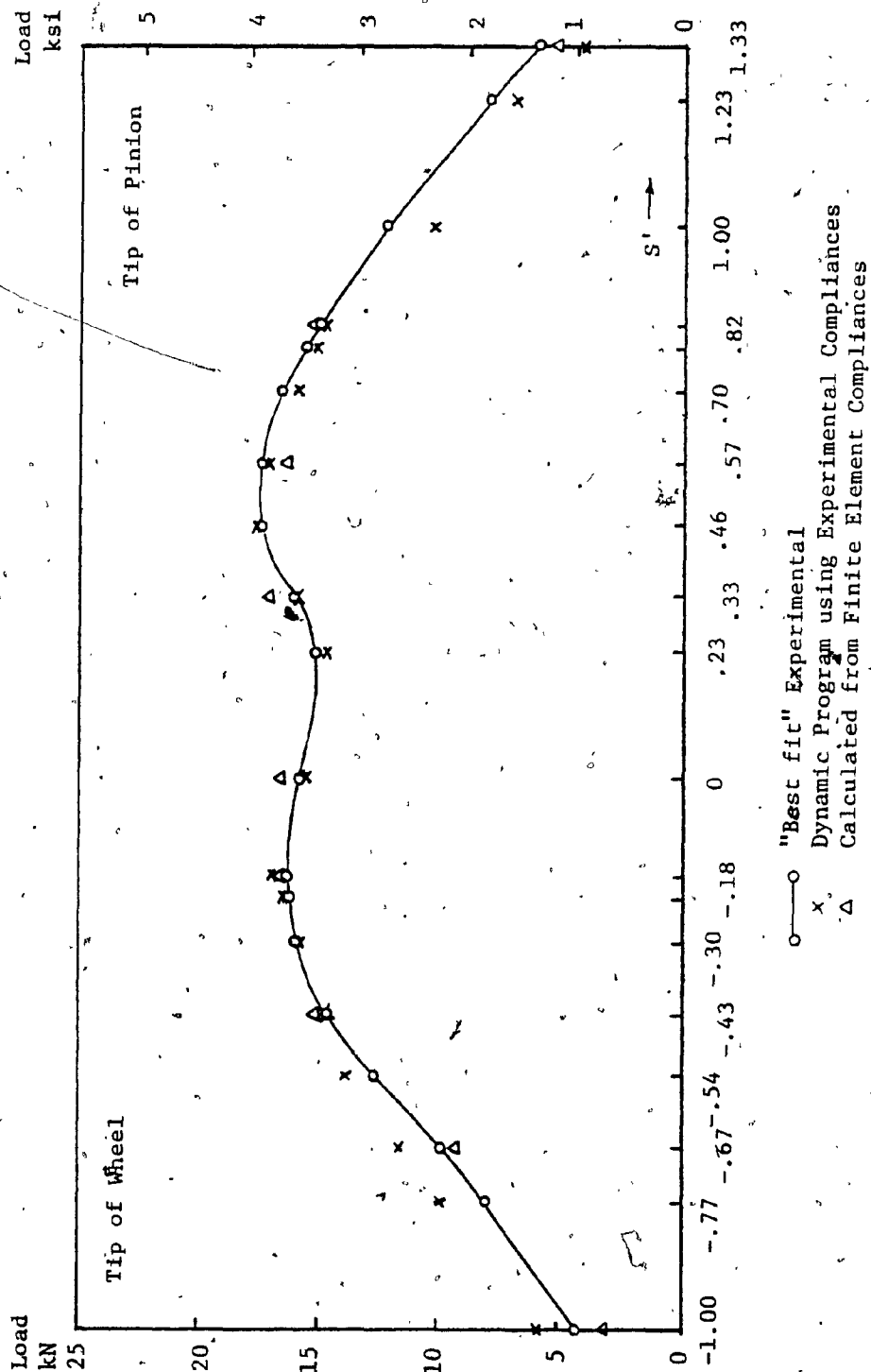


FIG. 8.4 BRANCH LOADS IN MULTIPLE ENGAGEMENT - SUMMARY

### 8.3.1 Determination of the Loads using Gage Point Stresses

A specific point on the fillet was found to be suitable for functioning as a load transducer.

The quadrant of a fillet curve which is part of a tooth under load is considered to be the "near side" of that fillet. This quadrant may lie either at the pressure or at the lee side of that tooth.

It was observed on single-pair engagement tests, that the stresses on the far sides of the fillets were zero or near zero at  $\pm 30^\circ$  fillet angles for all loading positions. This held true for the tensile and for the compressive fillets, for the pinion and for the wheel.

As the far side for say tooth "B" is the near side for tooth "C", it may be safely assumed that under multiple engagement loading the stress measured at the  $30^\circ$  fillet angle near tooth "C" can be attributed exclusively to the load on that tooth. The cross effect appears to be nil at these points, hence the  $30^\circ$  fillet angle point may be used as a load transducer.

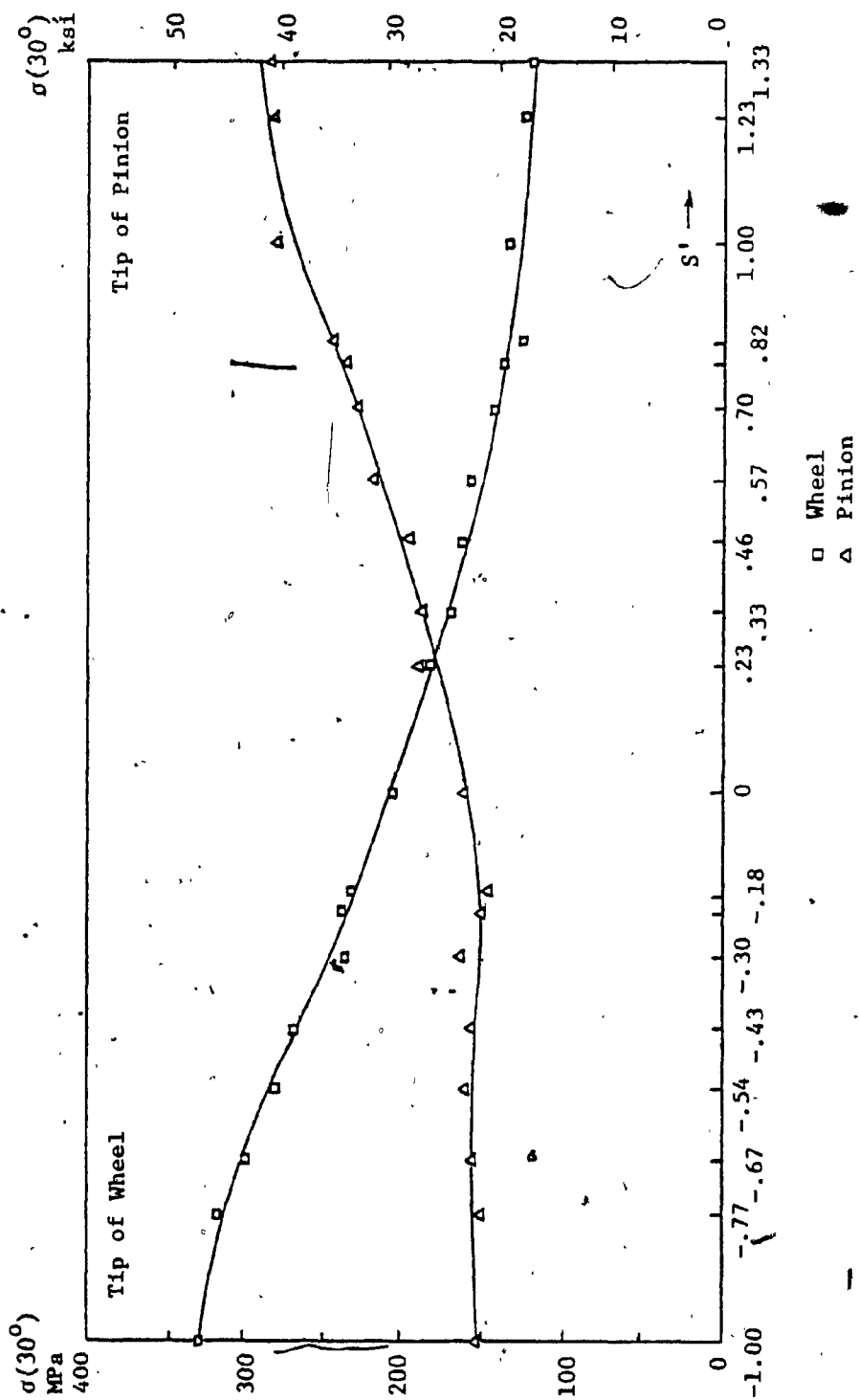
The single-pair test results were used as "gage calibration" and are plotted on Fig's. (8.5) and (8.6). The prototype equivalent of the load was 15.8 kN (3545 lbs). The "shared load" may be calculated from:

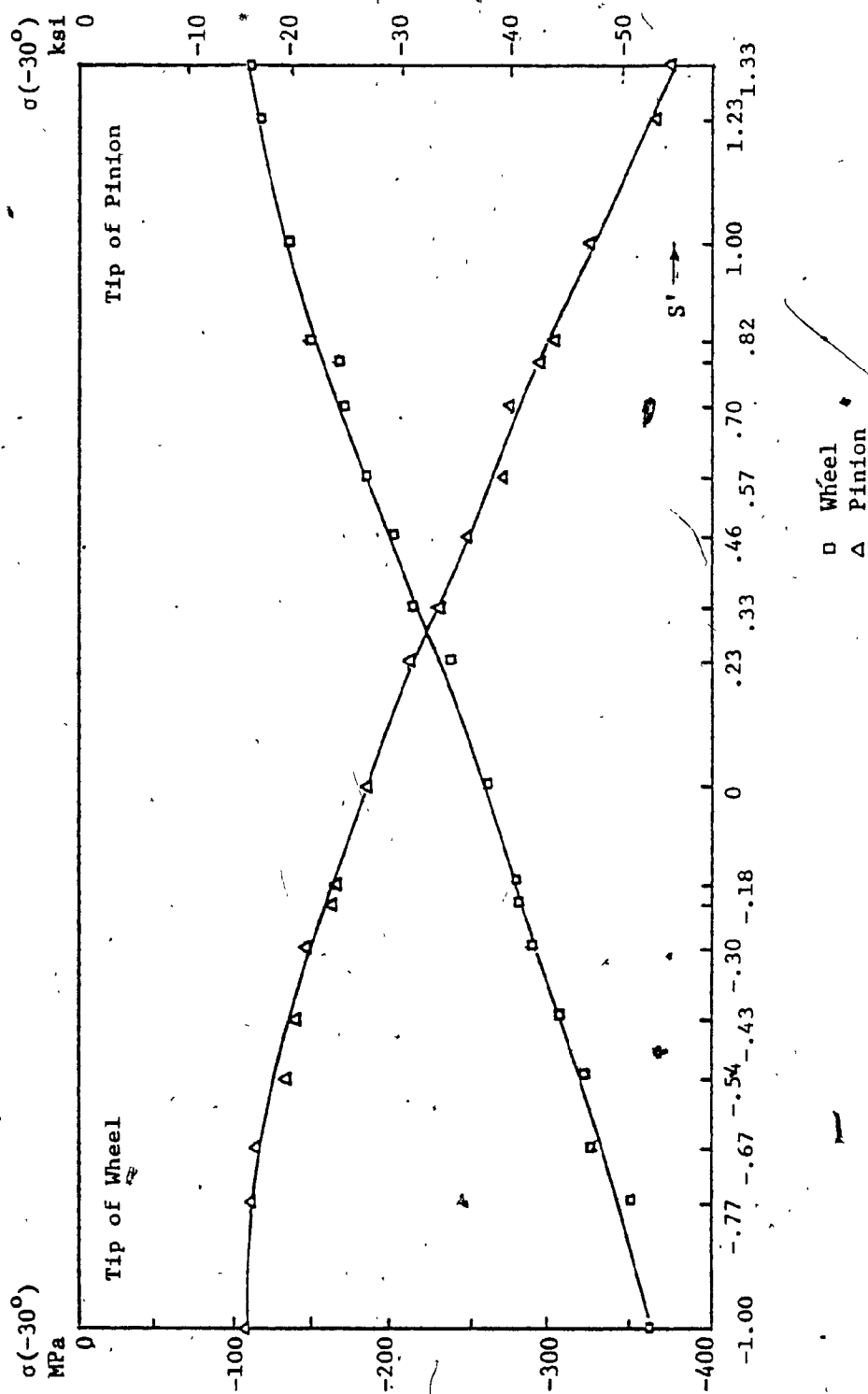
$$W_{sh} = 15.8 \sigma_{sh} / \sigma_g \quad [\text{kN}] \quad (8.1)$$

where  $\sigma_{sh}$  is the "shared stress" obtained on the multiple engagement tests due to  $W_{sh}$ ,

$\sigma_g$  is the "gage stress" obtained on the single engagement calibration runs due to a load of 15.8 kN.

Both stresses are measured at  $\pm 30^\circ$  fillet angles, where the -ve sign refers to the compressive fillet. As each branch load is surrounded by

FIG. 8.5 "LOAD GAUGE" STRESSES VS  $S'$  - TENSILE

FIG. 8.6 "LOAD GAUGE" STRESSES VS  $S'$  - COMPRESSIVE

four "near side" fillets four sets of independent data were available for each load. Using their average an improved load value was obtained.

### 8.3.2 Graphical Determination of Loads using Deflections

The non linearity of the deflection curves presented difficulties for finding a unique compliance value associated with a given loading position. This graphical method circumvents the problem. The load-deflection curves for those load points which belong to the same loading station i.e. act simultaneously, are replotted on the same graph, as on Fig's (8.7) thru (8.9). Let these curves be called set "A".

The graphical steps which follow are also illustrated on the figures:

i) The curves were redrawn in dashed lines for those loading points where there was an initial gap, in a position shifted to the right by the distance equal to that gap (set "B").

The curves with zero initial gap were not moved (set "C").

ii) The ordinates of sets "B" and "C" were added and their sum was replotted on the same graph. This curve represents load vs relative displacement for a group of pairs at a given station. It was sufficient to restrict this operation to the central region of the abscissa.

iii) The total load was therefore horizontally projected onto the sum curve, the intersection projected to the abscissa gave the group displacement. Each intersection of this vertical line with set "B" and "C" gave the respective branch loads.

### 8.3.3 Calculation of the Loads Assuming Linearity

As the deflection curves obtained from the finite element investigation appeared to be nearly linear, the computational method

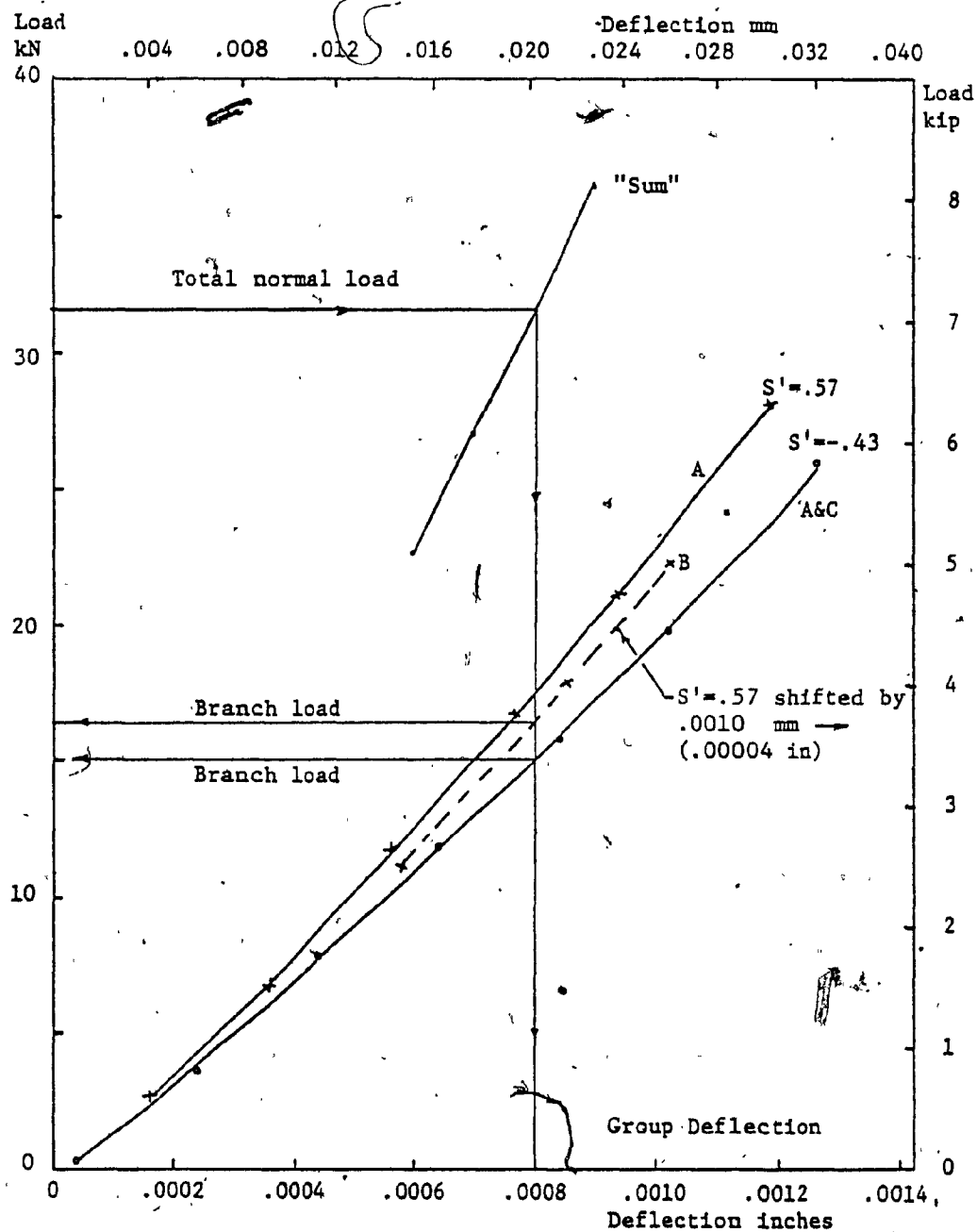


FIG. 8.7 LOAD SHARING, USING DEFLECTIONS -  $S'_{nom} = -.43$



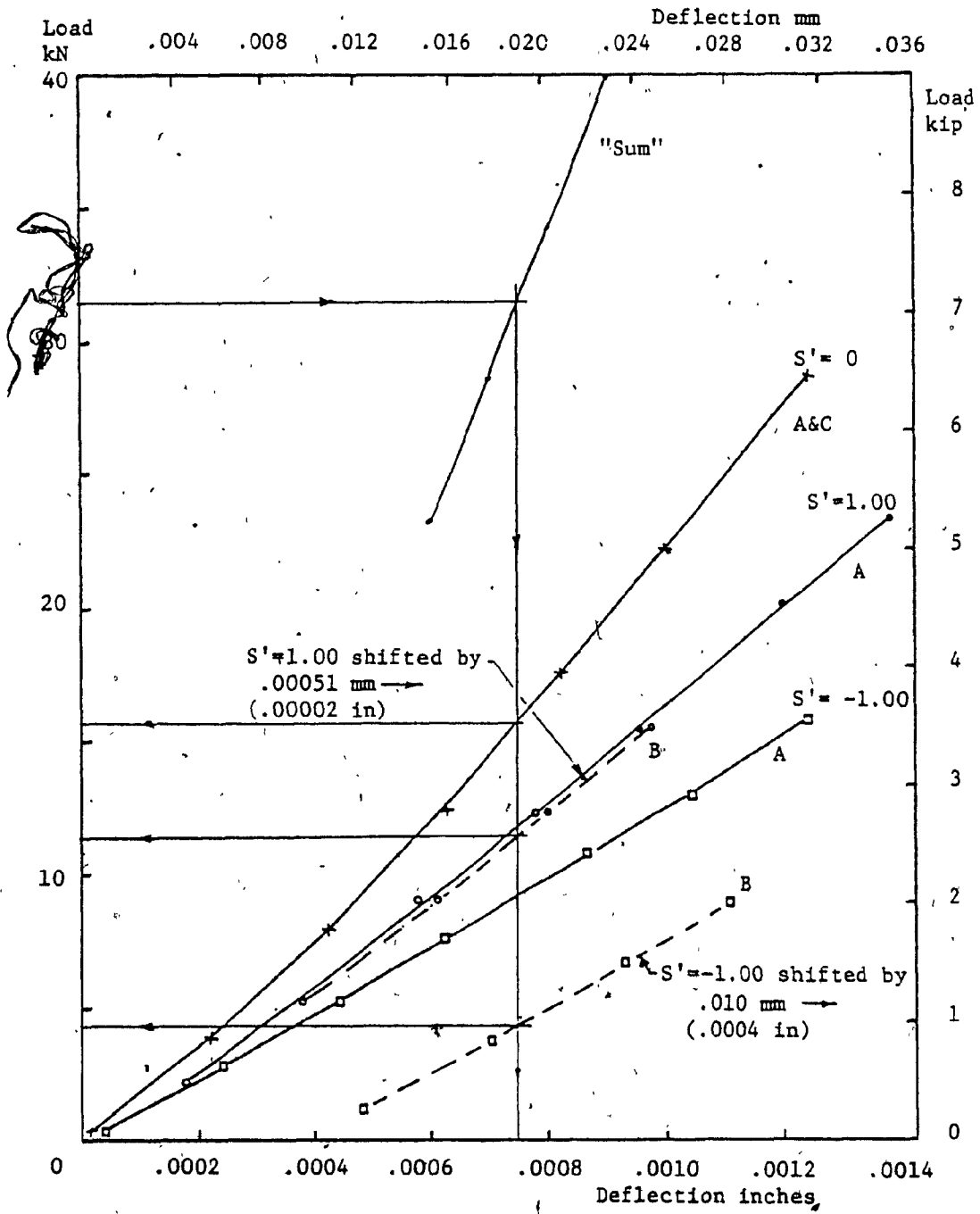


FIG. 8.8 LOAD SHARING, USING DEFLECTIONS -  $S'_{nom} = 0$

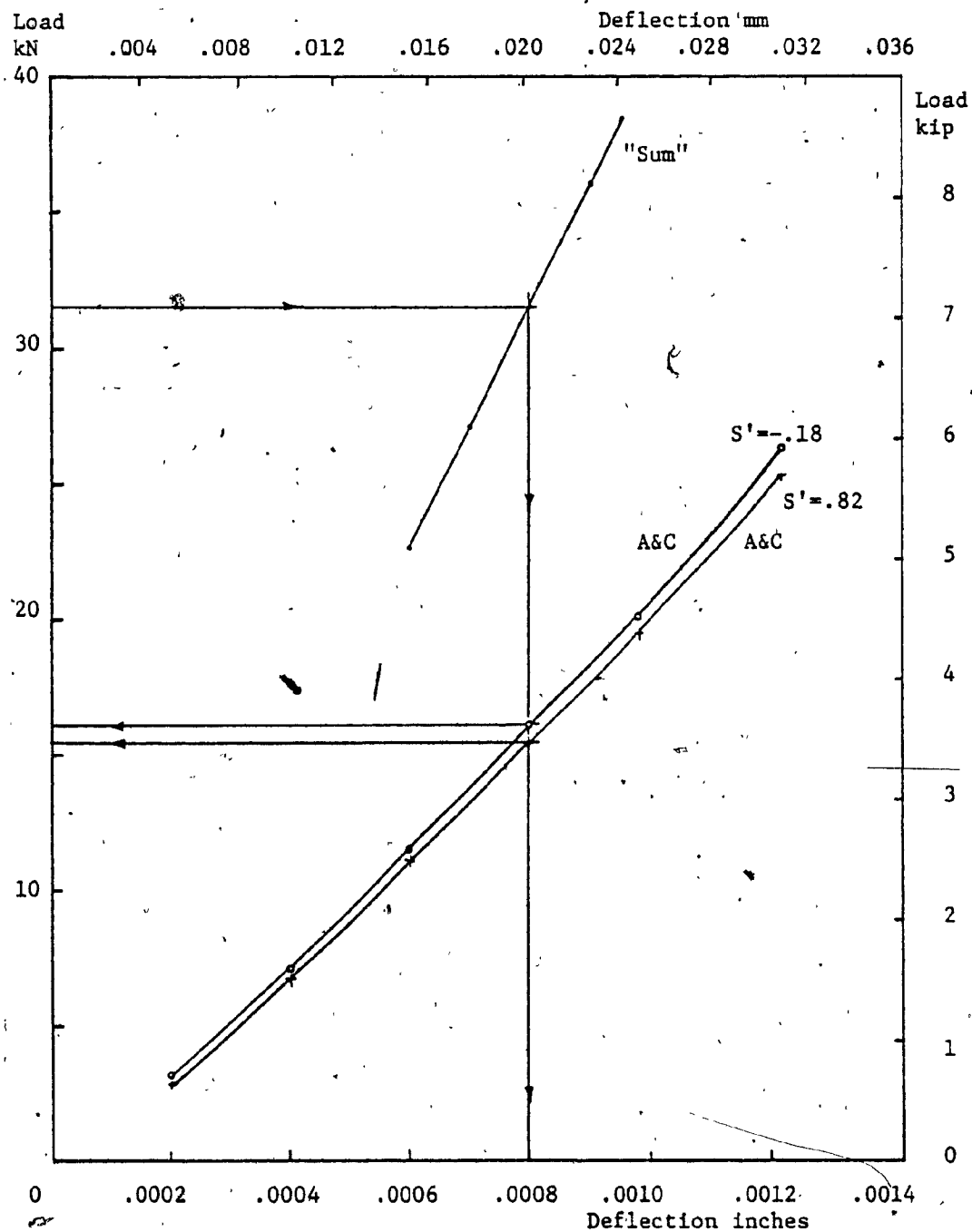


FIG.8.9 LOAD SHARING, USING DEFLECTIONS -  $S'_{nom} = .82$

described in Paragraph (3.2) was applied to these data.

The measured gaps on the model were scaled down to prototype level. The equivalent compliances were obtained from Eq.(3.9), then the group deflections were determined using Eq.(3.8). Finally the branch loads were found using Eq.(3.6) and the results are shown in Fig.(8.4), p.154.

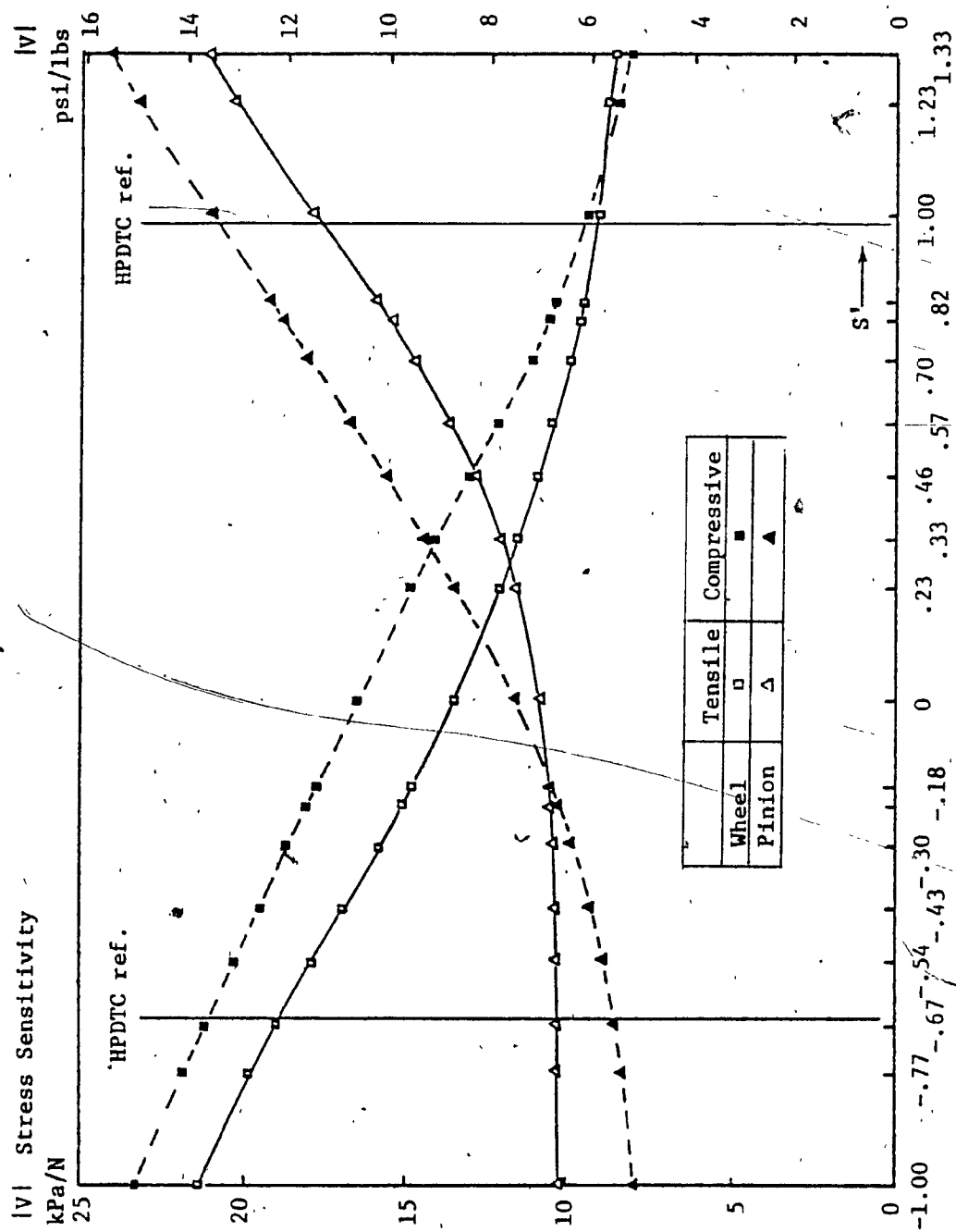
The good correlation with other data encourages an extension of this method. The composite tooth error may be represented by using a positive or negative gap respectively. The branch loads for such cases may be calculated and the fillet stresses evaluated accordingly.

#### 8.4 Stress Sensitivity and Stress Admittance

The stresses which were obtained on the Single Engagement tests and are shown in Fig's. (7.7) thru (7.10) were divided by the corresponding loads. The resulting "Stress Sensitivities" are plotted vs position along the line of action and are shown in a compact form on Fig. (8.10). Sensitivities in tension are drawn in solid lines, the absolute values of the compressive sensitivities appear in dashed lines.

The stress sensitivity values in Fig. (8.10) were then divided by the experimental compliances of Fig. (8.2). Their quotients yield the "Stress Admittances" which are plotted vs position on the line of action in Fig. (8.11). Tensile and compressive, pinion and wheel data are shown on the same graphs.

All four peaks on Fig. (8.11) are inside the limits of the "Highest Point for Double Tooth Contact". i.e. The damaging loads are successfully averted from the sensitive tip areas.

FIG. 8.10 STRESS SENSITIVITY VS  $S'$  - EXPERIMENTAL

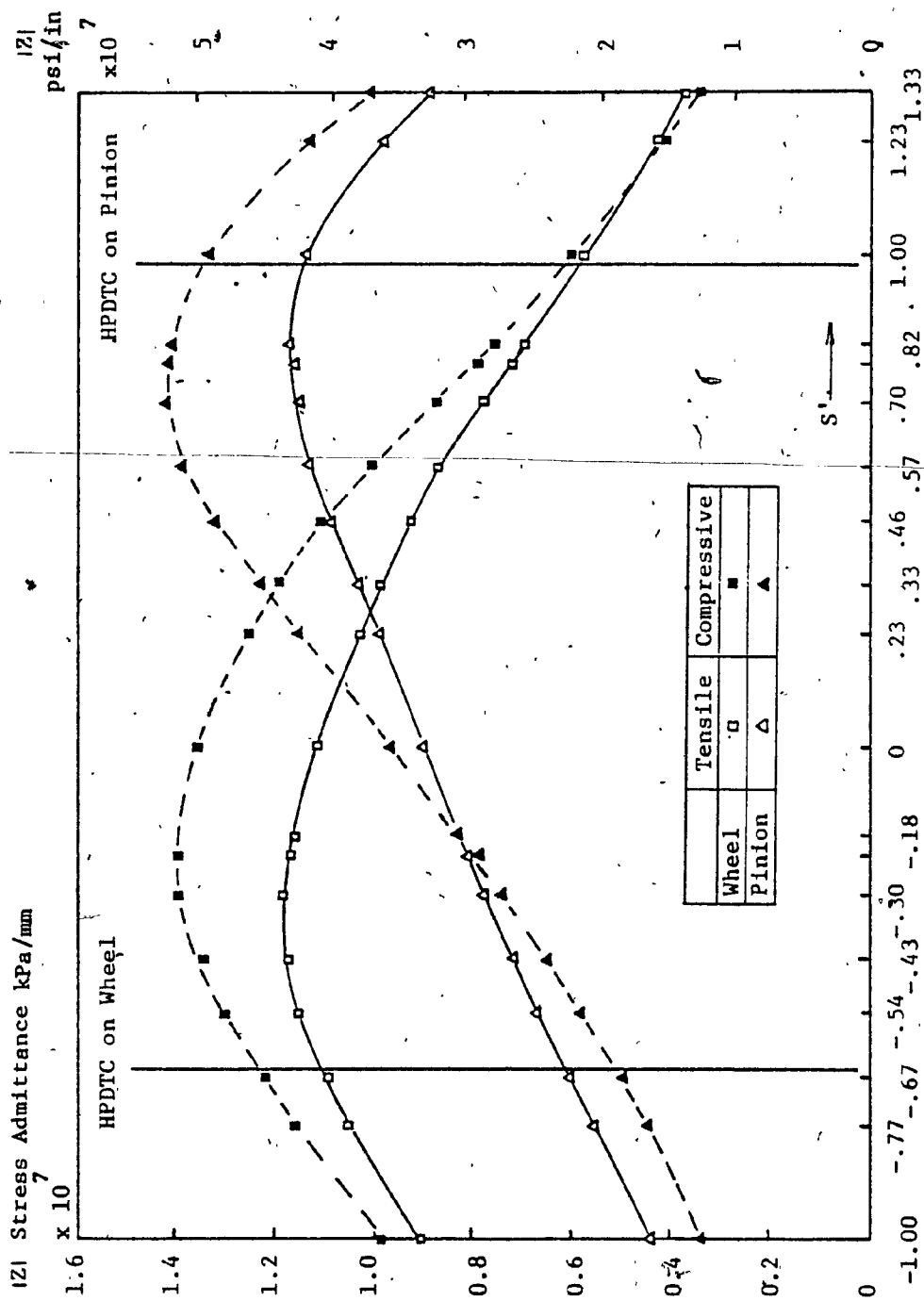


FIG. 8.11 STRESS ADMITTANCE VS S' - EXPERIMENTAL

### 8.5 Equivalent Static Alternating Stresses

Results from the Multiple-Engagement photoelastic tests were rearranged to obtain the stress excursion in a full cycle for a given location on the fillet. Four such plots are shown in Fig's. (8.12) thru (8.15). For this treatment it was necessary to define uniquely the position of a group of loads as viewed from a fillet.

Consider first a single contact as it moves along the flank of a tooth. Let the corresponding location on the line of action be called the "Labelled Position". To each such position belongs a unique set of one or two more loads which act in a distance of  $\pm$  one base pitch. By monitoring the "Labelled Position" the motion of the entire set can be defined. The range of the excursion is somewhat extended by considering the "Labelled" load acting on either the downstream or on the upstream flank with respect to the fillet.

The actual observations were made over several fillets as noted on the graphs. The rule above was then applied for the plotting of the data.

Tables 8.1 and 8.2 list the extreme stresses developed within one cycle at 22 fillet angle positions and tabulate the subsequent calculation for the Equivalent Alternating Stresses. First the stress range, the mean stress and the alternating stress components were calculated. For AMS 6265 steel an ultimate tensile stress of 1700 MPa (250 ksi) and an ultimate compressive stress of 2100 MPa (300 ksi) was used. Eq. (3.13) was expressed for the equivalent alternating stress:

$$\sigma_{ae} = \frac{\sigma_{ut} \sigma_a}{\sigma_{ut} - \sigma_m} \quad \text{for a tensile mean stress and} \quad (8.2)$$

$$\sigma_{ae} = \frac{\sigma_{uc} \sigma_a}{\sigma_{uc} - \sigma_m} \quad \text{for a compressive } \sigma_m \quad (8.3)$$

The calculated values are shown in Fig. (8.16).

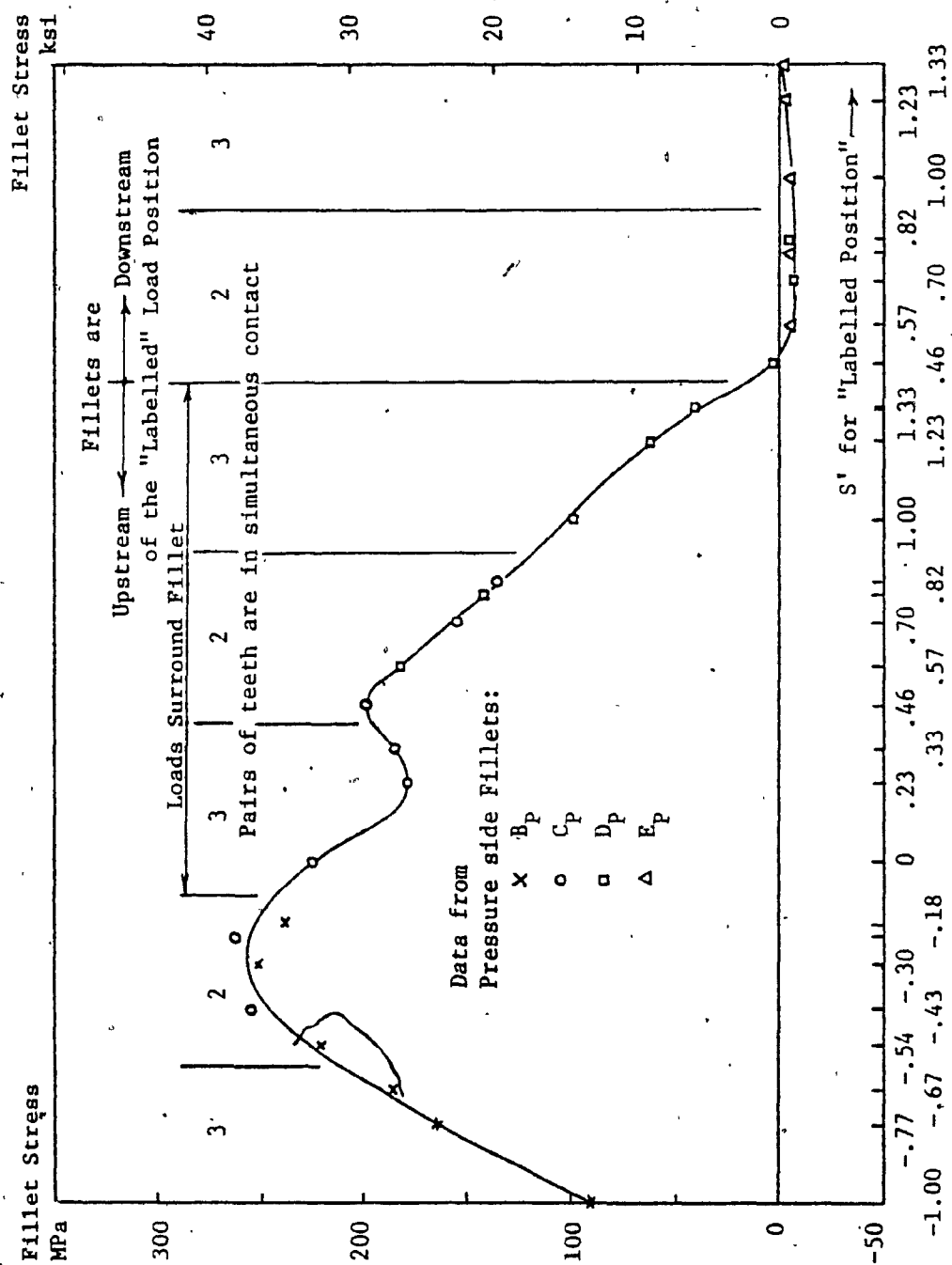
The maximum value for  $\sigma_{ae}$  is 156 MPa (22.6 ksi) for the wheel and 163 MPa (23.6 ksi) for the pinion. Both values originate from points in the compressive fillets. Each of these equivalent alternating stresses are higher than those caused by the maximum tensile fillet stresses alone by

8.1% for the wheel and by

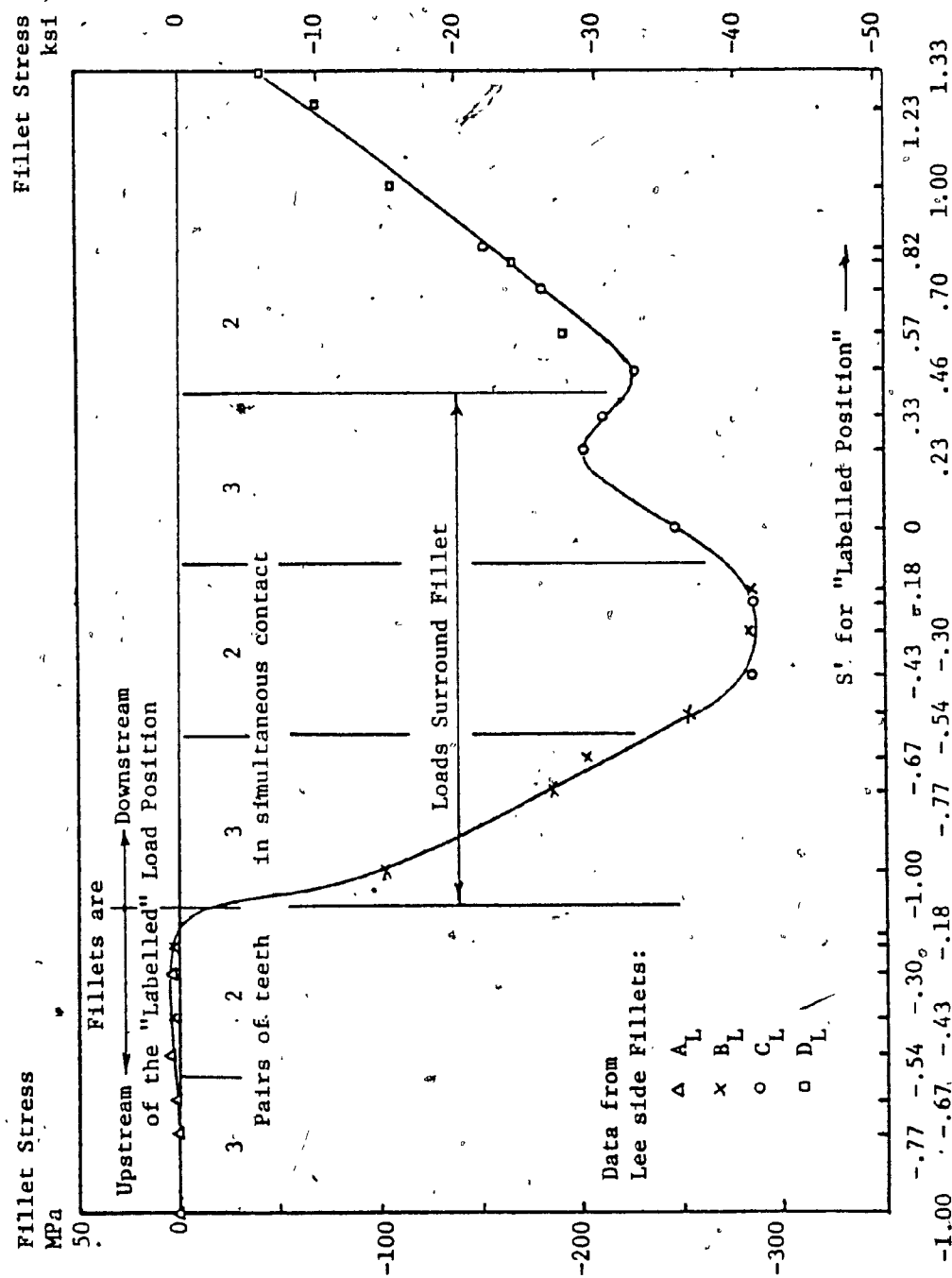
19.6% for the pinion.

It is emphasized that these results are not intended for predicting fatigue life. They merely demonstrate that other stress ranges may be more damaging than the range from zero to  $\sigma_{tmax}$ . An early crack at the location of  $\sigma_{cmax}$  may or may not lead to catastrophic failure.

Exploring this subject is a worthwhile topic for further research.

FIG. 8.12 STRESS EXCURSION - WHEEL, PRESSURE SIDE,  $\gamma = 40^\circ$



FIG. 8.13 STRESS EXCURSION - WHEEL, LEE SIDE,  $\gamma = -33^\circ$

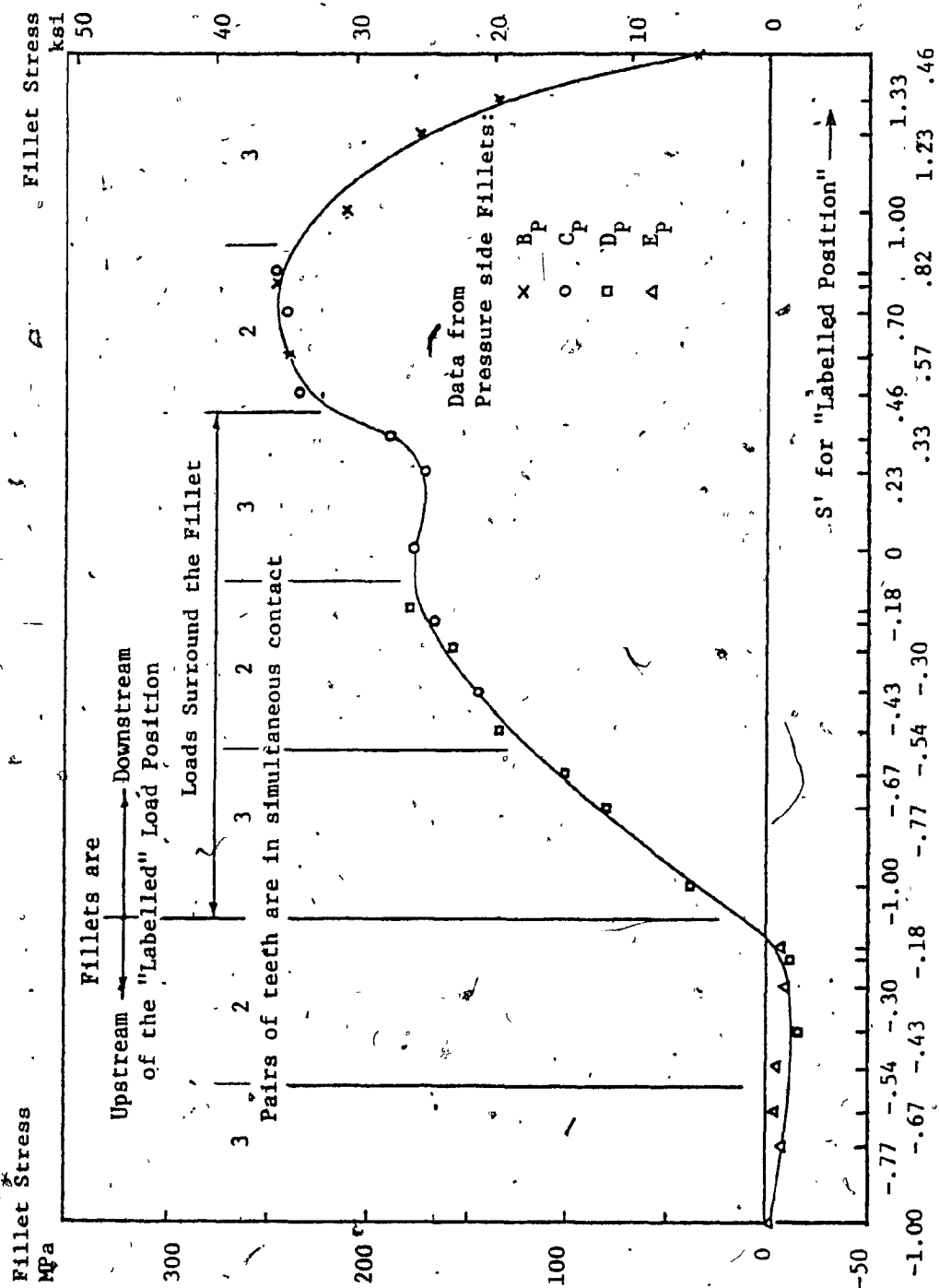


FIG. 8.14 STRESS EXCURSION - PINION, PRESSURE SIDE,  $\gamma = 40^\circ$

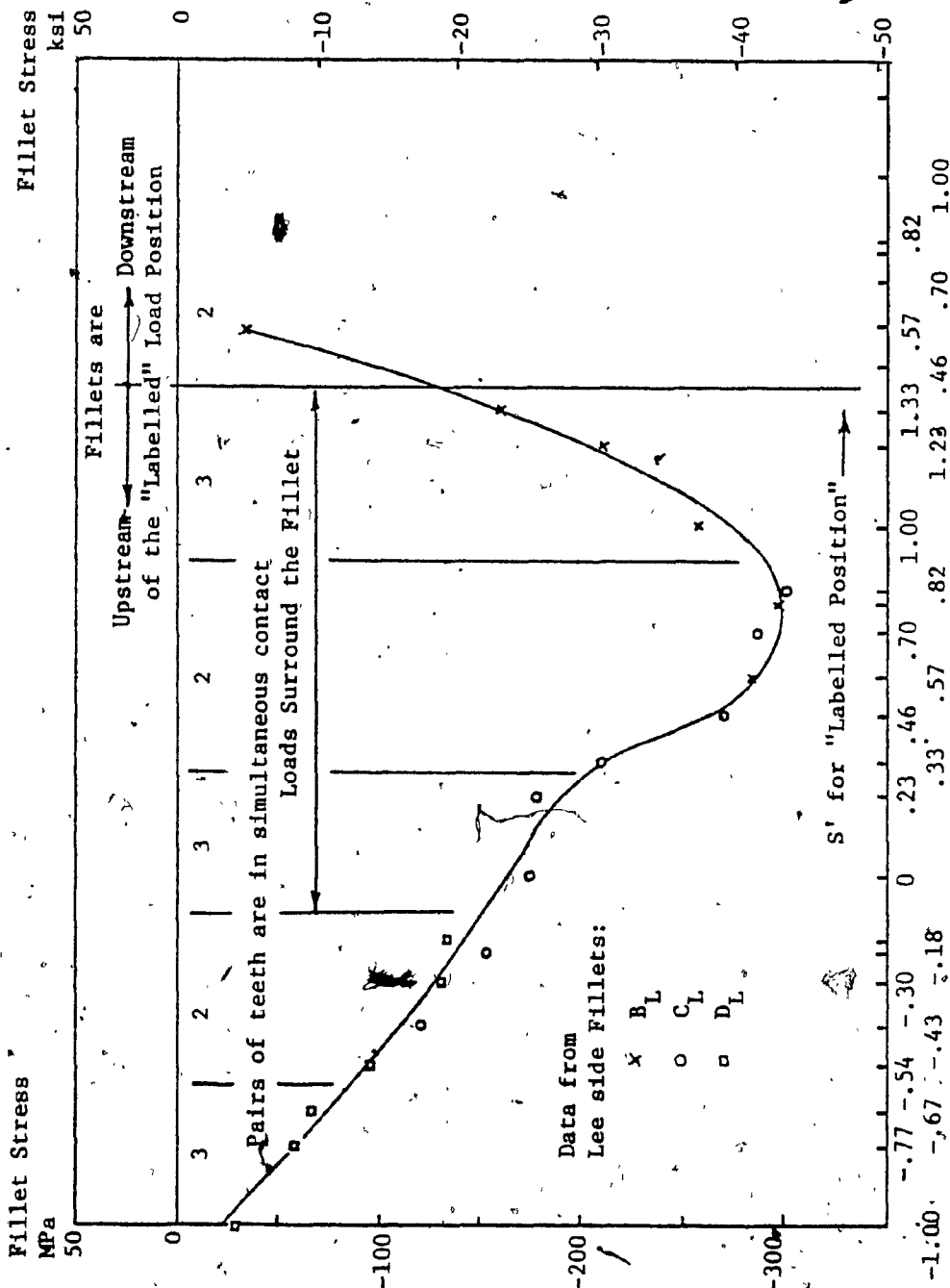


FIG. 8.15 STRESS EXCURSION - PINION, LEE SIDE,  $\gamma = -26^\circ$

Table 8.1

"Equivalent Alternating Stresses" - Wheel  
(Zero Mean Stress)

Obtained in static tests, excluding effects of

- 1) Dynamic loads
- 2) Manufacturing errors

All stresses in MPa except where shown as (Ksi)

$\gamma^\circ$	Stress Range	$\sigma_m$	$\pm \sigma_a$	$\sigma_{ae}$ (Ksi)	
0	169.6	84.8	84.8	89	12.9
10	197.2	98.6	98.6	105	15.2
20	230.2	115.1	115.1	123	17.9
30	252.4	126.2	126.2	136	19.8
37	266.2	133.1	133.1	144	20.9
40	268.2	127.9	134.1	145	21.0
50	269.6	117.6	134.8	145	21.0
60	262.6	94.1	131.3	139	20.2
70	255.2	68.9	127.6	133	19.3
80	251.7	38.3	125.8	129	18.7
89	246.1	10.7	123.1	124	18.0
-89	244.8	1.7	122.4	123	17.8
-80	243.4	-23.1	121.7	123	17.9
-70	244.8	-47.9	122.4	125	18.2
-60	245.5	-74.5	122.7	127	18.5
-50	269.2	-107.2	134.1	141	20.5
-40	290.3	-130.7	145.1	155	22.5
-33	290.3	-141.7	145.1	156	22.6
-30	286.1	-141.0	143.1	154	22.3
-20	256.5	-128.2	128.2	137	19.8
-10	227.5	-113.8	113.8	120	17.5
0	199.9	-100.0	100.0	105	15.2

\* Location of maximum tensile and compressive peaks respectively.

\*\* Maximum  $\sigma_{ae}$  in tension domain.

$\sigma_{ae}$  is based on

$\sigma_{ut} = 1700 \text{ MPa (250 Ksi)}$  and  $\sigma_{uc} = 2100 \text{ MPa (300 Ksi)}$

Table 8.2

"Equivalent Alternating Stresses" - Pinion,  
(Zero Mean Stress)

Obtained in static tests, excluding effects of

- 1) Dynamic loads
- 2) Manufacturing errors

All stresses in MPa except where shown as (Ksi)

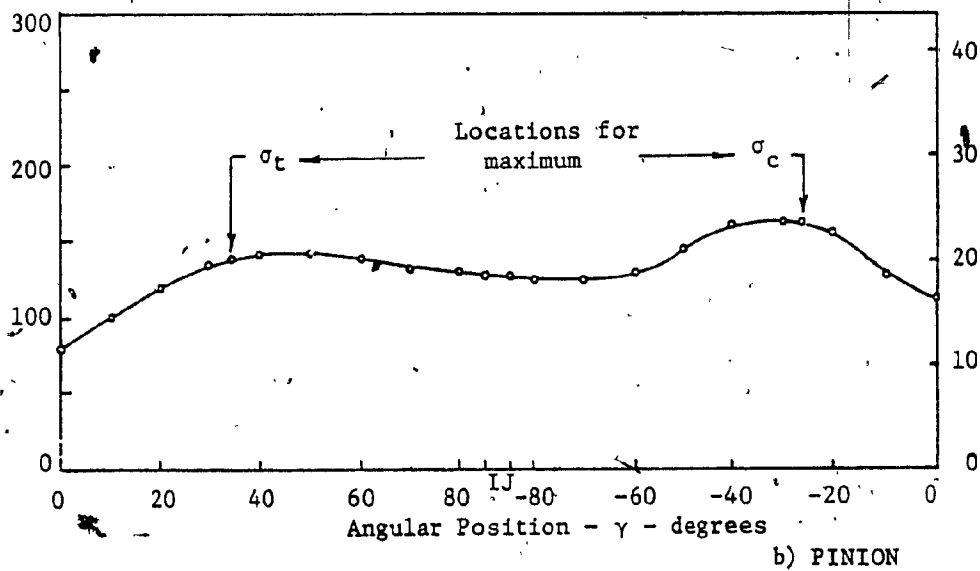
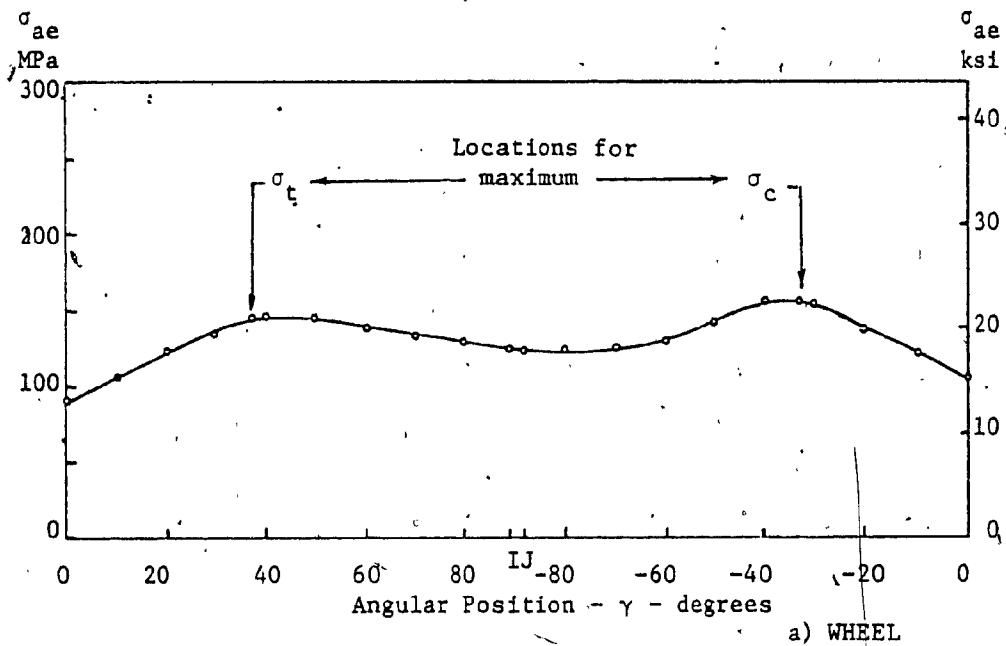
$\gamma^\circ$	Stress Range	$\sigma_m$	$\pm \sigma_a$	$\sigma_{ae}$ (Ksi)	
0	152.4	76.2	76.2	80	11.6
10	188.9	94.5	94.5	100	14.5
20	224.1	112.0	112.0	120	17.4
30	248.2	122.0	124.1	134	19.4
34	254.4	125.1	127.2	137	19.9
40	264.1	114.8	132.0	142	20.5
50	266.1	100.0	133.1	141	20.5
60	263.4	78.6	131.7	138	20.0
70	255.1	49.6	127.6	131	19.1
80	256.5	23.4	128.2	130	18.9
85	253.0	7.9	126.5	127	18.4
-85	252.3	-4.8	126.2	126	18.3
-80	248.9	-17.6	124.5	126	18.2
-70	244.1	-41.4	122.0	125	18.1
-60	244.8	-65.2	122.4	126	18.3
-50	274.4	-101.4	137.2	144	20.9
-40	299.2	-131.7	149.6	160	23.2
-30	302.0	-148.2	151.0	163	23.6
-26	302.0	-151.0	151.0	163	23.6
-20	291.0	-145.5	145.5	157	22.7
-10	239.9	-120.0	120.0	127	18.5
0	209.6	-104.8	104.8	110	16.0

\* Location of maximum tensile and compressive peaks respectively.

\*\* Maximum  $\sigma_{ae}$  in tension domain.

$\sigma_{ae}$  is based on

$\sigma_{ut} = 1700 \text{ MPa (250 Ksi)}$  and  $\sigma_{uc} = 2100 \text{ MPa (300 Ksi)}$



Data were generated under static conditions excluding the effects of:

- i) Dynamic loads
- ii) Manufacturing errors

FIG. 8.16 EQUIVALENT "STATIC ALTERNATING" STRESSES

AN ESTIMATE OF THE ERRORS

An experiment may be prepared and conducted with utmost care, but the results still carry some errors. It is good practice to give an estimate of these deviations.

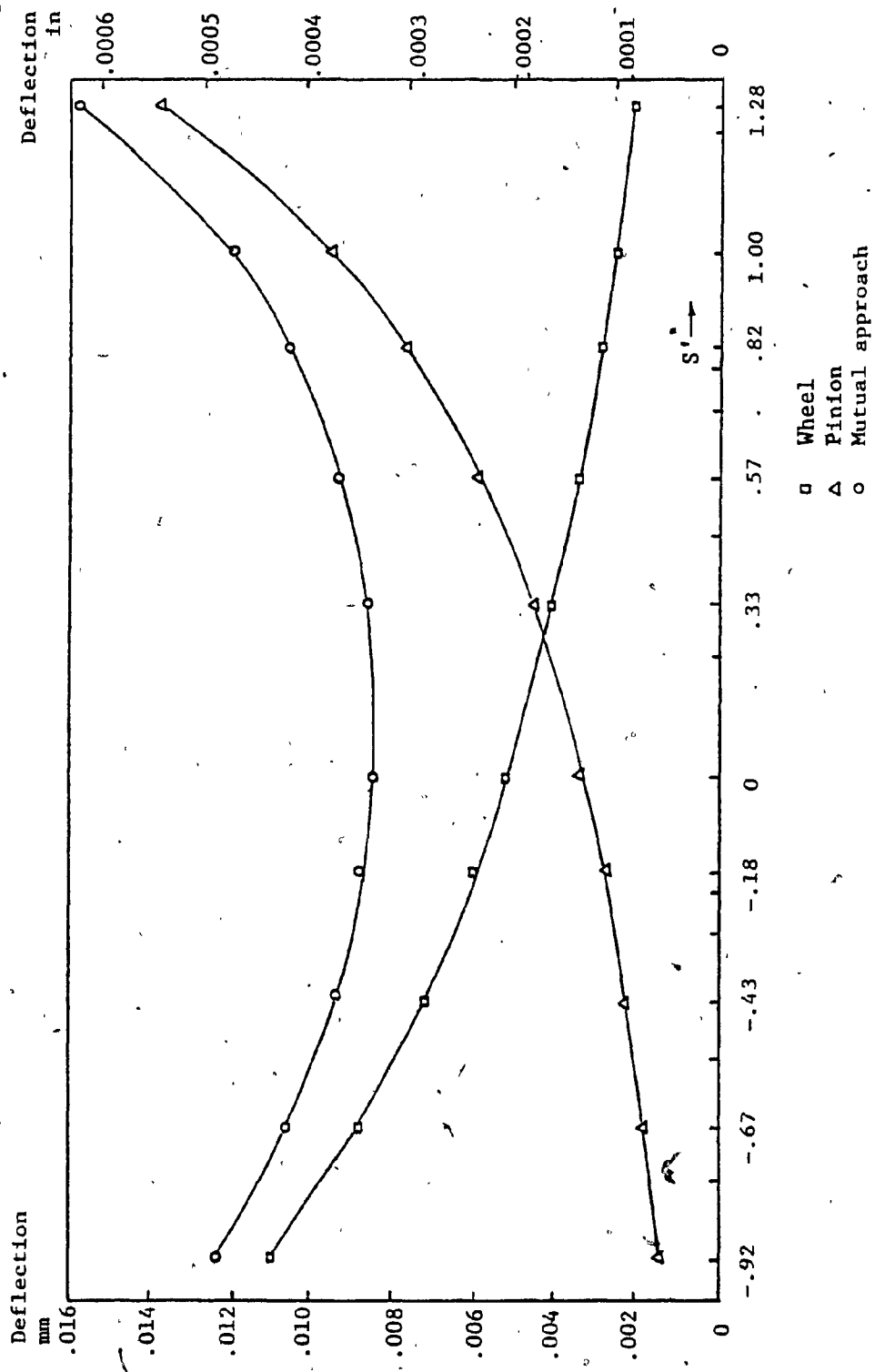
There are two basic types of discrepancies. The limited precision of the various instrument readings leads to errors of random distribution. This type of scatter may be described by the probable error, by the standard deviation or by some other similar deviation parameter Ref. [25], Para. 3.1.

The shift of the mean of the data from the "true value" or bias is likely to be caused by instruments which drifted off their calibration or by faulty test conditions.

### 9.1 Bias Due to Parasitic Loading

Friction at the contacting surfaces is markedly different for the model under static loading, and for the prototype running in the gearbox. The oil film due to dynamic lubrication maintains an effective coefficient of friction of 0.03 - 0.04. The direction of the frictional force at the meshing surfaces reverse as the position of the contact moves from the line of approach to the line of recession.

The frictional coefficient at the machined surfaces of the plastic is typically 0.4. Hence a tooth of the model may carry a tangential traction of 40% normal load, distorting the results beyond recognition. The finite element data indicates (Fig. 9.1) that the tangential component of the displacement at the contact in all cases points away from the gear body. Consequently the frictional forces are directed mutually toward the respective gear bodies in the static test.

FIG. 9.1 SLIDING COMPONENT DUE TO DEFLECTION, VS  $S'$



After some experimentation with oil and dry lubricants it was found that if two sheets of .076 mm (.003") thick teflon are placed between the contacting surfaces, the frictional coefficient may be reduced to 0.1. The tractions were possibly further reduced by the practice of gently plucking the loading cable after the load was applied. Thus vibration was induced to the contact, which may have partially relieved the contact surface of these tractions.

The Aida-Terauchi formula and a few finite element program runs were used to evaluate the effects of an assumed frictional force of 0.1 W. It was found that for the significant addendum loadings the average reduction of tensile stresses was 9.8% and those for the compressive stresses 4.9%.

It is unlikely that the frictional forces always develop quite to their maximum value. Therefore  $\sigma_t$  in the photoelastic test may have been underestimated by say 8%, the compressive maxima by 4%. To these a small value of 0.2% may be added for the loss of load due to friction at the pulleys.

## 9.2 Random Errors

These errors may originate from a number of sources, each contributing to the total in a specific manner. For numerical assessment some assumptions must be made.

Let us assume that these errors have a normal distribution.

As an arbitrary choice, the scatter for each type of error will be characterized by its standard deviation "s".

The stress on a free surface from Eq. (5.18):

$$\sigma = N'f/B \quad (9.1)$$

where  $N'$  is the fringe order

$F$  is the material fringe constant

$B$  is the thickness of the model

The stress from Eq. (3.1):

$$\sigma = VW \quad (9.2)$$

where  $V$  is the stress sensitivity

$W$  is the normal load

Considering that the model is not perfect and assuming arbitrarily that there is a linear factor  $K_m$  which relates the actual stress sensitivity to the "true" sensitivity  $V_t$  of a "perfect" model

$$V = K_m V_t \quad \text{then} \quad (9.3)$$

$$\sigma = K_m V_t W \quad (9.4)$$

from Eq's. (9.1) and (9.4)

$$V_t = \frac{N'f}{B K_m W} \quad (9.5)$$

Each of these variables represent a specific source of error:

$N'$  The fringe order may vary due to the inaccuracy of the instrument and the subjective errors in the reading of the fringe. The standard deviation of this type of scatter may be 2%

$$\text{or } s_{N'}/N' = .02$$

$f$  The material fringe constant obtained by calibration is of similar nature to  $N'$ . However replications and treating the results with linear regression a much better value, say 0.5%, was obtained.

$$\text{Hence } s_f/f = 0.005$$

B The thickness of the material may vary  $\pm 0.5\%$

$$s_B/B = 0.005$$

K<sub>m</sub> The nature of the variation in model accuracy is uncertain. However great care was taken to achieve a maximum deviation of 0.001 mm (0.0004") in the base pitch at assembled condition. The small value may justify linearization. Guesstimating this error to be 1% or

$$s_m/l = 0.01$$

W The uncertainty whether the tractions at the contact have developed to their mean bias or not adds a random component to this error.

Assuming this to be 2%  $s_W/W = 0.02$

A treatment of uncertainty in complete experiments is given by H. Schenck Jr. [25].

A result of an experiment R is a function of X, Y, etc when R<sub>c</sub>, X<sub>c</sub>, Y<sub>c</sub> are the true values. The variance of the result:

$$(s_r)^2 = \left( \frac{\partial R}{\partial X_c} \right)^2 s_x^2 + \left( \frac{\partial R}{\partial Y_c} \right)^2 s_y^2 \quad (9.6)$$

ref [25], Eq. (3.14)

The contribution of the variance of N' to the total variance of V<sub>t</sub> using Eq. (9.5):

$$\left( \frac{\partial V_t}{\partial N'_c} \right)^2 s_{N'}^2 = \left( \frac{f}{B K_m W} \right)^2 s_{N'}^2 \quad (9.7)$$

Then the variance fraction of the same with respect to V<sub>t</sub>:

$$\left( \frac{f}{B K_m W} \right)^2 \left( \frac{s_{N'}}{V_t} \right)^2 = \left( \frac{f}{B K_m W} \right)^2 s_{N'}^2 \left( \frac{B K_m W}{N' f} \right)^2 = \left( \frac{s_{N'}}{N'} \right)^2 \quad (9.8)$$

Similarly, taking an example from the denominator of Eq. (9.5) the contribution to the total variance of s<sub>W</sub>:

$$\left( \frac{\partial V_t}{\partial W_c} \right)^2 s_w^2 = \left( \frac{-N' f}{B K_m W^2} \right)^2 s_w^2 \quad (9.9)$$

Its fractional contribution:

$$\left( \frac{-N' f}{B K_m W^2} \right)^2 s_w^2 \left( \frac{B K_m W^2}{N' f} \right)^2 = \left( \frac{s_w}{W} \right)^2 \quad (9.10)$$

The percentage error in stress sensitivity based on Eq's. (9.8) and (9.10):

$$\begin{aligned} 100 \left( \frac{s_{vt}}{v_t} \right) &= 100 \left[ \left( \frac{s_{N'}}{N'} \right)^2 + \left( \frac{s_f}{f} \right)^2 + \left( \frac{s_B}{B} \right)^2 + \left( \frac{s_m}{K_m} \right)^2 + \left( \frac{s_w}{W} \right)^2 \right]^{\frac{1}{2}} \\ &= 100 (.02^2 + .005^2 + .005^2 + .01^2 + .02^2)^{\frac{1}{2}} = 3.08\% \end{aligned}$$

According to these figures 68.2% of the photoelastic test results fall within  $\pm 3.08\%$  of the "true values" over and above the bias, a likely underestimate of 8% for the tensile and 4% for the compressive maxima. This estimate of the total error is as good as the estimate of the errors of the components.

CONCLUSIONS AND CONTRIBUTIONS10.1 Conclusions

The stressing of the fillet in multiple engagement is primarily controlled by the sharing of the load, which in turn depends upon the variable compliance of a pair of contacting teeth.

The finite element method gave significantly lower compliances (24%) than those obtained experimentally. However the two curves are essentially parallel, the difference appears along the vertical axis. Consequently both results have lead to nearly identical load sharing. These loads correlate well with those obtained from the dynamic program, which was run with experimental compliances.

The interaction of deflections modifies the load sharing only slightly (1%), as the "relative" and "absolute" compliances obtained from finite elements are also nearly parallel, with the latter being lower by 7%.

The direct cross effect of stresses between adjacent teeth at the location of the peak stresses is small, an average of 6%. It is significant only at the fillet bottom, where it is beneficially attenuating.

The stresses obtained using finite elements are slightly higher than those determined photoelastically, both giving acceptable low values. The tensile stresses for the wheel are 266 MPa (38.6 ksi) and they are 5.5% higher than those for the pinion, (252 MPa, 36.6 ksi).

The closed form Aida-Terauchi equation gave remarkably good correlation with the photoelastic and finite element results.

The Kelley-Pedersen "stress shift" equation calculated accurately the location of the tensile peaks.

The Stress Admittance plots show that all four peaks fall well within the limits set by "The Highest Points for Double Tooth Contact". This indicates that the selected contact ratio and tooth forms constitute a design where the load carrying capacity of the material is effectively used.

The "Equivalent Static Alternating Stress" curves indicate that the most severe stress ranges seem to exist near the compressive maxima. It is not claimed that these locations are in fact the weakest points. However it is suggested that for proper fatigue analysis the stresses be monitored under dynamic conditions along the entire fillet curve.

#### 10.2 Contributions to the Art

- i) The concept of "Stress Admittance" was introduced, which gave the critical location of the load for the wheel and for the pinion respectively. It also lends itself to calculate multiple engagement stresses from single pair stress and deflection data. Combining this feature with load sharing Eq's (3.9, 3.8 and 3.6) a complete analysis is possible using a pair of finite element models with single tooth loading.
- ii) To the best knowledge of the author no attempt was made before to build a High Contact Ratio - Multiple Engagement photoelastic model, which was made using novel techniques. Unfortunately it is inherent in this type of model that surface traction effects can be not be completely eliminated.
- iii) The concepts of "Relative Pair Deflection" and of "Relative Pair Compliance" describe precisely the elastic behaviour of a pair of

gear teeth in multiple engagement. These parameters account for the interactive displacement of the adjacent teeth, thus, the sharing of the load may be determined slightly more accurately.

- iv) The Isotropic point used as a datum isolates the deflection of the tooth from the deflection of the rim.
- v) The observation of the "30° near zero stresses" yielded an independent method to determine the sharing of the load between parallel acting tooth pairs.
- vi) The graphical method to determine the sharing of the load circumvented the difficulties arising from the apparent non-linearity of deflection vs load.
- vii) The notion of positive and negative gaps in conjunction with the load sharing analysis in Chapter 3 opens the possibility to account for the effects of "composite error".
- viii) The extension of the Aida-Terauchi formula permits calculation of the compressive maxima and the effects of friction on fillet stresses.

LIST OF REFERENCESA. Primary Sources

1. Aida T., Terauchi Y. "On the Bending Stress of a Spur Gear (1st Report, Stress at the Fillet Curve and Inner Stress at the Root of Gear Tooth)", Bulletin of JSME, Vol.5, No.17, 1962, pp.161-170
2. Aida T., Terauchi Y. "On the Bending Stress of a Spur Gear (2nd Report, The Stress Concentration Factor and the Equation for the Calculation of Bending Stress of a Gear Tooth)", Bulletin of JSME, Vol.5, No.17, 1962, pp.170-176
3. Allison I.M., Hearn E.J. "A New Look at the Bending Strength of Gear Teeth", Experimental Mechanics, July 1980
4. American Gear Manufacturers Standard 220.02 "Rating the Strength of Spur Gear Teeth", Aug.1966
5. Baronet C.N., Tordian G.V. "Exact Stress Distribution in Standard Gear Teeth and Geometry Factors", ASME, Journal of Engineering for Industry, Nov.1973
6. Buckingham E. "Manual of Gear Design" - Section One, Sponsored by AGMA, The Industrial Press, New York, 1937
7. Chabert G., Dang Tran T., Mathis R. "An Evaluation of Stresses and Deflection of Spur Gear Teeth Under Strain", Journal of Engineering for Industry, Feb.1974
8. Cornell R.W. "Compliance and Stress Sensitivity of Spur Gear Teeth", Transactions of ASME, Journal of Mechanical Design No.80-C2/DET-24, 1980
9. Cornell R.W., Westervelt W.W. "Dynamic Tooth Loads and Stressing for High Contact Ratio Spur Gears", ASME, Journal of Mechanical Design, Jan.1978, Vol.100
10. Dally J.W., Riley W.F. "Experimental Stress Analysis", Chapter 9.6, McGraw-Hill, 1965
11. P.D Dimantha "On Distributed Loads and Consistent Loads for Parabolic Elements", unpublished note, 24 Aug 1977.
12. Dolan T.J., Broghamer E.L. "A Photoelastic Study of Stresses in Gear Tooth Fillets", University of Illinois, Engineering Experimental Station Bulletin No.335, 1942
13. Dudley D.W. "Gear Handbook", McGraw-Hill, 1962



14. Durelli, A.J., Phillips E.A., Tsao C.H. "Introduction of the Theoretical and Experimental Analysis of Stress and Strain", Paragraph 12.11, McGraw-Hill, 1958
15. Elkholy A, Smythe C "A 2D Finite Element Stress Analysis on RGB using HCRG and LCRG Spur Gear Teeth", unpublished note, April 21, 1980
16. R.H., Gallagher, "Finite Element Analysis Fundamentals", Chapters 6,7, Prentice Hall 1975
17. Heywood R.B. "Designing by Photoelasticity", Chapman and Hall 1952
18. Heywood R.B. "Tensile Fillet Stresses in Loaded Projections", Proceedings of Institution of Mechanical Engineers, Vol.159, 1948, pp.384-398
19. Jacobson M.A. "Bending Stresses in Spur Gear Teeth: Proposed New Design Factors Based on Photoelastic Investigation", Proceedings of Institute of Mechanical Engineers, Vol.169 (31), 1955, pp.587-609
20. Kelley B.W., Pedersen R. "The Beam Strength of Modern Gear Tooth Design", SAE Transactions, Vol.66, 1958
21. Muskhelishvili N.I. "Some Basic Problems of the Mathematical Theory of Elasticity", Nordhoff Ltd., Groningen - Holland, 1953
22. O'Donnell W.J. "Stress and Deflections on Built-in Beams", Journal of Engineering for Industry, Aug.1963
23. Premilhat A., Tordion G.V., Baronet C.N. "An Improved Determination of the Elastic Compliance of a Spur Gear Tooth Acted on by a Concentrated Load", ASME, Journal of Engineering for Industry, May 1974
24. Roark R.J. "Formulas for Stress and Strain", McGraw-Hill third edition, 1954, p.100
25. H. Schenk Jr., "Theories of Engineering Experimentation", Chapter 3, Second Edition, McGraw-Hill, 1968
26. Shigley J.E. "Mechanical Engineering Design", Second Edition 1972
27. Shotter B.A. "A New Approach to Gear Tooth Stresses", Journal of Engineering for Industry, Feb.1974
28. Timoshenko S.P., Goodier J.N. "Theory of Elasticity", 3rd Edition, McGraw-Hill, 1970

29. Weber C. "The Deformation of Loaded Gears and the Effect on their Load - Carrying Capacity", Sponsored Research (Germany), British Department of Scientific and Industrial Research, Report No.3, London, England, 1949
30. Wellauer E.J. and Seireg A. "Bending Strength of Gear Teeth by Cantilever Plate Theory", Transactions of ASME, Journal of Engineering for Industry, Vol.82, Series B, No.3, Aug.1960
31. Wilcox, L.E., Coleman, W. "Application of Finite Elements to the Analysis of Gear Tooth Stresses", Journal of Engineering for Industry, Nov.1973
32. Wilcox, L.E. "Finite Element Analysis Pinpoints Gear Tooth Stresses", Machine Design, Feb.1978, pp.88-92

#### B. Secondary Sources

33. Baud R.V., Hall E. "Stress Cycle in Gear Teeth", Mechanical Engineering, Vol.53, No.3, p.207 ff, cited in [12]
34. Baud R.V., Peterson R.E. "Load and Stress Cycles in Gear Teeth", Mechanical Engineering, Vol.51, No.9, pp.653 - 662 cited in [12],[22]
35. Black, P.H. "An Investigation of Relative Stresses in Solid Spur Gears by the Photoelastic Method", University of Illinois, Engineering Experimental Station Bulletin No.288, 1936 cited in [12]
36. Glaubitz H. "Root Strength of Straight Toothed Steel Spur Gears", Sponsored Research Report No.23, Department of Scientific and Industrial Research 1950 cited in [20]
37. Lewis W. "Investigation of the Strength of Gear Teeth", Proceedings Engineers Club (Philadelphia), Oct.1892 cited in [12],[26] etc.
38. Merrit W.E., "Gear Tooth Stresses and Rating Formula", Proceedings of Institution of Mechanical Engineers, Vol.166, 1952 cited in [31]
39. Timoshenko S., Baud R.V. "Strength of Gear Teeth", Mechanical Engineering, Vol.48, Nov.1926, p.1105 ff, cited in [12],[31]

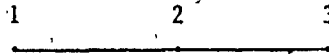
40. Ustinenko V.L. "Influence of Some Parameters on the Bending Stress in Spur Gear Teeth" (in Russian), Vestnik Mashinostroenja (Transactions for Mechanical Design), No.11, 1962, p.33 ff, cited in [5]
41. Walker H. (three articles, no title given)  
The Engineer, 1938, Oct.14, p.410, Fig.L  
The Engineer, 1938, Oct.21, p.435  
The Engineer, 1946, July 12, p.26, Fig.8  
cited in [29]

## — Appendix (1)

Work Equivalent Loads

When a distributed line load is replaced by a set of joint loads the work done must remain the same. Principles of virtual work are used.

The method was applied by P.C. Dimenhta [11], the fundamentals are described by R.H. Gallagher [16]. For simplicity consider a "single" degree of freedom. The edge of an element with a midside node is shown below:



Let  $\{P\}_{1 \times 1}$  and  $\{\delta\}_{1 \times 1}$  be the distributed loads and displacements.

The nodal forces and displacements are respectively:

$$\begin{Bmatrix} F_1 \\ F_2 \\ F_3 \end{Bmatrix}_{3 \times 1} \quad \begin{Bmatrix} \delta_1 \\ \delta_2 \\ \delta_3 \end{Bmatrix}_{3 \times 1}$$

The distributed displacements are tied to the nodal displacements by the relationship:

$$\{\delta\}_{1 \times 1} = [NA]_{1 \times 3} \{\delta_1\}_{3 \times 1} \quad (A.1)$$

where  $[NA] = [N_1 \ N_2 \ N_3]$  is the shape function.

As the assumed displacements are parabolic, and isoparametric formulation is used:

$$N_1 = \frac{1}{2} \xi (\xi - 1) \quad N_2 = (1 - \xi)^2 \quad N_3 = \frac{1}{2} \xi (1 + \xi) \quad (A.2)$$

where  $\xi$  is a "natural" coordinate which may take values of  $-1$  to  $1$ .

The relationship for virtual displacements:

$$-\{\Delta \delta\}_{1 \times 1} = [NA]_{1 \times 3} \{\Delta \delta_1\}_{3 \times 1} \quad (A.3)$$

The potential due to a virtual displacement with distributed loads:

$$\delta V = \int_s [\Delta \delta]_{1 \times 1} \{b\}_{1 \times 1} ds \quad (A.4)$$

The work done by the external nodal forces is the same as that by the distributed loads:

$$\begin{aligned} [\Delta \delta_1]_{1 \times 3}^T \{F_1\}_{3 \times 1} &= \int_s [NA]_{1 \times 3} [\Delta \delta_1]_{3 \times 1} \{p\}_{1 \times 1} ds \\ &= [\Delta \delta_1]_{1 \times 3}^T \int_s [NA]_{3 \times 1}^T \{p\}_{1 \times 1} ds \end{aligned}$$

therefore:

$$\{F_1\}_{3 \times 1} = \int_s [NA]^T_{3 \times 1} \{p\}_{1 \times 1} ds \quad (A.5)$$

The distributed load expressed by the load intensities at the nodes:

$$\{p\}_{1 \times 1} = \{N_1 p_1 + N_2 p_2 + N_3 p_3\}_{1 \times 1} = [p_1 \ p_2 \ p_3] \begin{Bmatrix} N_1 \\ N_2 \\ N_3 \end{Bmatrix} = [PA] \{NB\}$$

Hence:

$$\{F_1\}_{3 \times 1} = \int_s [NA]_{3 \times 1}^T [PA]_{1 \times 3} \{NB\}_{3 \times 1} ds \quad (A.6)$$

Expanding  $[NA]^T [PA] \{NB\}$

$$= \begin{Bmatrix} N_1 \\ N_2 \\ N_3 \end{Bmatrix}_{3 \times 1} [p_1 \ p_2 \ p_3]_{1 \times 3} \begin{Bmatrix} N_1 \\ N_2 \\ N_3 \end{Bmatrix}_{3 \times 1} = \begin{bmatrix} N_1 p_1 & N_1 p_2 & N_1 p_3 \\ N_2 p_1 & N_2 p_2 & N_2 p_3 \\ N_3 p_1 & N_3 p_2 & N_3 p_3 \end{bmatrix}_{3 \times 3} \begin{Bmatrix} N_1 \\ N_2 \\ N_3 \end{Bmatrix}_{3 \times 1}$$

$$= \begin{bmatrix} N_1^2 p_1 + N_1 N_2 p_2 + N_1 N_3 p_3 \\ N_1 N_2 p_1 + N_2^2 p_2 + N_2 N_3 p_3 \\ N_1 N_3 p_1 + N_2 N_3 p_2 + N_3^2 p_3 \end{bmatrix}_{3 \times 1}$$

This product may be rearranged:

$$= \begin{bmatrix} N_1^2 & N_1 N_2 & N_1 N_3 \\ N_1 N_2 & N_2^2 & N_2 N_3 \\ N_1 N_3 & N_2 N_3 & N_3^2 \end{bmatrix}_{3 \times 3} \begin{Bmatrix} p_1 \\ p_2 \\ p_3 \end{Bmatrix}_{3 \times 1} = [NC]_{3 \times 3} \{PB\}_{3 \times 1}$$

therefore:  $\{F\}_{3 \times 1} = \int_s [NC]_{3 \times 3} \{PB\}_{3 \times 1} ds$  (A.7)

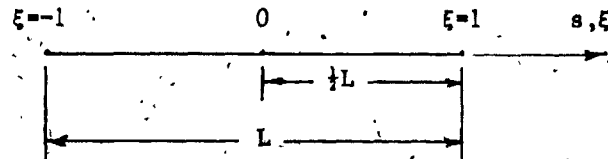


Fig. A-1

The isoparametric coordinate  $\xi$  takes values from -1 to 1.  
also for the given coordinate systems:

$$\xi = \frac{2s}{L} \quad \text{therefore:} \quad ds = \frac{L}{2} d\xi$$

After having integrated the entries in Eq. (A.7).

$$\int_s [NC] ds = \frac{1}{30} \begin{bmatrix} 4 & 2 & -1 \\ 2 & 16 & 2 \\ -1 & 2 & 4 \end{bmatrix} = [ND] \quad (A.8)$$

$$\{W\} = [ND] \{PB\} = \frac{1}{30} \begin{bmatrix} 4 & 2 & -1 \\ 2 & 16 & 2 \\ -1 & 2 & 4 \end{bmatrix} \begin{Bmatrix} p_1 \\ p_2 \\ p_3 \end{Bmatrix} \quad \text{hence} \quad (A.9)$$

$$W_1 = (4p_1 + 2p_2 - p_3) \frac{L}{30}$$

$$W_2 = (2p_1 + 16p_2 + 2p_3) \frac{L}{30}$$

$$W_3 = (-p_1 + 2p_2 - 4p_3) \frac{L}{30}$$

Eq's. (6.14)

